NASA TECHNICAL NOTE

NASA IN D-8192

STABILITY OF ELASTIC BENDING AND TORSION OF UNIFORM CANTILEVER ROTOR BLADES IN HOVER WITH VARIABLE STRUCTURAL COUPLING

Dewey H. Hodges and Robert A. Ormiston

Ames Research Center
and U.S. Army Air Mobility R&D Laboratory
Moffett Field, Calif. 94035

NATIONAL AERONAUTICS AND SPACE ADMINISTRATION • WASHINGTON, D. C. • APRIL 1976

1. Report No. NASA TN D-8192	2. Government Accession No.	3. Recipient's Catalog No.
4. Title and Subtitle STABILITY OF ELASTIC BENDING AND TORSION OF UNIFORM CANTILEVER ROTOR BLADES IN HOVER WITH VARIABLE STRUCTURAL COUPLING		5. Report Date April 1976 6. Performing Organization Code
7. Author(s) Dewey H. Hodges* and Robert A. Ormiston*		8. Performing Organization Report No. A-6375
9. Performing Organization Name and Address NASA Ames Research Center and Ames Directorate, U.S. Army Air Mobility R&D Laboratory Moffett Field, CA 94035		10. Work Unit No. 505-10-21-09 11. Contract or Grant No.
12. Sponsoring Agency Name and Address National Aeronautics and Space Administration, Wash., D.C. 20546 and U.S. Army Air Mobility R&D Laboratory, Moffett Field, CA 94035		13. Type of Report and Period Covered Technical Note 14. Sponsoring Agency Code

15. Supplementary Notes

*Ames Directorate, U.S. Army Air Mobility R&D Laboratory

16. Abstract The stability of elastic flap bending, lead-lag bending, and torsion of uniform, untwisted, cantilever rotor blades without chordwise offsets between the elastic, mass, tension, and aerodynamic center axes is investigated for the hovering flight condition. The equations of motion are obtained by simplifying the general, nonlinear, partial differential equations of motion of an elastic rotating cantilever blade. The equations are adapted for a linearized stability analysis in the hovering flight condition by prescribing aerodynamic forces, applying Galerkin's method, and linearizing the resulting ordinary differential equations about the equilibrium operating condition. The aerodynamic forces are obtained from strip theory based on a quasi-steady approximation of two-dimensional unsteady airfoil theory. Six coupled mode shapes, calculated from free vibration about the equilibrium operating condition, are used in the linearized stability analysis. The study emphasizes the effects of two types of structural coupling that strongly influence the stability of hingeless rotor blades. The first structural coupling is the linear coupling between flap and lead-lag bending of the rotor blade. A structural coupling parameter $\mathfrak{K}$ is introduced to simulate variations in flap-lag structural coupling that arise for blades having nonuniform stiffness distributions. The second structural coupling is a nonlinear coupling between flap bending, lead-lag bending, and torsion deflections. Results are obtained for a wide variety of hingeless rotor configurations and operating conditions in order to provide a reasonably complete picture of hingeless rotor blade stability characteristics. The stability of torsionally flexible blades is strongly influenced by the effects of the bending-torsion sturctural coupling. Without precone, typical configurations are usually stable except for low values of $\mathfrak{K}$ or low torsion frequencies. Addition of precone is strongly destabilizing for a wide range of configurations. Except for very low torsion frequencies, the results also indicate that the structural terms in the torsion equation dominate the torsion inertia and damping terms which permits the use of an approximate, but simplified, system of equations with fewer degrees of freedom. Finally, the accuracy of the results is sensitive to the number and type of mode shapes used in the analysis.

17. Key Words (Suggested by Author(s)) Hingeless rotor, Rotating beam, Structural dynamics, Beam (nonlinear bending-torsion), Flap-lag-torsion stability, Structural coupling, Aeroelasticity, Helicopter rotor	18. Distribution Statement Unlimited STAR Category - 02

19. Security Classif. (of this report) Unclassified	20. Security Classif. (of this page) Unclassified	21. No. of Pages 78	22. Price* $4.75

CONTENTS

SYMBOLS

A	blade structure cross-section area, equations (6), m^2
$A_i - O_{ij}$	modal integrals, equations (B4)
a	airfoil lift curve slope, 2π per radian
b	number of blades
$[C]$	modal damping matrix, equation (28)
$C(k)$	Theodorsen's function
C_T	rotor thrust coefficient, thrust/$\rho_\infty \pi \Omega^2 R^4$
c	blade chord, m
c_{d_0}	airfoil profile drag coefficient
D	airfoil profile drag per unit length, equation (15), N/m
E	Young's modulus, N/m^2
G	shear modulus, N/m^2
$[G]$	modal gyroscopic matrix, equation (31)
h	vertical displacement of two-dimensional airfoil section normal to free-stream velocity component V, figure 5, m
$[I]$	identity matrix
$I_{y'}$, $I_{z'}$	cross-section area moments of intertia about the y' and z' axes, respectively, equations (6), m^4
J	torsional stiffness constant, equations (6), m^4
K	dimensionless parameter, equations (B2)
$[K]$	modal stiffness matrix, equation (28)
k	reduced frequency, $\omega c/2V$
k_A	blade cross-section polar radius of gyration, equations (6), m
k_m	blade cross-section mass radius of gyration, equations (6), m
k_{m_1}, k_{m_2}	principal mass radii of gyration, equations (6), m
L	aerodynamic lift per unit length, equations (11), N/m

L_u, L_v, L_w	generalized aerodynamic forces per unit length, equations (2) and (23), N/m
M	number of rotating coupled modes; also, aerodynamic pitching moment per unit length, equations (11), N-m/m
[M]	modal mass matrix, equation (28)
M_ϕ	generalized aerodynamic moment per unit length, equations (2) and (23), N-m/m
m	mass per unit length, equations (6), kg/m
N	number of nonrotating modes for each of the flap bending, lead-lag bending, and torsion deflections
[P], [P*]	matrices whose eigenvalues determine stability, equations (30) and (35)
$\mathcal{R}$	flap-lag structural coupling parameter
R	blade length, m
S	aerodynamic force per unit length tangent to blade airfoil chordline, figure 6, N/m
T	blade tension, N; also, aerodynamic force per unit length normal to blade airfoil chordline, figure 6, N/m
t	time, sec
T	kinetic energy, equation (2), kg-m^2/sec^2
[T]	transformation matrix relating deformed and undeformed blade coordinate systems, equation (A2)
U	blade airfoil velocity with respect to the fluid, component normal to spanwise x' axis, equations (13), figure 5, m/sec
[U]	matrix of eigenvectors for free vibration of blade about its equilibrium position, equation (33)
U_P, U_T	velocity components of blade airfoil section with respect to the fluid, parallel to the y' and z' axes, respectively, figure 5, m/sec
u, v, w	displacements of the elastic axis in x, y, z directions, figure 3, m
U	strain energy, equation (2), N-m

V	free-stream velocity component of two-dimensional airfoil, figure 5, m/sec
$\vec{V}$	velocity of a point in the blade, equations (2), m/sec
V_j, W_j	lead-lag bending and flap bending generalized coordinates, equations (25)
v_i	induced downwash velocity, equation (24), m/sec
$\{X\}$	column vector of perturbation modal generalized coordinates, equation (29)
x, y, z	undeformed coordinate system, figure 3, m
x', y', z'	deformed coordinate system fixed to blade, figure 3, m
α	airfoil section angle of attack, figure 5, rad
$[\alpha]$	rotation matrix for angular velocity components, equation (A4)
α_i, α_j, α_k	components of angular velocity for blade airfoil section, equation (A4)
α_j, β_j, γ_j	constants for assumed mode shapes, equations (26)
β_{pc}	precone angle, figure 3, rad
γ	Lock number, $3 \rho_\infty acR/m$ for blade with uniform mass distribution
δ_{ij}	Kronecker delta
δW	virtual work of nonconservative forces, equations (2), N-m
ε	small parameter of the order of bending slopes; also airfoil section pitch angle with respect to free-stream velocity, figure 5, rad
ε_{xx}, $\varepsilon_{x\eta}$, $\varepsilon_{x\zeta}$	strain components, equations (3)
η, ζ	blade cross section principal axes coordinates, figure 4, m
$\theta_j(\bar{x})$	nonrotating torsional mode shape, equation (26)
θ	blade pitch angle, rad
θ_{cr}	blade pitch angle where motion is neutrally stable, rad
θ_β, θ_ζ	equivalent kinematic pitch-flap and pitch-lag coupling parameters defined by bending torsion structural coupling, equations (40)

κ	dimensionless torsional rigidity, equations (B2)
$\lambda\ (\eta, \zeta)$	warp function, equation (3)
Λ_1, Λ_2	dimensionless bending stiffnesses, equations (B2)
μ, μ_1, μ_2	dimensionless mass radii of gyration, equations (B2)
ρ	structural density, kg/m^3
ρ_∞	air density, kg/m^3
σ	solidity $bc/\pi R$; also, real part of eigenvalues, made dimensionless by Ω
$\sigma_{xx}, \sigma_{x\eta}, \sigma_{x\zeta}$	engineering stress components, N/m
Φ_j	torsion generalized coordinates, equations (25)
ϕ	elastic torsion deflection about x' axis, figures 3 and 4, rad
$\Psi_j(\bar{x})$	nonrotating flap and lead-lag bending mode shapes, equations (26)
ψ	dimensionless time, Ωt
$\omega_v, \omega_w, \omega_\phi$	fundamental lead-lag, flap, and torsion natural frequencies, made dimensionless by Ω
ω	imaginary part of eigenvalue, made dimensionless by Ω
Ω	rotor blade angular velocity, sec^{-1}
$(\ )'$	$\partial/\partial x$ ($\partial/\partial \bar{x}$ in appendix B)
$(\dot{\ })$	$\partial/\partial t$ ($\partial/\partial \psi$ in appendix B)
$(\ )_0, \Delta(\ )$	equilibrium and perturbation components of generalized coordinates
$(\ )_C$	circulatory aerodynamic term
$(\ )_{NC}$	noncirculatory aerodynamic term
$(\ )_{NR}$	frequency of a nonrotating beam, made dimensionless by Ω
$(\bar{\ })$	length quantity made dimensionless by R, or velocity made dimensionless by ΩR
$[\ ]^T$	transpose of a square matrix

STABILITY OF ELASTIC BENDING AND TORSION OF UNIFORM CANTILEVER ROTOR BLADES IN HOVER WITH VARIABLE STRUCTURAL COUPLING

Dewey H. Hodges* and Robert A. Ormiston*

Ames Research Center
and
Ames Directorate
U.S. Army Air Mobility R&D Laboratory

SUMMARY

The stability of elastic flap bending, lead-lag bending, and torsion of uniform, untwisted, cantilever rotor blades without chordwise offsets between the elastic, mass, tension, and aerodynamic center axes is investigated for the hovering flight condition. The equations of motion are obtained by simplifying the general, nonlinear, partial differential equations of motion of an elastic rotating cantilever blade. The equations are adapted for a linearized stability analysis in the hovering flight condition by prescribing aerodynamic forces, applying Galerkin's method, and linearizing the resulting ordinary differential equations about the equilibrium operating condition. The aerodynamic forces are obtained from strip theory based on a quasi-steady approximation of two-dimensional unsteady airfoil theory. Six coupled mode shapes, calculated from free vibration about the equilibrium operating condition, are used in the linearized stability analysis. The study emphasizes the effects of two types of structural coupling that strongly influence the stability of hingeless rotor blades. The first structural coupling is the linear coupling between flap and lead-lag bending of the rotor blade. A structural coupling parameter κ is introduced to simulate variations in flap-lag structural coupling that arise for blades having nonuniform stiffness distributions. The second structural coupling is a nonlinear coupling between flap bending, lead-lag bending, and torsion deflections. Results are obtained for a wide variety of hingeless rotor configurations and operating conditions in order to provide a reasonably complete picture of hingeless rotor blade stability characteristics. The stability of torsionally flexible blades is strongly influenced by the effects of the bending-torsion structural coupling. Without precone, typical configurations are usually stable except for low values of κ or low torsion frequencies. Addition of precone is strongly destabilizing for a wide range of configurations. Except for very low torsion frequencies, the results also indicate that the structural terms in the torsion equation dominate the torsion inertia and damping terms which permits the use of an approximate, but simplified, system of equations with fewer degrees of freedom. Finally, the accuracy of the results is sensitive to the number and type of mode shapes used in the analysis.

---

*Ames Directorate, U.S. Army Air Mobility R&D Laboratory

INTRODUCTION

The general problem of helicopter aeroelastic stability involves coupling between the motion of the individual blades and coupling between the rotor and the body of the helicopter; control system dynamics may also be involved. The complexity of the general problem poses a considerable challenge to the analyst, both in developing an analytical model of the system and in understanding its physical behavior. An important part of the general rotor-body dynamic system is the single blade rotating about an axis fixed in space. For many problems of practical interest, blade-to-blade and rotor-body couplings are not significant and the analysis of a single rotor blade constitutes an important problem by itself. Even when coupling with other blades and the body is significant, the single blade behavior usually remains recognizable and can be helpful in understanding the behavior of the more complete system. For this reason, the dynamics of a single blade forms an important fundamental building block in the study of helicopter dynamics.

Helicopter rotors with cantilever blades are commonly termed hingeless rotors. In contrast with the more conventional articulated rotor, the cantilever blades of the hingeless rotor are attached directly to the hub without flap or lead-lag hinges. This configuration reduces mechanical complexity and improves helicopter flying qualities by increasing rotor control power and angular rate damping. The lack of hinge articulation also alters the structural characteristics of the rotor blade and can significantly influence aeroelastic stability.

Aeroelastic stability of the articulated rotor blade is primarily determined by the relative chordwise position of the aerodynamic center, center of mass, and elastic axes. When these are unfavorable, an instability may occur that is usually characterized by coupled flap bending and torsion deflections with a frequency near the torsion natural frequency.

In the case of the hingeless rotor blade, another type of instability is possible because of the structural coupling between bending and torsion deflections of cantilever blades. This type of instability is usually characterized by coupled flap bending, lead-lag bending, and torsion deflections of the blade with a frequency near the lead-lag bending natural frequency. The structural coupling of cantilever blades is significantly dependent on the specific configuration parameters of the rotor blade. The magnitude and variability of this coupling make the analysis of cantilever rotor blades a complex and important subject. Moreover, the stability characteristics of hingeless rotor blades are still not well understood, even though considerable work has been devoted to this problem recently. The present investigation is intended to provide an improved understanding of the basic structural aspects of these problems; therefore, the effects of chordwise offsets between the elastic, mass, tension, and aerodynamic center axes are not included in this report.

The general equations of motion for a torsionally flexible cantilever rotor blade contain important nonlinear inertial and structural terms. These nonlinearities may be expected to cause nonlinear blade motion behavior, such

as limit cycles or nonlinear instabilities. For the present report, this type of behavior is not considered, and only the linear stability characteristics are treated. This does not mean, however, that nonlinear terms in the equations are ignored. In the present analysis, perturbation equations are obtained by linearizing the nonlinear equations about a suitable equilibrium condition. The influence of the nonlinear terms is then manifest in the coefficients of the linear perturbation equations.

If it is necessary to treat the complete nonlinear equations, more elaborate analyses must be used such as numerical integration of the equations or asymptotic expansion techniques. However, these methods are more difficult to apply than the standard eigenvalue methods used for linear equations and they are not as well suited to investigations where extensive numerical results are desired for a broad range of system parameters. Furthermore, an analysis of the nonlinearities cannot be justified logically until the linear behavior of the system is sufficiently well understood. For these reasons the scope of the present report is restricted to a linear stability analysis based on linearization of the general nonlinear equations of motion found in reference 1. Before briefly describing the procedure used in this report, it will be useful to review previous related research.

Discussion of Previous Research

Recent investigations of flap-lag-torsion stability of elastic cantilever rotor blades were preceded by simpler analyses of flap-lag stability of torsionally rigid blades. These flap-lag investigations revealed some of the complexities of nonlinear aerodynamic and inertial flap-lag coupling terms of cantilever rotor blades. The early flap-lag analyses usually relied on an approximate representation consisting of a rigid blade with spring restrained hinges at the hub to simulate bending flexibility. At that time, the most comprehensive equations applicable to rotating elastic beams were the linear equations developed by Houbolt and Brooks in reference 2.

In the early flap-lag analysis of reference 3, Young investigated the possibility that nonlinear aerodynamic and inertial coupling terms could be destabilizing for hingeless rotors. Subsequently, Hohenemser and Heaton (ref. 4) showed that linearized equations of motion for the spring restrained, hinged, rigid blade approximation could be used to investigate flap-lag instability in hover and forward flight. Further investigations in hover by Ormiston and Hodges (ref. 5), again using the rigid blade approximation, showed that the distribution of flexibility inboard and outboard of the pitch bearing (the degree of flap-lag structural, or elastic, coupling) was an important factor influencing stability. Flap-lag stability of elastic cantilever blades with uniform properties was studied by Hodges and Ormiston (refs. 5 and 6), based on a derivation of nonlinear partial differential equations suitable for elastic hingeless rotor blades. The results confirmed that the approximate rigid blade model could accurately predict lead-lag damping provided that the flap-lag structural coupling was properly represented. Similar equations were studied by Friedmann and Tong (refs. 7 and 8), except that flap-lag structural coupling was not included. The stability

characteristics were determined by using an asymptotic expansion procedure with multiple time scales. The results indicated that certain configurations shown to be unstable from a simple linearized stability analysis would exhibit large amplitude limit-cycle behavior with the more elaborate analysis.

Concurrently with the restricted flap-lag stability analyses, efforts were also made to investigate the complete problem including torsional blade deflections. Torsion deflections of hingeless rotor blades are strongly influenced by nonlinear structural moments caused by flap and lead-lag bending. This bending-torsion structural coupling, discussed by Mil' *et al.* (ref. 9) is proportional to the product of the flap and lead-lag bending curvatures and the difference between the two bending flexibilities. Other investigators have also noted the importance of bending-torsion structural coupling (refs. 10-13) and it has been approximated in some stability analyses using the rigid, hinged blade approximation (refs. 14-16). The latter analyses also include fuselage degrees of freedom as well as rotor blade deflections.

One of the first efforts toward the nonlinear flap-lag-torsion problem for a fully elastic blade was a derivation of nonlinear equations of motion for elastic flap bending, lead-lag bending, and torsion of rotating beams by Arcidiacono (ref. 17). The equations were derived in a reasonably detailed and complete manner; however, some small nonlinear inertial terms were not included.

Friedmann and Tong (ref. 7) and Friedmann (ref. 18) also developed flap-lag-torsion equations. Elastic flap and lead-lag bending of a uniform blade were considered, but the torsional deflections were approximated by rigid body pitching motion (root torsion). The results of reference 7 indicated that torsion motion was important and that the stability characteristics were sensitive to the number and type of assumed bending mode shapes used. Flap-lag structural coupling was not included in these reports, however, and only a few numerical results were presented.

Hodges (ref. 19) developed a system of nonlinear flap-lag-torsion equations for an elastic torsionally flexible cantilever blade and applied them to a cantilever blade stability analysis. The equations contained some small erroneous structural terms later shown to be due to incorrect shear strain-displacement relations. Numerical results illustrated the importance of elastic torsional flexibility and the possibility of omitting, for some configurations, torsional dynamics from the equations of motion and retaining only the structural (kinematic) effects of torsion.

Hodges and Dowell (ref. 1) corrected and extended Hodges' derivation of the nonlinear flap-lag-torsion equations using both Hamilton's principle and the Newtonian method. Prior to formal publication of reference 1, Hodges and Ormiston (ref. 20) applied these equations to a uniform rotor blade of solid cross section. Without blade precone, most hingeless rotor configurations with uniform blade properties and typical bending and torsion frequencies were found to be stable. Positive precone was found to be destabilizing in the range of typical lead-lag and torsion frequencies. The main destabilizing factors were shown to be the bending-torsion structural coupling and, for configurations of low torsional stiffness, torsional dynamics.

Additional numerical results were presented by Friedmann in references 21-23. In references 21 and 22, flap-lag structural coupling was omitted and an error in the equations led to incorrect conclusions regarding the importance of blade droop (as mentioned in the discussion of ref. 22). In reference 23, flap-lag structural coupling was included and thus the problem treated was similar to that of reference 20, except for the representation of torsion motion.

With the possible exception of reference 20, the work cited above does not furnish extensive numerical results for the stability characteristics of elastic cantilever rotor blades. This report is intended to provide results for a broad range of system parameters and to illustrate the general stability characteristics of hingeless rotors. It is an extension of reference 20 and incorporates the following changes: (1) the assumption of a blade model with a solid cross section is discarded, thereby permitting the stiffness and inertial parameters of the blade to be specified independently; (2) a sufficiently large number of assumed mode shapes is used to ensure convergence; (3) along with some notational changes, the blade configurations are defined in terms of rotating natural frequencies rather than nonrotating frequencies; and (4) blade configurations with various degrees of flap-lag structural coupling are represented by introducing a structural coupling parameter $\mathcal{R}$.

Procedure

The derivation of the general nonlinear equations of motion for an elastic rotating cantilever beam (ref. 1) is summarized in this report and specialized to a basic cantilever blade configuration without twist, nonuniformities in mass and stiffness, or chordwise offsets. A detailed derivation of the aerodynamic forces is given based on strip theory and on a quasi-steady approximation of unsteady aerodynamic theory for a two-dimensional airfoil. The nonlinear partial differential equations are transformed into a system of ordinary differential equations by Galerkin's method. These nonlinear equations of the generalized coordinates are linearized for small perturbation motions about the equilibrium operating condition. An iterative solution of the nonlinear algebraic equilibrium equations enables the coefficients of the perturbation differential equations to be determined. Finally, the eigenvalues of the perturbation equations that determine the dynamic stability of blade motions about the equilibrium are obtained. Coupled mode shapes, determined from free vibrations (*in vacuo*) of the blade about the equilibrium operating condition, are used.

The equations are solved for a variety of practical hingeless rotor configurations with emphasis on the variation of torsion frequency, lead-lag frequency, precone, the structural coupling parameter, and the collective pitch. Results are presented in the form of plots of equilibrium tip deflection, locus of roots, lead-lag damping, and stability boundaries.

GENERAL HINGELESS ROTOR CONFIGURATION PARAMETERS

A comprehensive study of hingeless rotor stability is a formidable task because there is a large number of important configuration parameters. The purpose of the present report is to investigate the primary parameters of a somewhat simplified configuration in a systematic manner; the remaining parameters are not considered. In order to place the present simplified configuration in proper perspective it is appropriate to describe the physical characteristics and define the parameters of a typical hingeless rotor blade.

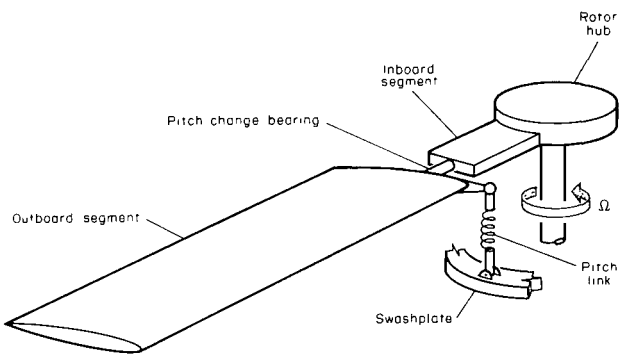

Figure 1.- Primary elements of a typical hingeless rotor blade (not all these elements are considered in the present analysis).

The general cantilever blade structure, shown in figure 1, is composed of two flexible beam segments joined by the pitch change bearing. The inboard hub segment is fixed to the hub at the root end of the blade, while the outboard segment can be rotated about the pitch change bearing by vertical movement of the pitch link from the swashplate controls. Pitch link flexibility, represented by a spring element, will permit rigid body pitching motion of the outboard blade segment (i.e., root torsion). In general, both the inboard and outboard segments of the rotor blade will have large nonuniformities of mass, bending stiffness, and torsional rigidity, and both segments will bend and twist. These nonuniformities contribute to the important and complex structural coupling between the flap bending, lead-lag bending, and torsion of hingeless rotor blades. Some additional configuration parameters of importance are precone, droop, torque offset, and sweep, all of which are illustrated in figure 2. These geometric parameters are usually tailored to minimize the steady state rotor blade stresses or to improve rotorcraft flying qualities, but they can also have an important influence on rotor blade stability.

The above features may differ for certain special hingeless rotor configurations. For example, it is not uncommon for the inboard beam segment to be eliminated entirely by placing the pitch change bearing in the hub itself, thus leaving only a single outboard blade segment. Or the pitch bearing may be eliminated by making the inboard segment very flexible in torsion so that pitch change of the outboard segment is accommodated by twisting the inboard segment.

The blade structure itself may also influence the stability characteristics. A rotor blade may consist of several spar, skin, stiffener, and balance weight components, or it may be molded from many layers of composite materials bonded together. These materials must all be tailored to provide acceptable aerodynamic, strength, and stiffness properties. Additional parameters

influenced by these construction details are the positions of the mass center, tension center, elastic axis (shear center), and the aerodynamic center. If these are not coincident, additional structural, inertial, and aerodynamic coupling between bending and torsion deflections will be introduced and may strongly influence rotor blade stability, as in the case of an articulated blade. The rotor blade may also be specially designed to produce desirable structural coupling effects; these effects may include equivalent pitch-flap and pitch-lag coupling, both of which can improve both rotor blade stability and rotorcraft flying qualities. Similar coupling effects may result from the kinematics of the pitch-link connection between the outboard blade segment and the swashplate control system. If the inboard blade segment is especially long or flexible, this kinematic coupling may be particularly significant because the motion of the pitch bearing due to blade bending is increased.

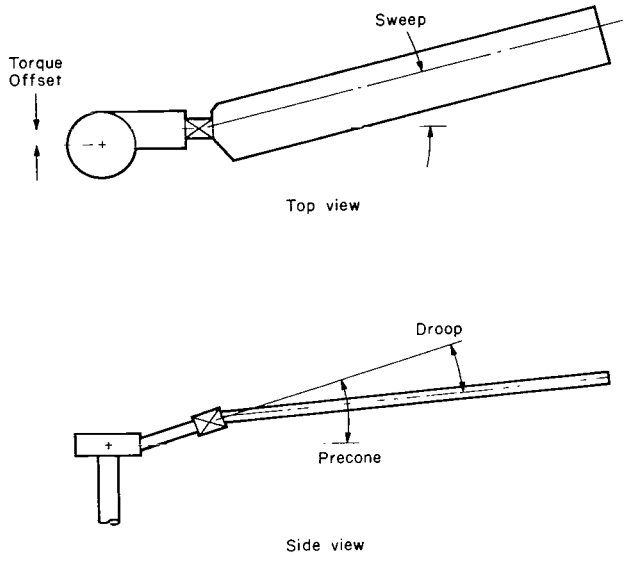

Figure 2.- Configuration parameters of a hingeless rotor blade (of these parameters only precone is considered in the present analysis).

As noted above, not all the rotor blade details described here are considered in this report. The present analysis treats the elastic flap, lead-lag, and torsion deflections of a simple untwisted uniform blade with precone, but excludes pitch link flexibility, droop, sweep, or torque offset. Furthermore, mass, tension axis, and aerodynamic center offsets from the elastic axis are all zero. The equations of motion are written for a single outboard blade segment without a flexible hub segment inboard of the pitch bearing. However, the effects of variable structural coupling due to the inboard and outboard segments are simulated by introducing the structural coupling parameter $\mathfrak{K}$ to arbitrarily vary the structural coupling in the uniform blade equations.

EQUATIONS OF MOTION

The equations of motion are taken from reference 1 and specialized for the present simplified blade configuration having uniform mass and stiffness, no twist, and no chordwise offsets of the elastic axis, tension axis, or center of mass. A brief outline of the derivation is given for completeness, and one modification to the equations is made to accommodate an approximate structural coupling parameter for expanding the scope of the numerical results. The expressions for aerodynamic forces are not included in reference 1; they

are derived in detail below on the basis of two-dimensional unsteady aerodynamic theory.

Coordinate Systems

Consider the undeformed beam in figure 3 with its elastic axis coincident with the x axis of the x, y, z coordinate system rotating with a constant angular velocity about a fixed point at the origin. The y axis lies in the plane of rotation and the x axis is rotated through a small angle β_{pc} from the plane of rotation. Bending deflections of the beam are defined by the displacements u, v, and w of the elastic axis parallel to the x, y, z coordinates, respectively. A second coordinate system, x', y', and z', fixed to the blade with y', z' axes parallel to the beam cross section principal axes, moves with the blade as it undergoes bending displacements, torsional displacements, and pitch angle rotation, θ. The projection of the beam cross section in the y, z plane is shown before and after deformation in figure 4. Before deformation, the blade principal axes are rotated with respect to the undeformed coordinates by the pitch angle. After deformation, the elastic axis is displaced by u, v, w and the blade twisted through the angle ϕ. Although the deformed y', z' axes do not lie exactly in the y, z plane, their projection in that plane is shown in figure 4. A small apparent twist, discussed in reference 24, is neglected by ignoring the difference between the actual and the projected twist angle ϕ, but this must be accounted for in deriving the blade aerodynamic forces.

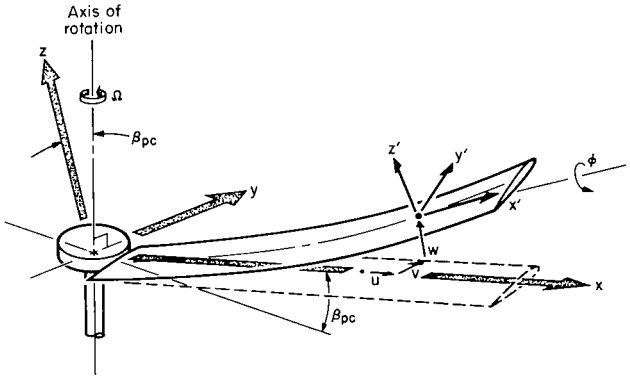

Figure 3.- Rotor blade coordinate systems and deflections.

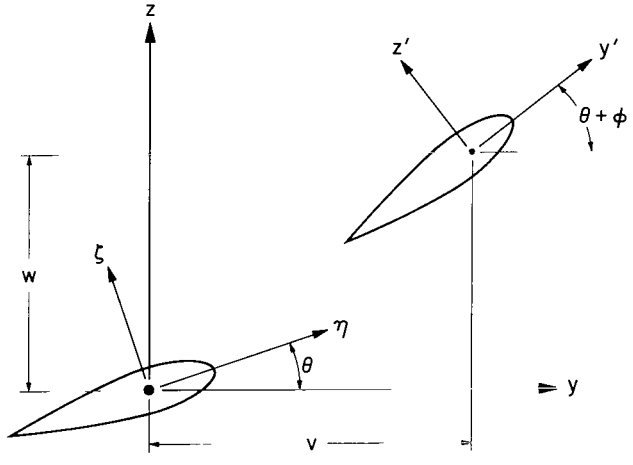

Figure 4.- Rotor blade cross section before and after deflections; note that y' and z' are projections on the y, z plane.

Structural and Inertial Terms

The equations of motion are derived using Hamilton's principle

$$\int_{t_1}^{t_2} (\delta U - \delta T - \delta W)dt = 0 \tag{1}$$

where the strain energy U, the kinetic energy T, and the virtual work of external forces δW are given by

$$\left.\begin{aligned} U &= \frac{1}{2}\int_0^R \iint_A (\sigma_{xx}\varepsilon_{xx} + \sigma_{x\eta}\varepsilon_{x\eta} + \sigma_{x\zeta}\varepsilon_{x\zeta})d\eta\, d\zeta\, dx \\ T &= \frac{1}{2}\int_0^R \iint_A \rho\vec{V}\cdot\vec{V}\, d\eta\, d\zeta\, dx \\ \delta W &= \int_0^R (L_u\delta u + L_v\delta v + L_w\delta w + M_\phi\delta\phi)dx \end{aligned}\right\} \tag{2}$$

For the strain energy, the stresses are proportional to the strains: $\sigma_{xx} = E\varepsilon_{xx}$, $\sigma_{x\eta} = G\varepsilon_{x\eta}$, and $\sigma_{x\zeta} = G\varepsilon_{x\zeta}$. In the kinetic energy, $\vec{V}$ is the velocity vector of an arbitrary point in the blade. The loads L_u, L_v, L_w, and M_ϕ are of aerodynamic origin and are treated below. The strain displacement relations as derived in reference 1 are:

$$\left.\begin{aligned} \varepsilon_{xx} &= u' + \frac{v'^2}{2} + \frac{w'^2}{2} + \left(\theta'\phi' + \frac{\phi'^2}{2}\right)(\eta^2 + \zeta^2) - \lambda\phi'' \\ &\quad - v''[\eta\cos(\theta + \phi) - \zeta\sin(\theta + \phi)] \\ &\quad - w''[\eta\sin(\theta + \phi) + \zeta\cos(\theta + \phi)] \\ \varepsilon_{x\eta} &= -\left(\zeta + \frac{\partial\lambda}{\partial\eta}\right)\phi' \\ \varepsilon_{x\zeta} &= \left(\eta - \frac{\partial\lambda}{\partial\zeta}\right)\phi' \end{aligned}\right\} \tag{3}$$

where λ is the warp function for the cross section. The function $\lambda(\eta, \zeta)$ may be determined by solving Laplace's equation for the specific cross section.

The remaining details of the derivation of the equations of motion are given in reference 1. An essential feature of the derivation is the introduction of an ordering scheme in which ε, a small parameter of the order of magnitude of the bending slopes, is introduced. The assumed order of magnitude of all quantities used in the equations appears in table 1. Within any equation, terms of $O(\varepsilon^3)$ are ordinarily dropped unless, for example, they

contribute to damping. The resulting dimensional equations are as follows, where the radial aerodynamic force component L_u is neglected as a higher order term.

δu equation:

$$-T' - m\Omega^2 x - \underline{2m\Omega\dot{v}} = 0 \tag{4a}$$

δv equation:

$$-(Tv')' + [EI_{z'} - (EI_{z'} - EI_{y'})\sin^2\theta]v'''' + (EI_{z'} - EI_{y'})\left[\frac{\sin 2\theta}{2} w'''' - \underline{\sin 2\theta(\phi v'')''} + \underline{\cos 2\theta(\phi w'')''}\right] + \underline{2m\Omega(\dot{u} - \beta_{pc}\dot{w})} + m(\ddot{v} - \Omega^2 v) = L_v \tag{4b}$$

δw equation:

$$-(Tw')' + [EI_{y'} + (EI_{z'} - EI_{y'})\sin^2\theta]w'''' + (EI_{z'} - EI_{y'})\left[\frac{\sin 2\theta}{2} v'''' + \underline{\cos 2\theta(\phi v'')''} + \underline{\sin 2\theta(\phi w'')''}\right] + \underline{2m\Omega\beta_{pc}\dot{v}} + m\ddot{w} = L_w - \underline{m\beta_{pc}\Omega^2 x} \tag{4c}$$

$\delta\phi$ equation:

$$\underline{(EI_{z'} - EI_{y'})\left[(w''^2 - v''^2)\frac{\sin 2\theta}{2} + v''w'' \cos 2\theta\right]} - GJ\phi'' - k_A^2(T\phi')' + mk_m^2\ddot{\phi} + m\Omega^2(k_{m_2}^2 - k_{m_1}^2)\phi \cos 2\theta = M_\phi - m\Omega^2(k_{m_2}^2 - k_{m_1}^2)\frac{\sin 2\theta}{2} \tag{4d}$$

TABLE 1.- ASSUMED ORDERS OF MAGNITUDE FOR PHYSICAL QUANTITIES

$\frac{c}{R} =$	$O(\varepsilon)$	$\frac{v}{R}, \frac{w}{R} =$	$O(\varepsilon)$
$\frac{c_{d_0}}{a} =$	$O(\varepsilon^2)$	$\frac{v_i}{\Omega R} =$	$O(\varepsilon)$
$\frac{d}{\Omega dt}, R\frac{d}{dx} =$	$O(1)$	$\beta_{pc} =$	$O(\varepsilon)$
$\frac{EA}{m\Omega^2R^2} =$	$O(\varepsilon^{-2})$	$\phi =$	$O(\varepsilon)$
$\frac{EI_{y'}}{m\Omega^2R^4}, \frac{EI_{z'}}{m\Omega^2R^4}, \frac{GJ}{m\Omega^2R^4} =$	$O(1)$	$\theta =$	$O(1)$
$\frac{k_A}{R}, \frac{k_{m_1}}{R}, \frac{k_{m_2}}{R}, \frac{k_m}{R} =$	$O(\varepsilon)$	θ (aerodynamic forces only) $=$	$O(\varepsilon)$

where the tension is given by

$$T = EA\left(u' + \frac{v'^2}{2} + \frac{w'^2}{2}\right) \tag{5}$$

and

$$\left.\begin{aligned}
A &\equiv \iint_s d\eta\, d\zeta \\
I_{y'} &\equiv \iint_s \zeta^2\, d\eta\, d\zeta \\
I_{z'} &\equiv \iint_s \eta^2\, d\eta\, d\zeta \\
k_A^2 &\equiv \frac{I_{y'} + I_{z'}}{A} \\
J &\equiv \iint_s \left[\left(\eta - \frac{\partial\lambda}{\partial\zeta}\right)^2 + \left(\zeta + \frac{\partial\lambda}{\partial\eta}\right)^2\right] d\eta\, d\zeta \\
m &\equiv \iint_m \rho\, d\eta\, d\zeta \\
k_{m_1}^2 &\equiv \frac{1}{m} \iint_m \rho\zeta^2\, d\eta\, d\zeta \\
k_{m_2}^2 &\equiv \frac{1}{m} \iint_m \rho\eta^2\, d\eta\, d\zeta \\
k_m^2 &\equiv k_{m_1}^2 + k_{m_2}^2
\end{aligned}\right\} \tag{6}$$

These cross-sectional integrals in equation (6) define the structural and mass properties of the rotor blade cross section. The subscripts s or m refer to integration over the portion of the cross section which contributes structural or mass characteristics, respectively. These properties are the radial stiffness EA, the flapwise and chordwise bending stiffness $EI_{y'}$ and $EI_{z'}$, the polar radius of gyration k_A, the torsional rigidity GJ, the mass per unit length m, the flapwise and chordwise principal mass moments of inertia $mk_{m_1}^2$ and $mk_{m_2}^2$, and the torsional mass moment of inertia mk_m^2.

The present nonlinear equations may be compared directly with the well-known linear equations of Houbolt and Brooks (ref. 2). When specialized to untwisted beams with uniform mass and stiffness and with no chordwise offsets, the equations of Houbolt and Brooks are identical to the present equations with the exception that the underlined terms in equations (4) are not present.

The underlined nonlinear terms arise from both inertial and structural effects and they are important for dynamic analyses of cantilever rotor blades. (The underlined terms due to precone β_{pc} are linear, but precone was not considered by Houbolt and Brooks.)

The various terms in the present equations will now be briefly described. We first discuss the inertial terms, and in particular the nonlinear flap-lag inertial coupling terms. In the δu equation, the term $-2m\Omega\dot{v}$ represents the centrifugal force of lead-lag deflection velocity. This dependence of tension on lead-lag deflection produces nonlinear products when T is substituted into the $(Tv')'$ and $(Tw')'$ terms in the lead-lag and flap bending equations. A similar nonlinear expression for the $2m\Omega\dot{u}$ Coriolis term in the lead-lag equation may be obtained by solving for u in terms of v, w, and T in the nonlinear strain relation, equation (5). As discussed in reference 6, these terms must be included to properly represent the Coriolis and centrifugal coupling between the flap and lead-lag equations. In the torsion equation, the tension-torsion coupling term $-k_A^2(T\phi')'$, has a small coefficient and only the linear contribution $-k_A^2(m\Omega^2/2)[(R^2 - x^2)\phi']'$ is retained. Inertia terms in the torsion equation include the torsional inertia $mk_m^2\ddot{\phi}$ and the tennis racket effect; the tennis racket effect is proportional to the difference between the principal mass moments of inertia. We next discuss the structural terms.

In addition to the familiar torsional rigidity term $-GJ\phi''$, there are the nonlinear bending-torsion structural coupling terms underlined in the torsion equation, (eq. (4d)). These terms are probably the most important ones for hingeless rotor stability because they are large and sensitive to many configuration parameters. They are actually moments proportional to the difference between lead-lag and flap bending stiffness $EI_{z'} - EI_{y'}$, and products of the flap and lead-lag curvatures. These terms are discussed by Mil' (ref. 9) as noted in the introduction; the present equations also include the corresponding nonlinear bending-torsion terms in the flap and lead-lag bending equations (eqs. (4b), (4c)). The flap-lag structural coupling terms in equations (4b) and (4c), with coefficients proportional to $EI_{z'} - EI_{y'}$ are linear and are included in the equations of Houbolt and Brooks. These terms couple flap bending and lead-lag bending elastically when $\theta \neq 0$ and, like the bending-torsion coupling terms, they are proportional to the difference between the lead-lag and flap bending stiffnesses. In some analyses, such as those of references 7, 18, 21, and 22, these terms have been discarded, although they strongly influence the stability characteristics of some hingeless rotor blade configurations.

In general, the flap-lag structural coupling terms are also dependent on blade twist and on bending stiffness distributions in the case of nonuniform blade configurations. In particular, the flap-lag structural coupling is dependent on the relative stiffness of the blade segments inboard and outboard of the pitch bearing. This is because the principal elastic axes of the outboard blade segment rotate through an angle θ as the blade pitch varies while the inboard segment principal axes do not. The resultant effective orientation of principal axes depends on the blade geometry and distribution of bending stiffness inboard and outboard of the pitch bearing. Although the variations in these coupling effects significantly influence stability, they

are not present in the case of a simple single segment uniform beam; they are difficult to include exactly without resorting to a more general blade configuration and a more sophisticated analysis. However, an approximate representation of these effects may be introduced in the present equations with no increase in complexity. This is accomplished by arbitrarily assuming that the average inclination of the principal elastic axes of a nonuniform blade is equal to some fraction of the inclination of the principal axes of a uniform single segment blade. This entails replacing θ by $\mathcal{R}\theta$ in the structural terms in the equations while the mass and inertial terms are unchanged. The factor $\mathcal{R}$ is called the structural coupling parameter. When $\mathcal{R} = 1$, the original equations are retained, but as $\mathcal{R}$ is reduced to zero, the flap-lag structural coupling terms diminish and eventually vanish. The structural coupling parameter $\mathcal{R}$ also influences the bending-torsion structural coupling terms, but to a lesser degree.

As defined here, the structural coupling parameter $\mathcal{R}$ is nearly equivalent (for small pitch angles) to an analogous parameter R used in reference 5 to characterize the variable flap-lag structural coupling of the approximate rigid, hinged blade representation of an elastic blade. Additional discussion of flap-lag structural coupling is given in reference 5.

In their present form, including the nonlinear strain relation, there are five nonlinear equations in u, v, w, ϕ, and T. These equations can be simplified by substitution to eliminate u and T as dependent variables, following the procedure given in references 1, 6, 19, and 20. First, the δu equation is integrated to obtain the tension:

$$T = \frac{m\Omega^2}{2}(R^2 - x^2) + 2m\Omega \int_x^R \dot{v}\, dx \tag{7}$$

This equation is substituted into the δv, δw, and $\delta\phi$ equations to eliminate T. When equation (7) is substituted into the $\delta\phi$ equation, the $2m\Omega \int_x^R \dot{v}\, dx$ term is discarded because it is $O(\varepsilon^3)$. The $2m\Omega\dot{u}$ term in the δv equation is replaced as follows, solving first for u' from equation (5) and substituting equation (7) for T.

$$u' = \frac{m\Omega^2R^2}{EA}\left(\frac{1 - x^2/R^2}{2}\right) + \frac{2m\Omega^2R^2}{EA}\int_x^R \frac{\dot{v}\, dx}{\Omega R^2} - \frac{v'^2}{2} - \frac{w'^2}{2} \tag{8}$$

This is integrated with respect to x and differentiated with respect to t yielding

$$\dot{u} = \frac{2m\Omega^2R^2}{EA}\int_0^x \int_x^R \frac{\ddot{v}}{\Omega^2R^2}\, dx\, dx - \int_0^x (v'\dot{v}' + w'\dot{w}')dx \tag{9}$$

While not essential, it is convenient to discard the first term of equation (9) since $m\Omega^2R^2/EA = O(\varepsilon^2)$ where ε is of the order of magnitude of the bending

slopes. This is equivalent to postulating that the rotor blade is inextensional for perturbation bending deflections; that is, radial shortening of the beam is a purely geometric consequence of the transverse bending deflections of the blade. This assumption is sometimes made on the basis of intuitive reasoning; however, it is strictly valid only for sufficiently large values of the dimensionless radial stiffness, $EA/m\Omega^2R^2$.

After substituting equation (9) into the δv equation (4b), three equations for v, w, and ϕ remain. In the structural terms, θ has been replaced by $\Re\theta$ according to the discussion above.

δv equation:

$$-\frac{m\Omega^2}{2}[v'(R^2-x^2)]' - 2m\Omega\left(v'\int_x^R \dot{v}\,dx\right)' + [EI_{z'} - (EI_{z'} - EI_{y'})\sin^2(\Re\theta)]v'''' + (EI_{z'} - EI_{y'})\frac{\sin(2\Re\theta)}{2}w'''' + (EI_{z'} - EI_{y'})[-\sin(2\Re\theta)(\phi v'')'' + \cos(2\Re\theta)(\phi w'')''] - 2m\Omega\beta_{pc}\dot{w} - 2m\Omega\int_0^x (v'\dot{v}' + w'\dot{w}')dx + m(\ddot{v} - \Omega^2 v) = L_v \quad (10a)$$

δw equation:

$$-\frac{m\Omega^2}{2}[w'(R^2-x^2)]' - 2m\Omega\left(w'\int_x^R \dot{v}\,dx\right)' + [EI_{y'} + (EI_{z'} - EI_{y'})\sin^2(\Re\theta)]w'''' + (EI_{z'} - EI_{y'})\frac{\sin(2\Re\theta)}{2}v'''' + (EI_{z'} - EI_{y'})[\cos(2\Re\theta)(\phi v'')'' + \sin(2\Re\theta)(\phi w'')''] + 2m\Omega\beta_{pc}\dot{v} + m\ddot{w} = L_w - m\Omega^2\beta_{pc}x \quad (10b)$$

$\delta\phi$ equation:

$$-\frac{m\Omega^2}{2}k_A^2[\phi'(R^2-x^2)]' - GJ\phi'' + (EI_{z'} - EI_{y'})\left[(w''^2 - v''^2)\frac{\sin(2\Re\theta)}{2} + v''w''\cos(2\Re\theta)\right] + mk_m^2\ddot{\phi} + m\Omega^2(k_{m_2}^2 - k_{m_1}^2)\phi\cos 2\theta = M_\phi - m\Omega^2(k_{m_2}^2 - k_{m_1}^2)\frac{\sin(2\theta)}{2} \quad (10c)$$

These equations are nonlinear, integro-partial differential equations with variable coefficients in x. In the next section, expressions for L_v, L_w, and M_ϕ, the aerodynamic loading terms, will be derived.

Aerodynamic Loading

The aerodynamic lift and pitching moment acting on the blade in hover are based on Greenberg's extension of Theodorsen's theory (ref. 25) for a two-dimensional airfoil undergoing sinusoidal motion in pulsating incompressible flow. The rotor blade aerodynamic forces are formulated from strip theory in which only the velocity component perpendicular to the blade spanwise axis (the x'-axis in the deformed blade coordinate system x', y', z' in fig. 5) influences the aerodynamic forces. A quasi-steady approximation of the unsteady theory for low reduced frequency k is employed in which the Theodorsen function C(k) is taken to be unity. The steady induced inflow for the rotor is calculated from classical blade element-momentum theory. These simplifying assumptions are judged to be adequate for low frequency (mainly determined by the blade bending frequencies) stability analyses of a hovering rotor.

In Theodorsen's theory (ref. 26), a two-dimensional airfoil is assumed to be pivoted about an axis which may be distinct, in general, from the aerodynamic center axis. The airfoil is pitched at an angle $\varepsilon(t)$ to the free stream flowing at constant velocity V. The airfoil is vertically displaced with velocity $\dot{h}(t)$ positive downward as shown in figure 5. Greenberg has extended Theodorsen's theory for pulsating free-stream velocity V(t). The relations for lift and pitching moment per unit length may be expressed in terms of the circulatory and noncirculatory components

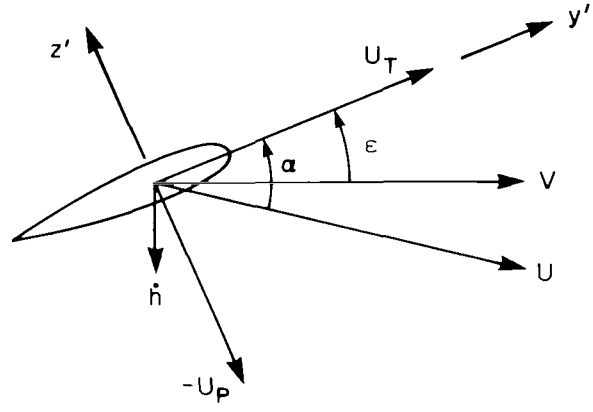

Figure 5.- Rotor blade airfoil section in general unsteady motion.

$$\left.\begin{aligned} L &= L_C + L_{NC} \\ M &= M_C + M_{NC} \end{aligned}\right\} \tag{11}$$

With the airfoil pivot axis (analogous to the rotor blade elastic axis) at the airfoil quarter chord (the airfoil aerodynamic center) these components are

$$\left.\begin{aligned} L_{NC} &= \frac{\rho_\infty ac}{2}\frac{c}{4}\left(\ddot{h} + V\dot{\varepsilon} + \dot{V}\varepsilon + \frac{c}{4}\ddot{\varepsilon}\right) \\ L_C &= \frac{\rho_\infty ac}{2} V\left(\dot{h} + V\varepsilon + \frac{c}{2}\dot{\varepsilon}\right) \\ M_{NC} &= -\frac{c}{4}L_{NC} - \frac{\rho_\infty ac}{2}\left(\frac{c}{4}\right)^3\frac{\ddot{\varepsilon}}{2} \\ M_C &= -\frac{\rho_\infty ac}{2}\left(\frac{c}{4}\right)^2 V\dot{\varepsilon} \end{aligned}\right\} \tag{12}$$

The Theodorsen function $C(k)$ has been set equal to unity in the circulatory lift. It should be noted that ε is the angular position of the airfoil with respect to space; $\dot{\varepsilon}$ and $\ddot{\varepsilon}$ are the angular velocity and angular acceleration of the airfoil. The instantaneous angle of attack of the airfoil $\alpha = \tan^{-1}(U_P/U_T)$ is the angle between the airfoil chord line and the resultant fluid velocity U of the airfoil. The airfoil velocity components in the principal axis system y', z' are U_T and U_P shown in figure 5. It is desirable to express the aerodynamic forces and moments in terms of U_P and U_T. Assuming that the angles ε and α are small yields

$$\left.\begin{aligned} U_P &\cong -\dot{h} - V\varepsilon \\ U &= \sqrt{U_T^2 + U_P^2} \cong V \end{aligned}\right\} \tag{13}$$

Substitution of equations (13) into equations (12) yields

$$\left.\begin{aligned} L_{NC} &= \frac{\rho_\infty ac}{2}\frac{c}{4}\left(-\dot{U}_P + \frac{c}{4}\ddot{\varepsilon}\right) \\ L_C &= \frac{\rho_\infty ac}{2}U\left(-U_P + \frac{c}{2}\dot{\varepsilon}\right) \end{aligned}\right\} \tag{14}$$

Next we consider the total aerodynamic forces in directions parallel and perpendicular to the airfoil chord line. The noncirculatory lift is taken to act normal to the chordline, and the circulatory lift is taken to act normal to the resultant blade velocity U. An aerodynamic profile drag force per unit length, acting parallel to the resultant blade velocity, is included based on a constant profile drag coefficient c_{d_0}.

$$D = \frac{\rho_\infty ac}{2}\frac{c_{d_0}}{a}(U_T^2 + U_P^2) \tag{15}$$

The force components and directions are shown in figure 6. The force components T, normal to the airfoil chord line, and S, parallel to the airfoil chord line, are therefore

$$\left.\begin{aligned} T &= L_C \cos\alpha + L_{NC} + D\sin\alpha \\ S &= -L_C \sin\alpha - D\cos\alpha \end{aligned}\right\} \tag{16}$$

From figure 5,

$$\left.\begin{aligned} \cos\alpha &= \frac{U_T}{U} = \frac{U_T}{\sqrt{U_T^2 + U_P^2}} \\ \sin\alpha &= \frac{U_P}{U} = \frac{U_P}{\sqrt{U_T^2 + U_P^2}} \end{aligned}\right\}$$

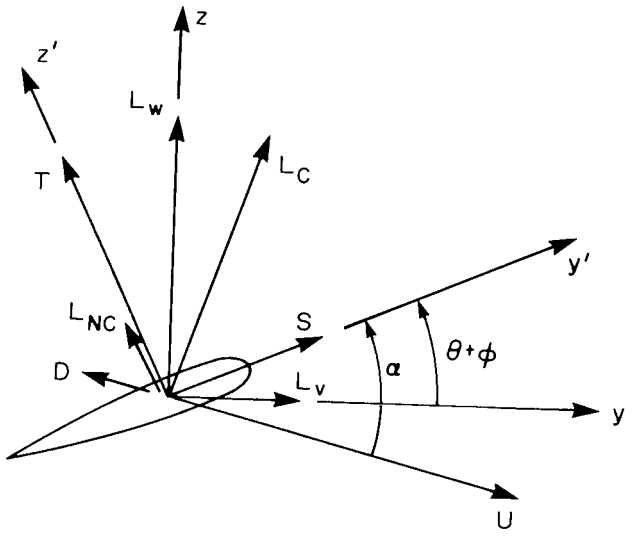

Figure 6.- Orientation of components of aerodynamic loading.

Substitution of equations (14), (15), and (17) into equations (16), with c_{d_0}/a neglected with respect to unity, yields

$$\left.\begin{aligned} T &= \frac{\rho_\infty ac}{2}\left[-U_P U_T + \frac{c}{2}U_T\dot{\varepsilon} - \frac{c}{4}\dot{U}_P + \left(\frac{c}{4}\right)^2\ddot{\varepsilon}\right] \\ S &= \frac{\rho_\infty ac}{2}\left(U_P{}^2 - \frac{c}{2}U_P\dot{\varepsilon} - \frac{c_{d_0}}{a}U_T{}^2\right) \end{aligned}\right\} \tag{18}$$

The expressions for aerodynamic pitching moment components may be written from equations (12) and (13) as

$$\left.\begin{aligned} M_{NC} &= -\frac{\rho_\infty ac}{2}\left(\frac{c}{4}\right)^2\left(-\dot{U}_P + \frac{3c}{8}\ddot{\varepsilon}\right) \\ M_C &\cong -\frac{\rho_\infty ac}{2}\left(\frac{c}{4}\right)^2 U_T\dot{\varepsilon} \end{aligned}\right\} \tag{19}$$

where U has been approximated by U_T in M_C. The total pitching moment is then given by

$$M_\phi = M \cong \frac{\rho_\infty ac}{2}\left(\frac{c}{4}\right)^2\left(U_T\dot{\varepsilon} - \dot{U}_P + \frac{3c}{8}\ddot{\varepsilon}\right) \tag{20}$$

In appendix A, U_P, U_T, and $\dot{\varepsilon}$ are expressed in terms of v, w, and ϕ to the appropriate order of magnitude. From equations (A3) and (A9) we have

$$
\left.
\begin{aligned}
U_P &\cong -\Omega x\left(\theta + \phi + \underline{\int_0^x v'w''\,dx}\right) - (\theta + \phi)\dot{v} + v_i + \dot{w} + \underline{\Omega v(\beta_{pc} + w')} \\
U_T &\cong \Omega x + \dot{v} \\
\dot{\varepsilon} &\cong \dot{\phi} + \Omega(\beta_{pc} + w')
\end{aligned}
\right\} \quad (21)
$$

where v_i is the induced inflow velocity. The underlined terms in U_P produce second order terms in the angle of attack; they are discussed in detail in reference 24. These terms have been shown to influence significantly the flap-lag-torsion stability of cantilever rotor blades (ref. 20). The transformation [T] may also be used to resolve the blade forces S and T into L_V and L_W parallel to the y and z axes of the undeformed blade coordinate system. Retaining terms to the appropriate order of magnitude yields

$$
\left.
\begin{aligned}
L_V &= S - T(\theta + \phi) \\
L_W &= T + S(\theta + \phi)
\end{aligned}
\right\} \quad (22)
$$

Substitution of equations (21) into equation (20) and equations (18) and (21) into equations (22) yields the following expressions for L_V, L_W, and M:

$$
\left.
\begin{aligned}
L_V &\cong \frac{\rho_\infty ac}{2}\left\{v_i^2 - \Omega^2x^2\frac{c_{d_0}}{a} - \Omega x v_i(\theta + \phi) - \underline{\left[2\Omega x\frac{c_{d_0}}{a} + (\theta + \phi)v_i\right]}\dot{v}\right. \\
&\qquad \left. + [2v_i - \Omega x(\theta + \phi)]\dot{w}\right\} \\
L_W &\cong \frac{\rho_\infty ac}{2}\left\{-\Omega x v_i + \Omega^2x^2\left(\theta + \phi + \underline{\int_0^x v'w''}\right) - \underline{\Omega^2 x v(\beta_{pc} + w')}\right. \\
&\qquad + \Omega^2\frac{xc}{2}(\beta_{pc} + w') + [2\Omega x(\theta + \phi) - v_i]\dot{v} - \Omega x\dot{w} \\
&\qquad \left. + \frac{3c}{4}\Omega x\dot{\phi} - \frac{c}{4}\ddot{w}\right\} \\
M_\phi &\cong -\underline{\frac{\rho_\infty ac}{2}\left(\frac{c^2}{8}\Omega x\dot{\phi}\right)}
\end{aligned}
\right\} \quad (23)
$$

Nonlinear rate product terms $\dot{v}\dot{w}$, $\dot{v}^2$, and $\dot{w}^2$ are neglected since they do not contribute in a linearized stability analysis. Also, all $O(\varepsilon^3)$ terms, except those that contribute to lead-lag or torsion damping (double underlined), are neglected (including $\ddot{\varepsilon}$ terms). The single underlined terms are the second order angle of attack terms noted above. The induced inflow v_i is taken to be steady and uniform along the blade radius equal to the value of nonuniform

inflow given by blade element momentum theory at the radial station $x = 0.75R$ (ref. 27). The blade angle at $x = 0.75R$ is set equal to the blade collective pitch plus the equilibrium elastic twist ϕ_0 at $x = 0.75R$. Thus

$$v_i = \text{sgn}[\theta + \phi_0(0.75R)]\Omega R \frac{\pi\sigma}{8}\left(\sqrt{1 + \frac{12}{\pi\sigma}\left|\theta + \phi_0(0.75R)\right|} - 1\right) \tag{24}$$

where σ is the blade solidity $bc/\pi R$.

Solution of the Equations of Motion

In this section we describe the solution of the final flap-lag-torsion equations of motion obtained by combining equations (10) and (23). These nonlinear, variable coefficient, integro-partial differential equations are solved by Galerkin's method using six coupled, rotating mode shapes to evaluate the stability of small perturbation motions about the equilibrium operating condition. These coupled, rotating mode shapes are determined by first calculating the equilibrium position and formulating the stability analysis in terms of standard, uncoupled, nonrotating cantilever beam mode shapes. The coupled mode shapes are then determined from an approximate free vibration analysis (*in vacuo*) of the rotating beam about the deformed shape of the equilibrium operating condition.

We begin by first reducing the equations of motion to ordinary differential equations by Galerkin's method. The dimensionless bending ($\bar{v} = v/R$, $\bar{w} = w/R$) and torsion deflections are first expressed in terms of a series of generalized coordinates and mode shape functions:

$$\left.\begin{aligned} \bar{v} &= \sum_{j=1}^{N} V_j(\psi)\Psi_j(\bar{x}) \\ \bar{w} &= \sum_{j=1}^{N} W_j(\psi)\Psi_j(\bar{x}) \\ \phi &= \sum_{j=1}^{N} \Phi_j(\psi)\Theta_j(\bar{x}) \end{aligned}\right\} \tag{25}$$

where $\psi = \Omega t$ and $\bar{x} = x/R$. This operation yields $3N$ modal equations in terms of modal generalized coordinates V_j, W_j, and Φ_j (appendix B contains the results of this operation). The assumed mode shapes for the bending and torsion deflections are the standard nonrotating, uncoupled mode shapes for a uniform cantilever beam:

$$\left.\begin{aligned} \Psi_j(\bar{x}) &= \cosh(\beta_j\bar{x}) - \cos(\beta_j\bar{x}) - \alpha_j[\sinh(\beta_j\bar{x}) - \sin(\beta_j\bar{x})] \\ \Theta_j(\bar{x}) &= \sqrt{2}\,\sin(\gamma_j\bar{x}) \end{aligned}\right\} \tag{26}$$

The constants α_j and β_j are tabulated in reference 28 and $\gamma_j = \pi(j - 1/2)$. Nonrotating mode shapes are used because of computational ease. Since they depend only on the fixed constants α_j and β_j, and not on EI_y' and EI_z', the modal integrals that result when Galerkin's method is applied need to be calculated only once (see refs. 6 and 19, for example). Furthermore, many of the modal integrals have closed form solutions in terms of α_j and β_j (ref. 29).

The 3N nonlinear, nonhomogeneous, constant-coefficient ordinary differential equations are then linearized for small perturbation motions about the equilibrium operating condition by expressing the time-dependent generalized coordinates in terms of steady equilibrium quantities and small unsteady perturbation quantities.

$$\left.\begin{aligned} V_j(\psi) &= V_{0j} + \Delta V_j(\psi) \\ W_j(\psi) &= W_{0j} + \Delta W_j(\psi) \\ \Phi_j(\psi) &= \Phi_{0j} + \Delta\Phi_j(\psi) \end{aligned}\right\} \tag{27}$$

Two sets of equations are obtained from this operation. First, substituting only the steady equilibrium quantities into the nonlinear modal equations yields 3N nonlinear algebraic equations in V_{0j}, W_{0j}, and Φ_{0j} (given in appendix B) which define the equilibrium deflections. These equilibrium equations are solved by the Newton-Raphson method. The second set of 3N equations is obtained by substituting equations (27) into the modal equations, subtracting the equilibrium equations, and discarding all nonlinear products of perturbation quantities. The coefficients of these linearized perturbation equations are functions of the equilibrium solution. The perturbation equations define the unsteady blade motion near the equilibrium operating condition and the stability of this motion is determined using standard techniques. The perturbation equations are linear, homogeneous, constant-coefficient ordinary differential equations of the form

$$[M]\{\ddot{X}\} + [C]\{\dot{X}\} + [K]\{X\} = 0 \tag{28}$$

where [M] is symmetric, and where [C] and [K] are asymmetric and depend on V_{0j}, W_{0j}, and Φ_{0j}. Each matrix is 3N × 3N (these matrices are given in appendix B) and the vector {X} is of length 3N and is given by

$$\{X\} = \begin{Bmatrix} \Delta V_j \\ \Delta W_j \\ \Delta\Phi_j \end{Bmatrix} \tag{29}$$

The stability of motion about the equilibrium operating condition is determined by the eigenvalues of the 6N × 6N matrix [P] where

$$\begin{Bmatrix} \dot{X} \\ \ddot{X} \end{Bmatrix} = \begin{bmatrix} 0 & I \\ -M^{-1}K & -M^{-1}C \end{bmatrix} \begin{Bmatrix} X \\ \dot{X} \end{Bmatrix} = [P] \begin{Bmatrix} X \\ \dot{X} \end{Bmatrix} \tag{30}$$

Since we are primarily concerned with lower frequency instabilities (first lead-lag, first flap, and first torsion frequencies), there is a value of N for which any increase in N will not appreciably change the eigenvalues associated with these lower frequencies. It is at this value of N that the eigenvalues are considered to be converged. For practical hingeless rotor configurations, N = 5 gives suitably converged eigenvalues; the matrix [P] is thus 30 × 30. By a change of modal coordinates, the size of the matrix [P] may be greatly reduced without significantly changing the eigenvalues of interest. Such a transformation may be found by first considering free vibrations (*in vacuo*) of the blade about the equilibrium deflected state. The equation of motion, analogous to equation (28), is

$$[M]\{\ddot{X}\} + [G]\{\dot{X}\} + [K_v]\{X\} = 0 \tag{31}$$

where the subscript v implies the vacuum case. Both [M] and $[K_v]$ are symmetric; $[K_v]$ is equal to [K] with all aerodynamic terms set equal to zero, and [G] is antisymmetric and equal to [C] with all aerodynamic terms set equal to zero. The presence of the matrix [G] causes the eigenvectors of the free vibration to be complex. This may be avoided for computational efficiency by approximating equation (31) as

$$[M]\{\ddot{X}\} + [K_v]\{X\} = 0 \tag{32}$$

The matrix of eigenvectors [U] for equation (32) is orthogonal with respect to [M]. Thus,

$$[U]^T[M][U] = [I] \tag{33}$$

According to Meirovitch (ref. 30) a so-called principal coordinate transformation for equation (28) may be determined by replacing {X} by [U]{X}. We may then pre-multiply equation (28) by $[U]^T$ to take advantage of the form of equation (33) yielding

$$[I]\{\ddot{X}\} + [U^TCU]\{\dot{X}\} + [U^TKU]\{X\} = 0 \tag{34}$$

Hence,

$$\begin{Bmatrix} \dot{X} \\ \ddot{X} \end{Bmatrix} = \begin{bmatrix} 0 & I \\ -U^TKU & -U^TCU \end{bmatrix} \begin{Bmatrix} X \\ \dot{X} \end{Bmatrix} = [P^*] \begin{Bmatrix} X \\ \dot{X} \end{Bmatrix} \tag{35}$$

The matrices [P] and [P*] have the same eigenvalues. However, because of the nature of this modal coordinate transformation from [P] to [P*], the rows and columns corresponding to high frequency modes of both $[U^TKU]$ and $[U^TCU]$ may be removed without affecting the eigenvalues of the low frequency modes of interest. These 3N × 3N matrices are thus reduced to M × M matrices whose

rows and columns correspond to the M low frequency modes that are retained. The rows and columns that are retained in $[U^TKU]$ and $[U^TCU]$ may be chosen in two ways: (1) the M rows and columns that correspond to the M lowest frequency modes of the blade may be retained, or (2) the M rows and columns that correspond to M modes selected arbitrarily from the lowest lead-lag, the lowest flap, and the lowest torsion frequency modes are retained. For the second case, under certain conditions, M = 3, 4, or 5 will result in converged eigenvalues. In either case, suitably converged results do not require $M > 6$.

The reduced matrices are analogous to stiffness and damping matrices generated from M coupled, rotating modes. Since the analysis is formulated in terms of standard cantilever mode shapes, however, repeated numerical integration of modal integrals is not necessary for different values of beam stiffnesses. Instead, the matrix operations described above lead to a net savings in CPU time. For all results given in this report, M = 6 unless otherwise noted. Thus $[P^*]$ is reduced from $6N \times 6N$ (30×30) to $2M \times 2M$ (12×12). Eigenvalues may be calculated from a 12×12 matrix in less than 10 percent of the time required for a 30×30. The total savings in CPU time is about 60 percent for each case including the equilibrium solution, the above modal analysis, and the eigenvalues for the perturbation equations.

Approximate Equations of Motion

The flap-lag-torsion equations may be considered as an extension of the earlier flap-lag equations of reference 6. They permit the analysis of torsionally flexible rotor blades, but also introduce additional equations and degrees of freedom for the torsion generalized coordinates. It is possible to reduce the flap-lag-torsion equations to an approximate set of modified flap-lag equations and still retain the most important effects of torsional flexibility. This is possible because the structural terms in the torsion equation are usually large compared to the inertial and aerodynamic damping terms. Based on order of magnitude considerations, the $\ddot{\Phi}_j$ and $\dot{\Phi}_j$ terms are small in comparison to the Φ_j terms when ω_ϕ is sufficiently large. The approximation simply consists of discarding the $\ddot{\Phi}_j$ and $\dot{\Phi}_j$ terms in the torsion modal equations leaving (in addition to the tension-torsion and tennis racket terms) the torsion rigidity term proportional to Φ_j and the bending-torsion structural terms proportional to products of the bending generalized coordinates V_j and W_j. This permits Φ_j to be expressed in terms of V_j and W_j and permits Φ_j to be substituted into the flap and lead-lag modal equations. This reduces the number of equations and eliminates the torsion generalized coordinates Φ_j as independent degrees of freedom. The accuracy and limits of validity of the resulting modified flap-lag equations will be examined below.

SELECTION OF CONFIGURATION PARAMETERS

A few brief comments are in order to explain clearly the choice of the blade configuration parameters. These consist of the structural and inertia

parameters $EI_y'/m\Omega^2R^4$, $EI_z'/m\Omega^2R^4$, $GJ/m\Omega^2R^4$, k_A/k_m, k_m/R, k_{m_1}/k_{m_2}, and $\mathcal{R}$, and the geometric and aerodynamic parameters c/R, β_{pc}, and σ, and the Lock number $\gamma = 3\rho_\infty acR/m$. The pitch angle θ is considered to be the control parameter defining the rotor operating condition; that is, the rotor thrust.

Beginning with the geometric and aerodynamic parameters, typical values are chosen as follows: the Lock number $\gamma = 5.0$ and the solidity $\sigma = 0.10$. Since $\sigma = bc/\pi R$, the choice of a four blade rotor ($b = 4$) yields the dimensionless chord ratio $c/R = \pi/40$. The geometric blade precone angle β_{pc} has an important influence on stability, and thus a range of values will be investigated.

The structural and inertial parameters mainly determine the natural frequencies of the blade which in turn serve as rotor blade configuration parameters. In general, explicit expressions do not exist for the structural and inertial parameters in terms of the blade natural frequencies, and it is necessary to solve for these parameters iteratively if the natural frequencies are specified. In this report, the following procedure is used. For an untwisted cantilever beam with uniform mass and stiffness, the structural and inertial parameters are first expressed explicitly in terms of the uncoupled natural frequencies for the nonrotating condition. These relationships are

$$\frac{EI_z'}{m\Omega^2R^4} = \frac{\omega_{v_{NR}}^2}{\beta_1^4}, \qquad \frac{EI_y'}{m\Omega^2R^4} = \frac{\omega_{w_{NR}}^2}{\beta_1^4}, \qquad \frac{GJ}{m\Omega^2k_m^2R^2} = \frac{\omega_{\phi_{NR}}^2}{\gamma_1^2} \tag{36}$$

where the subscript NR refers to frequencies of the nonrotating beam. The nonrotating frequencies are then used as an intermediate step in determining the uncoupled (at $\theta = 0$), rotating natural frequencies. For an untwisted uniform cantilever beam, the rotating bending frequencies may be accurately expressed in terms of the nonrotating frequencies using the approximate analytical relations developed in reference 31. These relationships are shown in figures 7 and 8. An analogous relationship for the rotating and nonrotating torsion frequencies, also derived in reference 31, depends on the intensity of tension-torsion coupling that is proportional to k_A^2/k_m^2, and the inertia ratio k_{m_1}/k_{m_2}. This result is shown in figure 9 based on a choice of $k_A^2/k_m^2 = 1.5$ and $k_{m_1}/k_{m_2} = 0.0$. The remaining torsion inertia parameter, the mass radius of

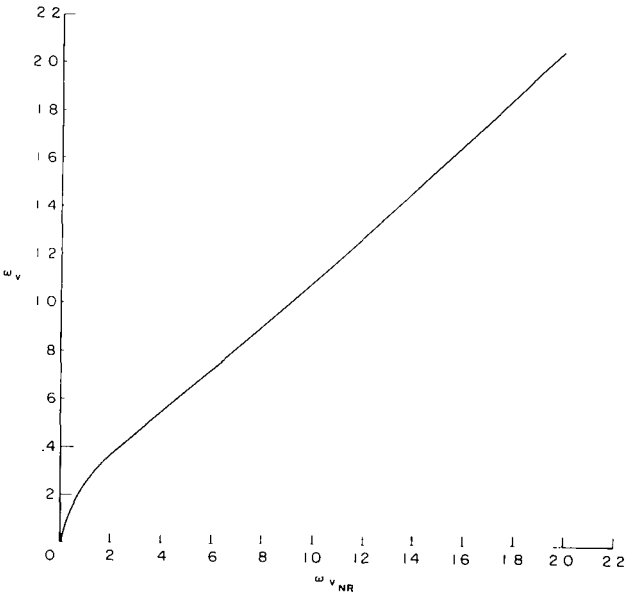

Figure 7.- Rotating lead-lag frequency versus nonrotating lead-lag frequency: $\theta = 0.0$.

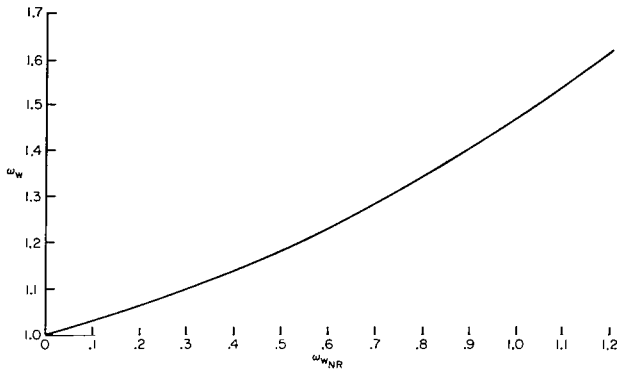

Figure 8.- Rotating flap frequency versus nonrotating flap frequency: $\theta = 0$.

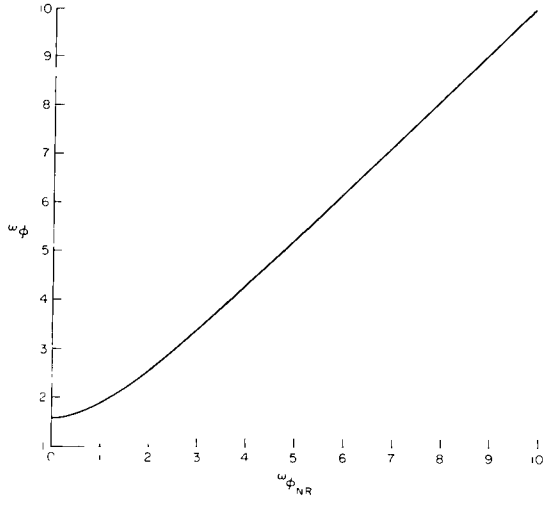

Figure 9.- Rotating torsion frequency versus nonrotating torsion frequency; $\theta = 0.0$, $k_{m_1}/k_{m_2} = 0.0$, and $k_A^2/k_m^2 = 1.5$.

gyration k_m/R, is taken to be 0.025. Therefore, any choice of the three fundamental rotating frequencies, together with the values for k_A^2/k_m^2, k_{m_1}/k_{m_2}, and k_m/R given here and the frequency variations of figures 7-9, will yield the appropriate values of $EI_y'/m\Omega^2R^4$, $EI_z'/m\Omega^2R^4$, $GJ/m\Omega^2R^4$, k_A^2/k_m^2, k_{m_1}/k_{m_2}, and k_m/R for the equations of motion.

Values for the blade natural frequencies will be chosen as follows. The dimensionless flap natural frequency typically lies between 1.1 and 1.2; for the present results ω_w is taken to be 1.15. The dimensionless lead-lag natural frequency ω_v typically falls into one of two ranges: 0.5 to 0.75 for soft inplane ($\omega_v < 1.0$) configurations and 1.2 to 1.7 for stiff inplane ($\omega_v > 1.0$) configurations. Two typical values, $\omega_v = 0.7$ and 1.5, are chosen here. Since $EI_y'/EI_z' = 0(1)$ was assumed from the outset in deriving the equations, the validity of the equations is limited to $\omega_v \lesssim 3$ (i.e., the practical range). To analyze configurations with larger ω_v, one should refer to reference 1 and rederive the equations based on a different ordering scheme, such as $EI_z'/m\Omega^2R^4 = 0(\epsilon^{-1})$. This will introduce additional terms and the equations will then be valid for larger values of ω_v. The dimensionless torsion natural frequency ω_ϕ usually ranges from 2.5 to 8.0. We will use 5.0 as a typical value and include results for other values as well.

The structural coupling parameter $\mathfrak{K}$ will arbitrarily be given various values between 0.0 and 1.0. It is not possible to relate this parameter in a simple way to the stiffness distribution characteristics of actual rotor blades and the results can only indicate the range of behavior that may be encountered.

In solving the equations using assumed mode shapes, the modal parameters are important. Unless otherwise specified, six coupled rotating mode shapes

(M = 6) will be used, thus producing six degrees of freedom. These are based on the free vibration analysis using 15 (3N) uncoupled nonrotating mode shapes. The six coupled rotating mode shapes retained are the six lowest frequency modes. The various parameter values discussed above are summarized in table 2.

TABLE 2.- VALUES OF CONFIGURATION AND OPERATING CONDITION PARAMETERS USED FOR NUMERICAL RESULTS

	Baseline values	Additional values
ω_v	0.7, 1.5	Variable
ω_w	1.15	---
ω_ϕ	2.5, 5.0, 8.0	Variable
$(k_A/k_m)^2$	1.5	---
θ, rad	0.0	Variable 0.0 - 0.5
β_{pc}, rad	0.0, 0.05, 0.1	Variable
μ	0.0, 0.4, 1.0	Variable 0.0 - 1.0
k_m/R	0.025	---
k_{m_1}/k_{m_2}	0.0	---
$\gamma = (3\rho_\infty acR/m)$	5	---
σ	0.10	---
c/R	$\pi/40$	---
b	4	---
c_{d_0}/a	$0.01/2\pi$	---
M	6	2-5

RESULTS

Steady State Deflections

The steady state equilibrium deflections of the rotor blade must be determined because they contribute to the coefficients of the linearized perturbation equations. The equilibrium deflections are required also to define precisely the operating condition of the rotor. This is because the total blade angle, which determines the rotor thrust in hover, is equal to the blade pitch angle θ plus the equilibrium elastic torsional deflection of the blade ϕ_0. A few results are given to indicate the general behavior of the equilibrium deflections and the influence of several configuration parameters. The results are given in terms of the dimensionless tip deflections that are related to the equilibrium generalized coordinates by the following relations:

$$\left.\begin{aligned} \bar{v}_0\Big|_{tip} &= 2\sum_{j=1}^{N} V_{0j}(-1)^{j+1} \\ \bar{w}_0\Big|_{tip} &= 2\sum_{j=1}^{N} W_{0j}(-1)^{j+1} \\ \phi_0\Big|_{tip} &= \sqrt{2}\sum_{j=1}^{N} \Phi_{0j}(-1)^{j+1} \end{aligned}\right\} \tag{37}$$

The blade pitch angle θ is varied throughout the nominal range of thrust including very high thrust conditions ($\theta > 0.3$ implies that $C_T/\sigma > 0.17$).

The results given in figures 10 and 11 show the equilibrium deflections of a soft and a stiff inplane rotor blade as a function of the pitch angle θ for several values of the structural coupling parameter $\mathcal{R}$. Increasing θ increases the aerodynamic forces acting on the blade and generally increases the magnitude of the equilibrium deflections. The structural coupling parameter $\mathcal{R}$ has little direct effect on the equilibrium flap deflection $\bar{w}_0\Big|_{tip}$, although the variation of $\phi_0\Big|_{tip}$ does change the blade angle and thus indirectly influences $\bar{w}_0\Big|_{tip}$. The lead lag deflection is directly influenced by $\mathcal{R}$ as a result of the flap-lag structural coupling. When $\mathcal{R} \neq 0$ and $EI_z' > EI_y'$, the blade tends to bend in a direction normal to the airfoil chord so that negative $\bar{v}_0\Big|_{tip}$ deflections are produced by positive $\bar{w}_0\Big|_{tip}$ deflections when $\theta > 0$. This is evident in figures 10 and 11 by the increasingly negative values of $\bar{v}_0\Big|_{tip}$ as $\mathcal{R}$ varies from 0 to 1.0.

The equilibrium torsion deflection $\phi_0\Big|_{tip}$ depends on a combination of inertial and structural moments. First the inertial term, or tennis racket effect, that is independent of $\mathcal{R}$ dominates the torsion moments at small pitch angles. This term produces a negative equilibrium torsion deflection proportional to θ at small pitch angles that is clearly evident in figures 10 and 11. Second, the structural torsion moments strongly influence the equilibrium torsion deflection, but in a complex manner. In the torsion equation, the bending-torsion structural coupling terms are nonlinear products of the bending deflections. Thus, parameters that influence the equilibrium values of $\bar{v}_0\Big|_{tip}$ and $\bar{w}_0\Big|_{tip}$ similarly influence the equilibrium torsion

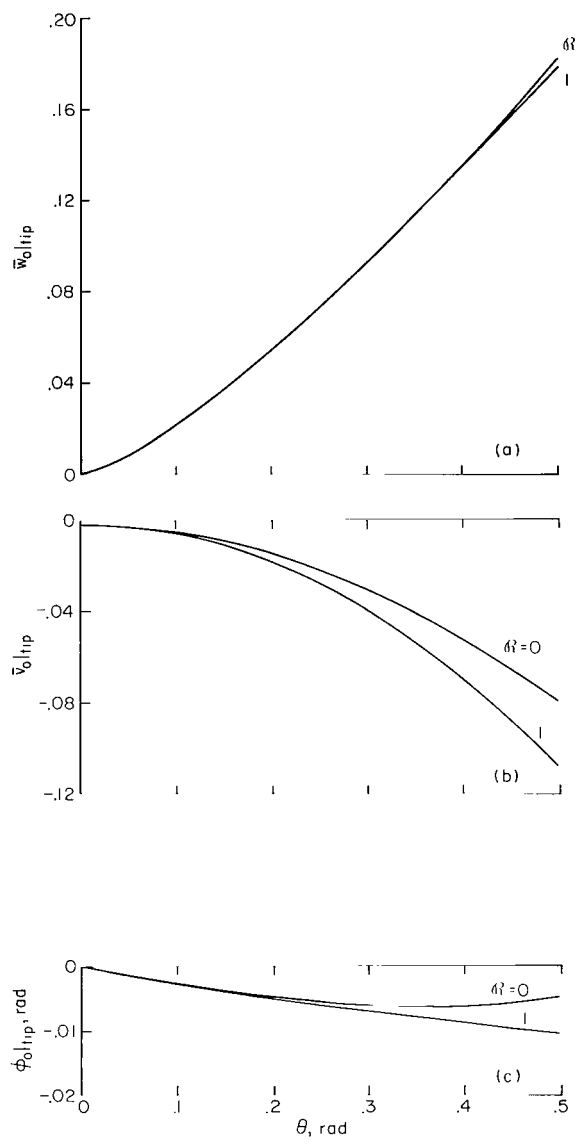

(a) Flap bending.
(b) Lead-lag bending.
(c) Torsion.

Figure 10.- The effect of pitch angle and $\mathfrak{R}$ on the equilibrium deflections of a soft inplane rotor blade: $\omega_v = 0.7$, $\omega_\phi = 5.0$, $\beta_{pc} = 0.0$ rad.

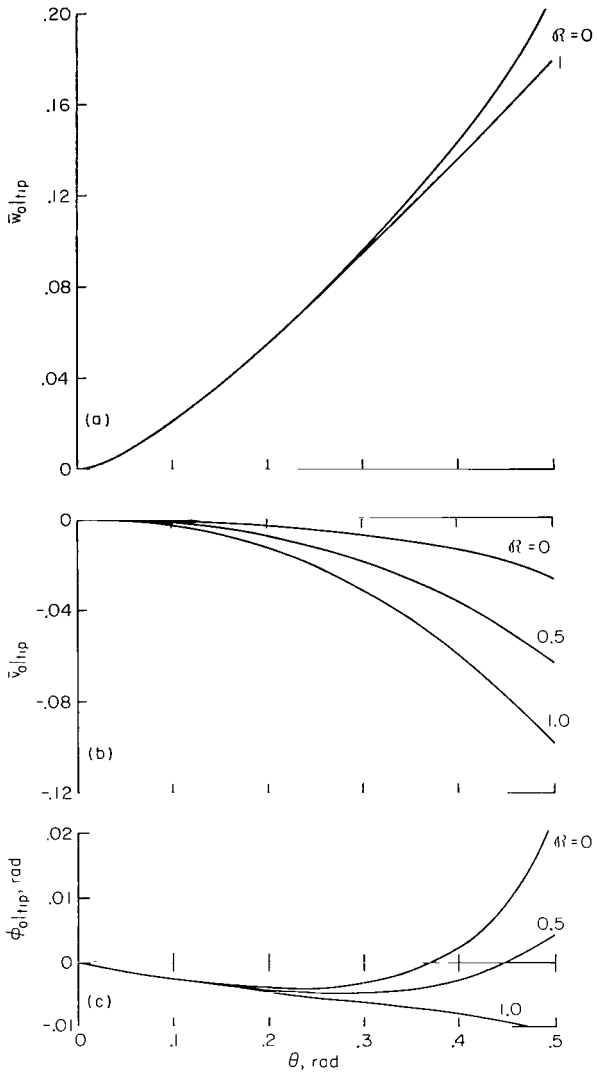

(a) Flap bending.
(b) Lead-lag bending.
(c) Torsion.

Figure 11.- The effect of pitch angle and $\mathfrak{R}$ on the equilibrium deflections of a stiff inplane rotor blade: $\omega_v = 1.5$, $\omega_\phi = 5.0$, $\beta_{pc} = 0.0$ rad.

deflection. To help explain the structural coupling terms that influence the equilibrium torsional deflection, the structural terms of equation (10) are written below.

$$\left.\begin{aligned}
&[EI_{z'} - (EI_{z'} - EI_{y'})\sin^2(\mathcal{R}\theta)]v'''' + (EI_{z'} - EI_{y'})\frac{\sin(2\mathcal{R}\theta)}{2}w'''' \\
&\qquad + (EI_{z'} - EI_{y'})[-\sin(2\mathcal{R}\theta)(\phi v'')'' + \cos(2\mathcal{R}\theta)(\phi w'')''] + \ldots \\
&(EI_{z'} - EI_{y'})\frac{\sin(2\mathcal{R}\theta)}{2}v'''' + [EI_{y'} + (EI_{z'} - EI_{y'})\sin^2(\mathcal{R}\theta)]w'''' \\
&\qquad + (EI_{z'} - EI_{y'})[\cos(2\mathcal{R}\theta)(\phi v'')'' + \sin(2\mathcal{R}\theta)(\phi w'')''] + \ldots \\
&-GJ\phi'' + (EI_{z'} - EI_{y'})\left[\underline{\underline{(w''^2 - v''^2)}}\frac{\sin(2\mathcal{R}\theta)}{2} + \underline{v''w''\cos(2\mathcal{R}\theta)}\right] + \ldots
\end{aligned}\right\} \quad (38)$$

Consider first the case where $\mathcal{R} = 0$ and the flap-lag structural coupling terms vanish. In the torsion equation, the bending-torsion structural moment (singly underlined in eq. (38)) is proportional to the product of the flap and lead-lag bending curvatures. This is a positive torsion moment that counteracts the equilibrium torsion deflection due to the inertial tennis racket effect shown in figures 10 and 11. Furthermore, since the bending-torsion structural coupling is proportional to $EI_{z'} - EI_{y'}$ this effect is larger for the stiff-inplane than for the soft-inplane configuration. In fact, for sufficiently large θ or ω_v, the structural torsion moments can produce a static divergence for low values of $\mathcal{R}$. For the case when $\mathcal{R} \neq 0$, there is another torsional moment (doubly underlined in eq. (38)) that is proportional to squares of the bending curvatures. This moment generally acts to reduce the effect of its companion term; this is evident in figures 10 and 11 as $\mathcal{R}$ varies from 0 to 1.

The two terms together are equivalent to a single product term $(EI_{z'} - EI_{y'})v_p''w_p''$ where v_p and w_p are blade bending deflections in the direction of the blade principal axes. This axis system is obtained simply by rotating the y,z axis system through an angle $\mathcal{R}\theta$. Alternatively, the nonlinear structural torsion moment can also be shown to be proportional to the angle between the resultant direction of the blade bending deflection and the principal elastic axis angle $\mathcal{R}\theta$. As $\mathcal{R}$ increases, this angle, the positive structural torsion moment, and $\phi_0|_{tip}$ are all reduced.

The effects of precone on the equilibrium deflections for a soft inplane and a stiff inplane rotor blade are shown in figures 12 and 13, respectively. Positive precone reduces the elastic flap deflection of the blade because of centrifugal force. For this example, $\mathcal{R} = 1.0$ and flap-lag structural coupling with positive precone generates a positive lead-lag deflection increment due to the negative increment of elastic flap deflection. Similarly, the

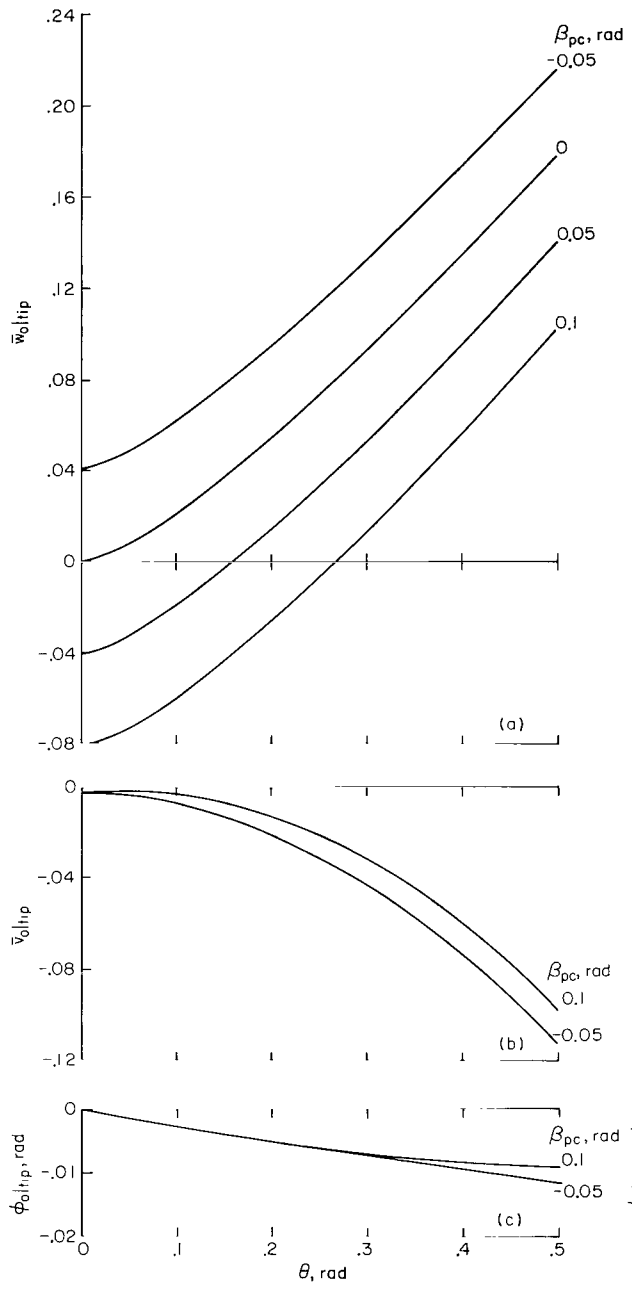

(a) Flap-bending.
(b) Lead-lag bending.
(c) Torsion.

Figure 12.- The effect of pitch angle and precone on the equilibrium deflections of a soft inplane rotor blade: $\omega_v = 0.7$, $\omega_\phi = 5.0$, $\mathcal{R} = 1.0$.

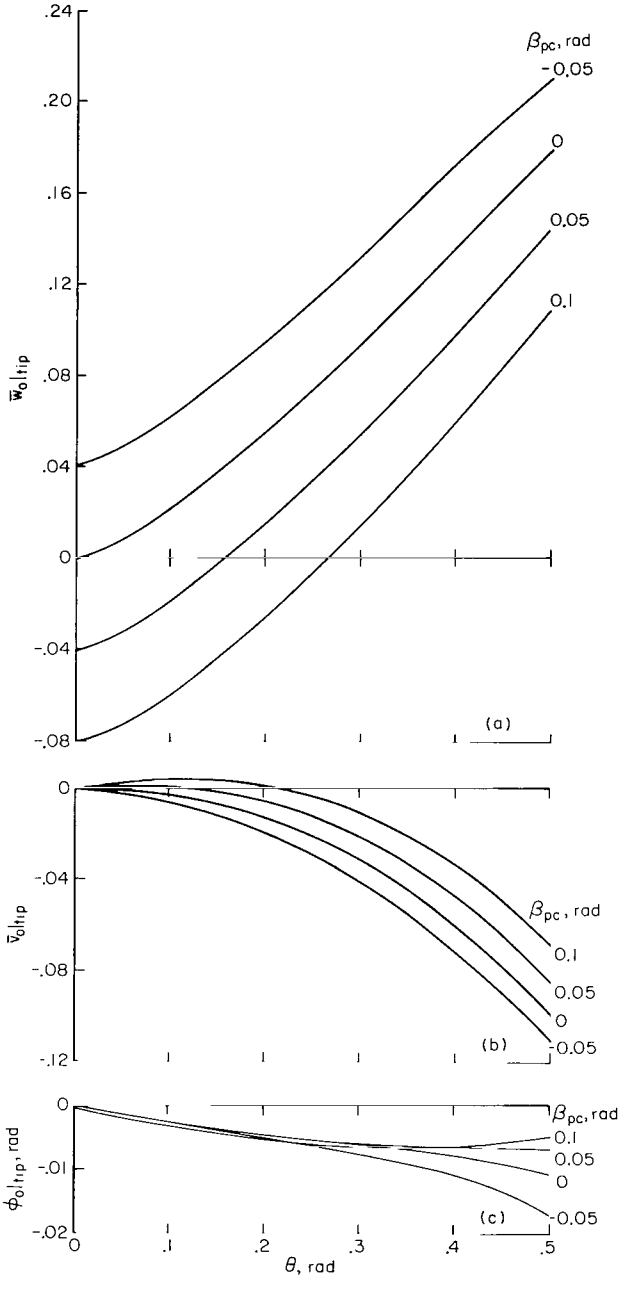

(a) Flap-bending.
(b) Lead-lag bending.
(c) Torsion.

Figure 13.- The effect of pitch angle and precone on the equilibrium deflections of a stiff inplane rotor blade: $\omega_v = 1.5$, $\omega_\phi = 5.0$, $\mathcal{R} = 1.0$.

structural torsion moments, and hence the equilibrium torsion deflections, is influenced by precone.

As noted above, the nonlinear equilibrium equations were solved by the Newton-Raphson method. In some cases, multiple equilibrium solutions were found, but in all cases only the physically relevant solution was statically stable. At high pitch angles, care was required to insure that the numerical scheme converged to the proper solution. This was done by using a previous solution at a lower pitch angle as the initial condition for a solution at a slightly higher pitch angle.

Mechanism of Bending-Torsion Structural Coupling

The equilibrium results showed that the torsion deflection $\phi_0|_{tip}$ is dependent on $\bar{v}_0|_{tip}$ and $\bar{w}_0|_{tip}$ because of nonlinear structural bending-torsion coupling. This coupling also influences the linearized perturbation equations, producing perturbation torsion deflections proportional to perturbation flap and lead-lag bending deflections. This type of coupling is known (ref. 5) to have a strong influence on hingeless rotor blade stability and, therefore, a brief discussion of the equivalent kinematic pitch-flap and pitch-lag couplings generated by the structural coupling is included here.

For simplicity, we consider the perturbation torsion equation for one flap, one lead-lag, and one torsion mode (N = 1), neglecting torsional inertia and damping:

$$\left[\omega_\phi^2 - \left(\frac{k_{m_2}^2 - k_{m_1}^2}{k_m^2}\right)(1 - \cos 2\theta)\right]\Delta\Phi_1 = \frac{-K_{111}(EI_{z'} - EI_{y'})}{m\Omega^2 k_m^2 R^2}\left[(W_{01}\Delta W_1 - V_{01}\Delta V_1)\sin(2\Re\theta) + (V_{01}\Delta W_1 + W_{01}\Delta V_1)\cos(2\Re\theta)\right] \tag{39}$$

where

$$\omega_\phi^2 = \frac{k_{m_2}^2 - k_{m_1}^2}{k_m^2} + \frac{k_A^2}{k_m^2}N_{11} + \frac{GJ\pi^2}{4m\Omega^2 k_m^2 R^2}$$

and the modal integrals defined in appendix B are

$$K_{111} = \int_0^1 \Theta_1 \Psi_1''^2 \, d\bar{x} \cong 5.03911$$

$$N_{11} = \int_0^1 \left(\frac{1 - \bar{x}^2}{2}\right)\Theta_1'^2 \, d\bar{x} \cong 1.07247$$

Taking the ratios of torsion deflection to flap and lead-lag bending deflections yields, for $k_{m_1} = 0$,

$$\left.\begin{aligned}\theta_\beta \cong \frac{1}{\sqrt{2}}\frac{\partial\Delta\Phi_1}{\partial\Delta W_1} &= \frac{-K_{111}(EI_z' - EI_y')}{\sqrt{2}mk_m^2\Omega^2R^2(\omega_\phi^2 - 1 + \cos 2\theta)}\,[V_{01}\cos(2\mathcal{R}\theta) + W_{01}\sin(2\mathcal{R}\theta)] \\ \theta_\zeta \cong \frac{1}{\sqrt{2}}\frac{\partial\Delta\Phi_1}{\partial\Delta V_1} &= \frac{-K_{111}(EI_z' - EI_y')}{\sqrt{2}mk_m^2\Omega^2R^2(\omega_\phi^2 - 1 + \cos 2\theta)}\,[-V_{01}\sin(2\mathcal{R}\theta) + W_{01}\cos(2\mathcal{R}\theta)]\end{aligned}\right\} \quad (40)$$

where θ_β and θ_ζ are defined as the equivalent kinematic pitch-lag and pitch-flap couplings due to the structural properties of the blade. They depend on the equilibrium bending deflections of the blade, the difference in lead-lag and flap and bending stiffness $EI_z' - EI_y'$, the torsion frequency ω_ϕ, and the structural coupling parameter $\mathcal{R}$. For matched stiffness ($EI_z' = EI_y'$) configurations, these couplings vanish. For soft- and stiff-inplane rotor blade configurations, they are small and large, respectively. Both torsion frequency and precone influence these coupling terms. For very high torsion frequencies ($\omega_\phi > 20$) the couplings are normally small and unimportant, but for typical values of torsion frequency ($5 \le \omega_\phi \le 10$) they are important. Precone affects the couplings via the equilibrium bending deflections of the blades as discussed previously. At low pitch angles, positive precone can make $\bar{w}_0|_{tip}$ negative and change the sign of the pitch-lag coupling. For many rotor blade configurations this will produce instability. Figure 14 shows

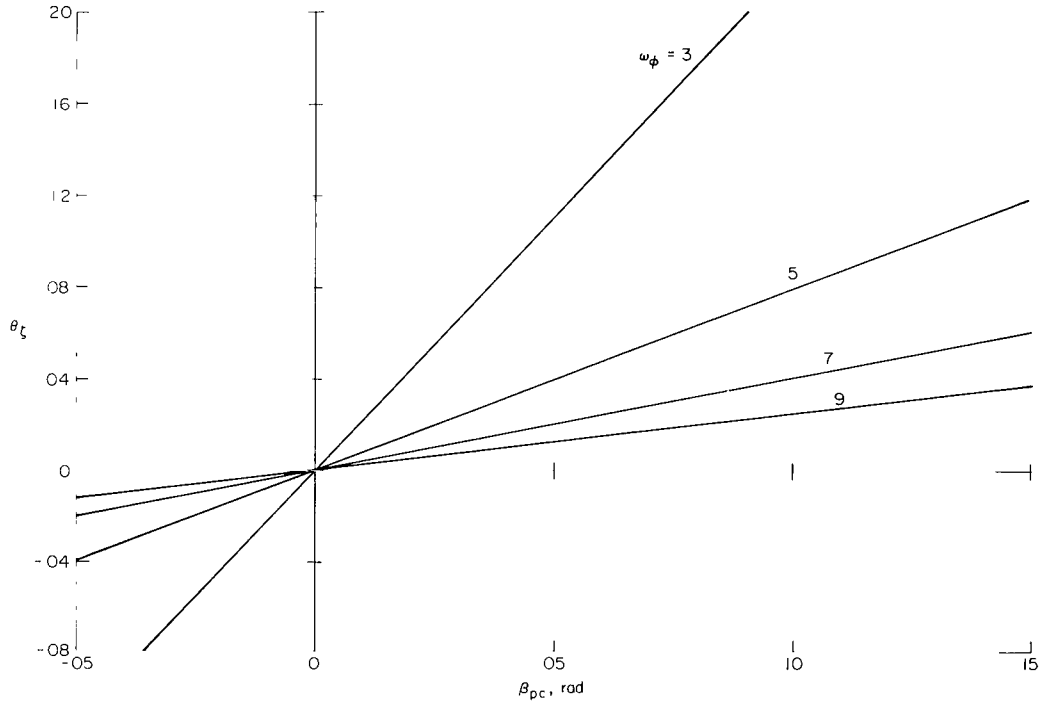

Figure 14.- The effect of torsion frequency and precone on the equivalent pitch-lag coupling for zero pitch angle: $\omega_v = 0.7$, $\mathcal{R} = 0.0$, $\theta = 0.0$ rad.

typical changes in the sign of θ_ζ at $\theta = 0$ and its linear dependence on precone. Finally, the structural coupling parameter $\mathcal{R}$ affects θ_β and θ_ζ by altering the orientation of the principal elastic axes of the blade. Variation of $\mathcal{R}$ from 0 to 1.0 can change the sign of θ_β. The quantitative variation of the equivalent kinematic pitch-flap and pitch-lag coupling is shown in figures 15-18.

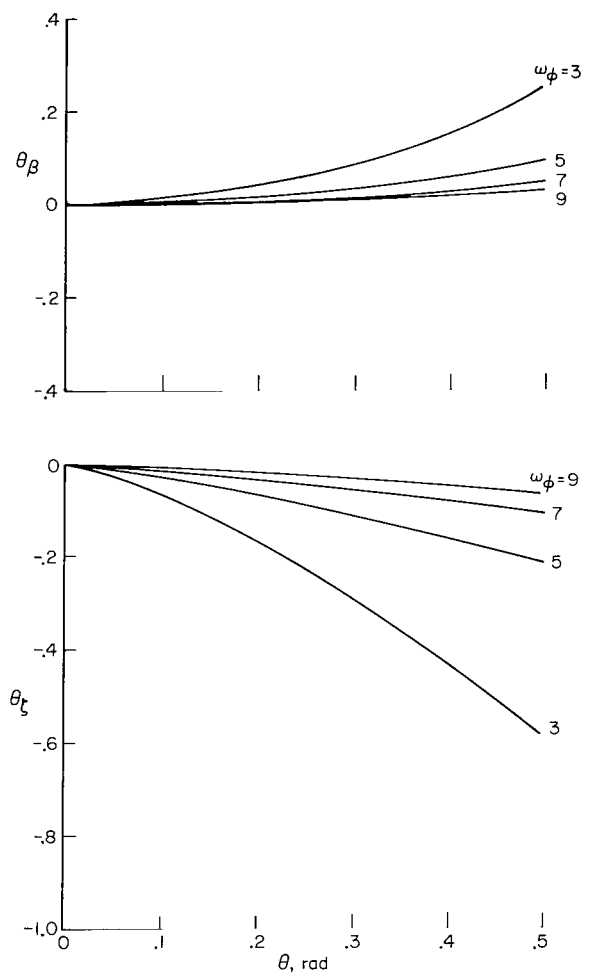

Figure 15.- Equivalent pitch-flap and pitch-lag coupling for a soft inplane rotor blade: $\omega_v = 0.7$, $\mathcal{R} = 0.0$, $\beta_{pc} = 0.0$ rad.

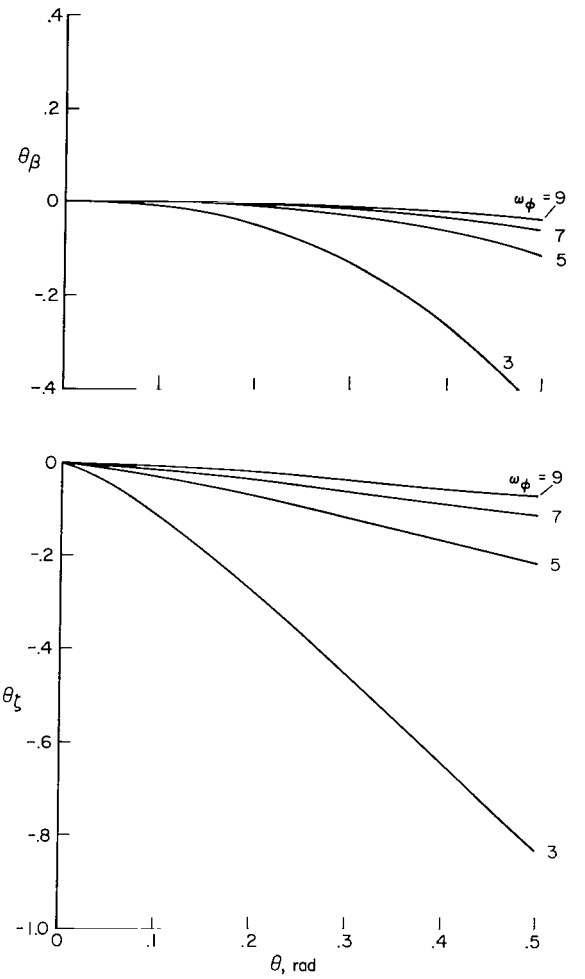

Figure 16.- Equivalent pitch-flap and pitch-lag coupling for a soft inplane rotor blade: $\omega_v = 0.7$, $\mathcal{R} = 1.0$, $\beta_{pc} = 0.0$ rad.

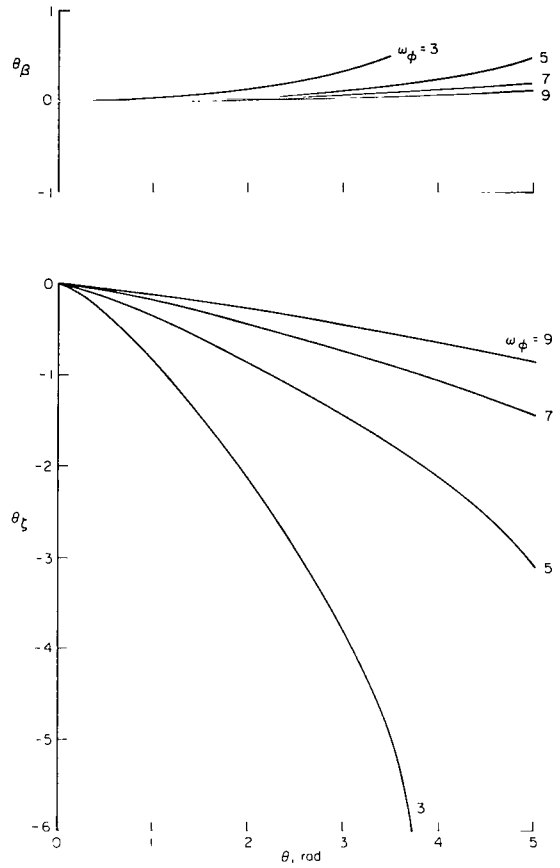

Figure 17.- Equivalent pitch-flap and pitch-lag coupling for a stiff inplane rotor blade: $\omega_v = 1.5$, $\mathcal{R} = 0.0$, $\beta_{pc} = 0.0$ rad.

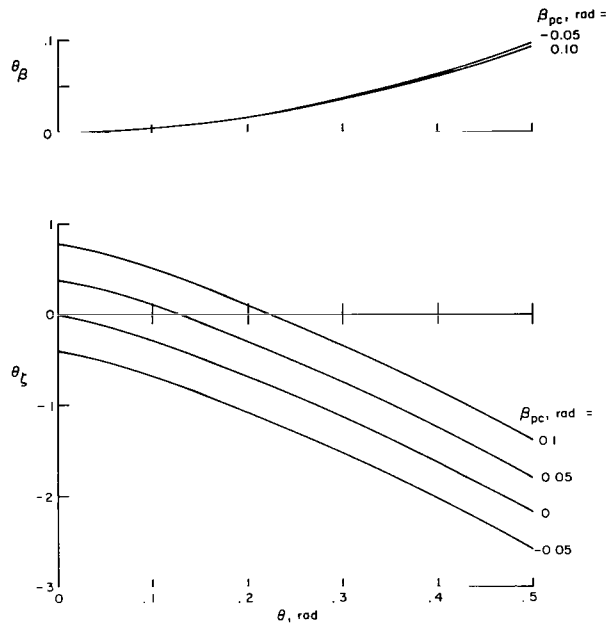

Figure 18.- Equivalent pitch-flap and pitch-lag coupling for a soft inplane rotor blade: $\omega_v = 0.7$, $\omega_\phi = 5.0$, $\mathcal{R} = 0.0$.

General Stability Characteristics, Locus of Roots

A general overview of hingeless rotor blade flap-lag-torsion stability characteristics is next provided by a series of figures showing the locus of roots of each fundamental mode as the blade pitch angle θ is increased from zero to 0.5 rad. The main configuration variables of interest are the torsion frequency, the lead-lag frequency, and the structural coupling parameter $\mathcal{R}$. Before presenting these results, it will be useful to review the flap-lag stability characteristics of a torsionally rigid blade, based on the results of reference 6 extended here to include variations in $\mathcal{R}$ (in ref. 6, $\mathcal{R} = 1$ only) and the second order angle of attack terms. The locus of roots for typical soft and stiff inplane configurations are shown in figure 19.

At zero pitch angle the flap and lead-lag modes are uncoupled. The flap mode is highly damped due to the large aerodynamic damping produced by lift forces associated with flapping velocity. The lead-lag damping, however, is

very small. This is because the aerodynamic drag forces associated with lead-lag velocity are very small. In the present analysis, structural lead-lag damping is not included. According to results of reference 5, structural damping acts like aerodynamic profile drag damping, and for weak flap-lag instabilities, structural damping can eliminate the instability.

As the blade pitch angle increases from zero, the flap and lead-lag modes become coupled and the motion may be destabilized. The flap mode remains stable for both the soft and stiff inplane configurations; the lead-lag mode is stabilized for the soft inplane configuration only, and it may become unstable for the stiff inplane configuration for values of $\Re$ between 0 and 1. The effects of flap-lag structural coupling are larger for the stiff inplane than the soft inplane configurations because this coupling is proportional to $EI_{z'} - EI_{y'}$.

The flap-lag stability characteristics will be altered when torsional flexibility is introduced. The changes are expected to be large when the torsion frequency is low. Figure 20 shows the locus of roots for the soft inplane configuration for three values of $\Re$ and figure 21 shows the corresponding locus of roots for the stiff inplane configuration. As expected, the effects of torsional flexibility are largest when ω_ϕ is low and the stiff inplane configuration shows larger variations in frequency and damping than the soft inplane configuration, again due to the difference in $EI_{z'} - EI_{y'}$. The soft inplane lead-lag mode damping is generally increased by torsional flexibility while the flap mode damping is reduced. There is little influence of torsion frequency on the torsion mode damping. Furthermore, the effects of the structural coupling

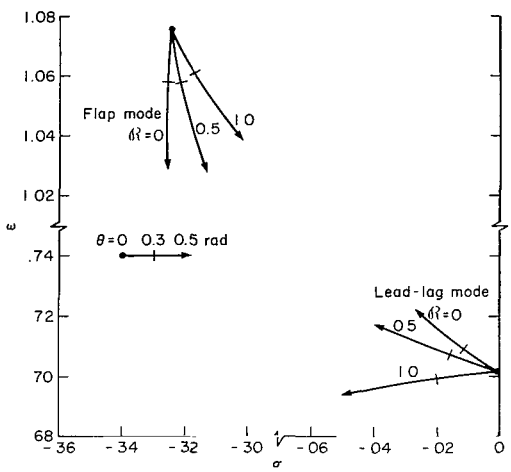

(a) Soft inplane, $\omega_V = 0.7$.

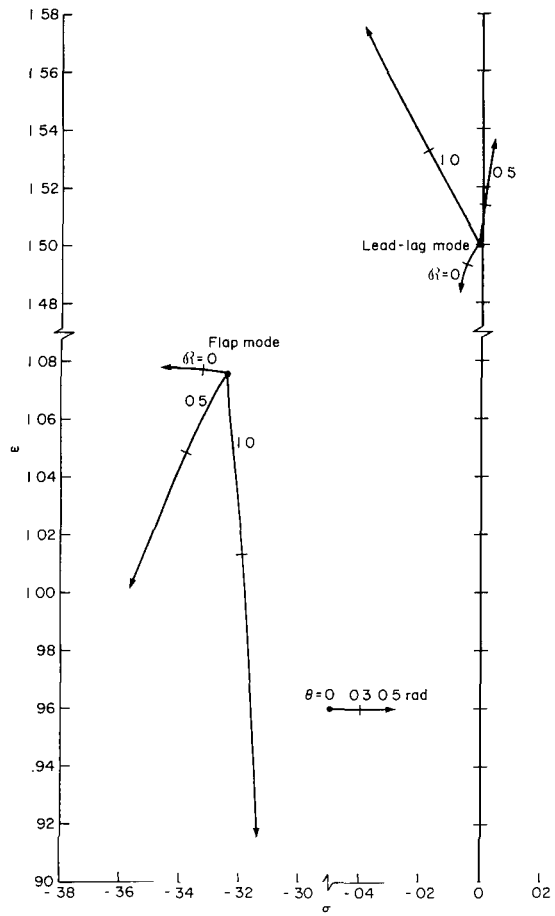

(b) Stiff inplane, $\omega_V = 1.5$.

Figure 19.- Locus of roots for torsionally rigid rotor blade: $\beta_{pc} = 0.0$ rad.

parameter $\mathcal{R}$ are not large for the soft inplane configuration. The increase in lead-lag damping, as torsional flexibility increases, is due to the equivalent kinematic pitch-lag coupling produced by bending-torsion structural coupling.

The stability of the stiff inplane configuration in figure 21 is strongly influenced by torsional flexibility. There is a lead-lag mode instability that depends on both ω_ϕ and $\mathcal{R}$ and a flap mode divergence for small values of $\mathcal{R}$ and ω_ϕ. Depending on the particular values of $\mathcal{R}$ and ω_ϕ, either the flap mode divergence or the lead-lag mode instability will occur at the lowest pitch angle. Again, the effects of torsional flexibility can be attributed mainly to the bending-torsion structural coupling and the associated kinematic pitch-lag coupling. For example, according to the rigid blade flap-lag analysis of reference 5, negative θ_ζ destabilizes the lead-lag mode for small and moderate values of $\mathcal{R}$ and stabilizes it for $\mathcal{R} \cong 1$. For the present results, θ_ζ becomes increasingly negative (fig. 17) as the torsion frequency is decreased

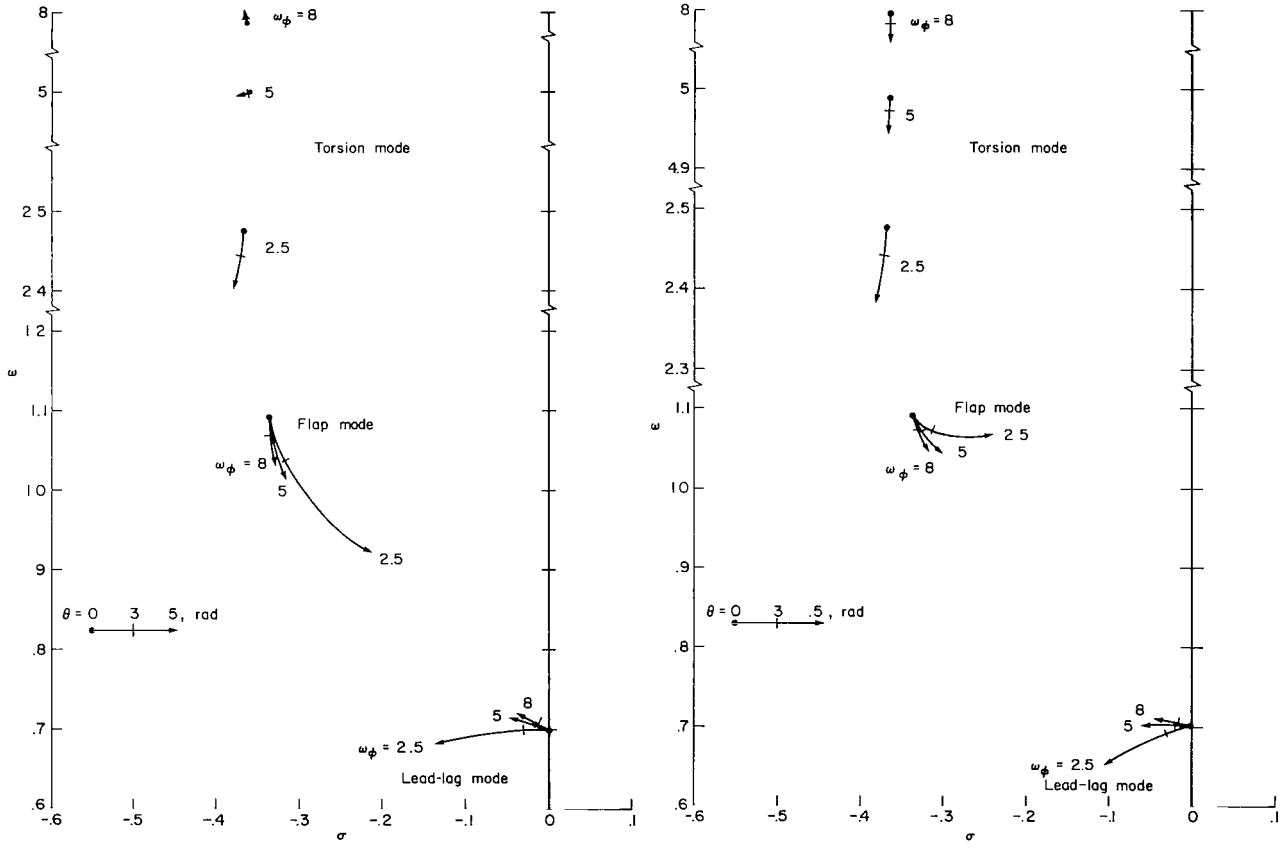

(a) $\mathcal{R}$ = 0.0. (b) $\mathcal{R}$ = 0.5.

Figure 20.- Locus of roots for a soft inplane rotor blade: ω_V = 0.7, β_{pc} = 0.0 rad.

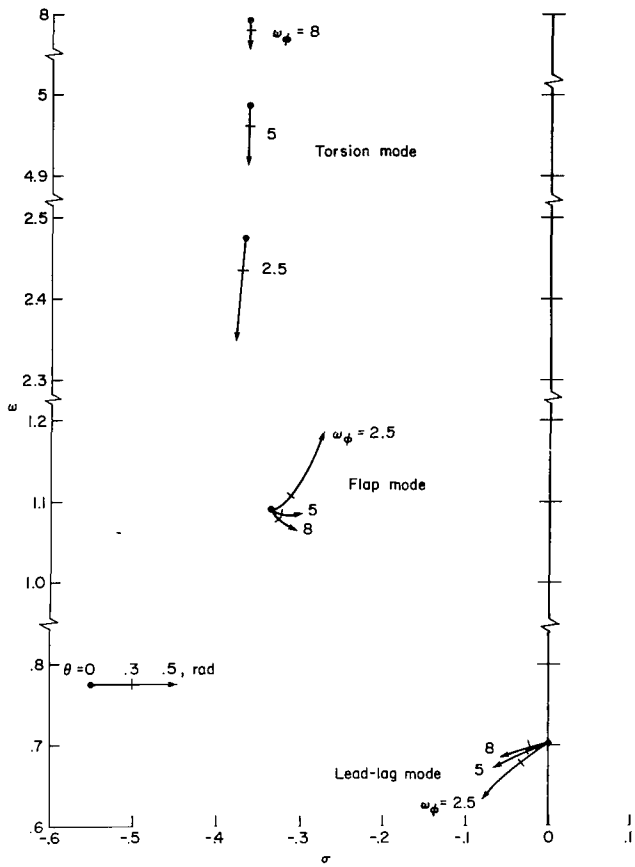

(c) $\mathcal{R} = 1.0$.

Figure 20.- Concluded.

and, analogous to the rigid blade flap-lag results, the lead-lag mode is destabilized when $\mathcal{R} = 0$ and stabilized when $\mathcal{R} = 1.0$. At very low torsion frequencies, $\omega_\phi \leq 2.5$, this analog is not valid since torsional dynamics terms begin to dominate stability.

Effect of Lead-Lag Frequency, Torsion Frequency, and Flap-Lag Structural Coupling on Stability Boundaries

In the next series of results, stability boundaries are presented for a wide range of parameter values with blade pitch angle θ the dependent variable. At low blade pitch angles, the motion is generally stable, but as θ is increased, the blade motion may become less stable. If this trend continues, a stability boundary is crossed at the critical pitch angle θ_{cr} and the motion becomes unstable. In a few cases, the motion is unstable at zero pitch angle and may be stabilized at higher pitch angles. Arrows are provided in the figures to indicate the stable and unstable regions defined by the

stability boundaries and, in some cases, crosshatching is included on the unstable side of the boundary. In most cases, the regions of instability are clear and the crosshatching is omitted to avoid obscuring the figures. In general, an instability of the lead-lag mode is encountered when a stability boundary is crossed. In some cases, however, modes other than the lead-lag mode determine the stability boundary. In such cases an (F) or (T), for flap mode or torsion mode, respectively, is placed next to the stability boundary. The notation "Div" refers to a flap mode divergence.

The first result in figure 22 is for the flap-lag stability boundaries of a torsionally rigid blade as a function of lead-lag frequency and for several values of the structural coupling parameter $\mathcal{R}$. The soft inplane configurations are always stable, while most of the stiff inplane configurations exhibit a lead-lag instability depending on the values of ω_V and $\mathcal{R}$. These pure flap-lag instabilities cannot occur below a certain minimum pitch angle which, in this case, is approximately 0.21 rad. As discussed in reference 5,

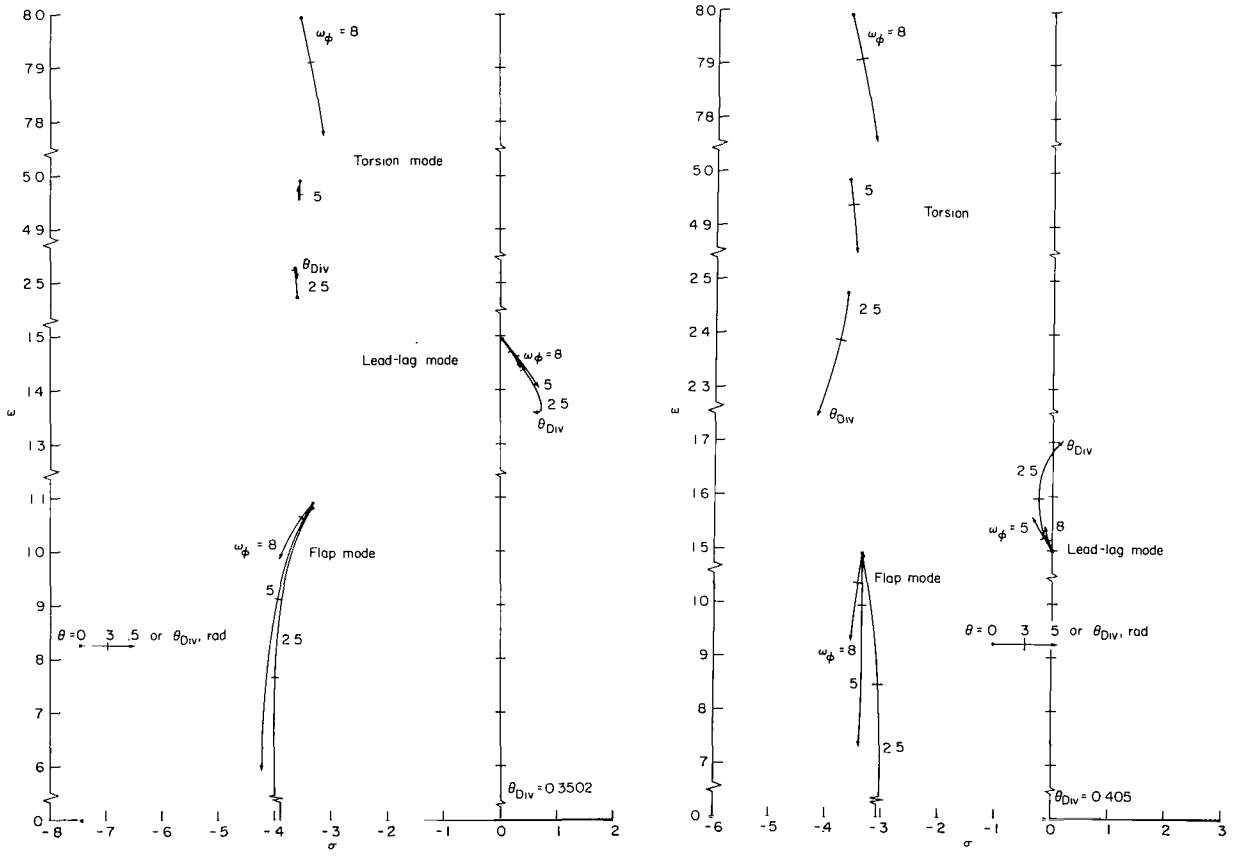

(a) $\mathcal{R}$ = 0.0. (b) $\mathcal{R}$ = 0.5.

Figure 21.- Locus of roots for stiff inplane rotor blade: ω_V = 1.5, β_{pc} = 0.0 rad.

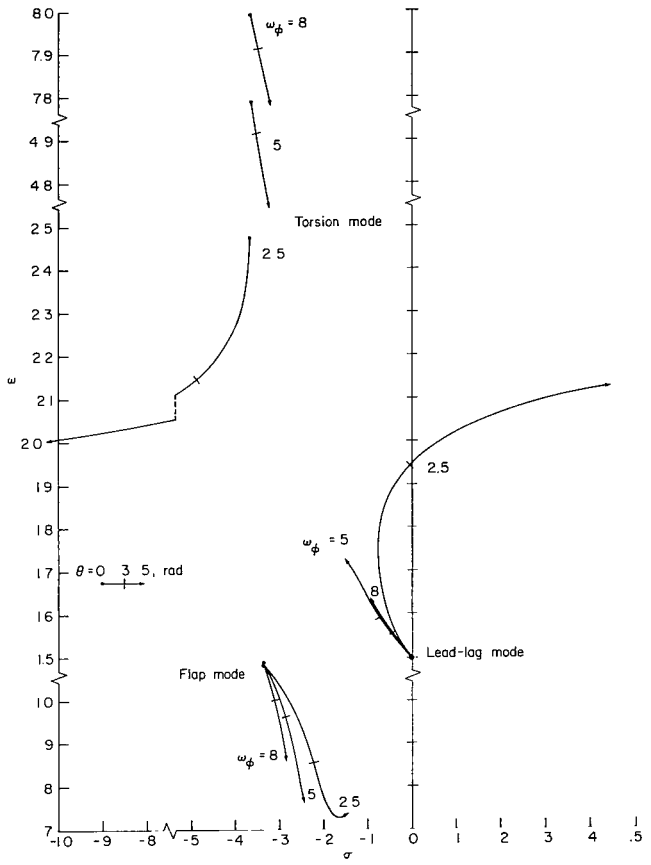

(c) $\mathcal{R} = 1.0$.

Figure 21.- Concluded.

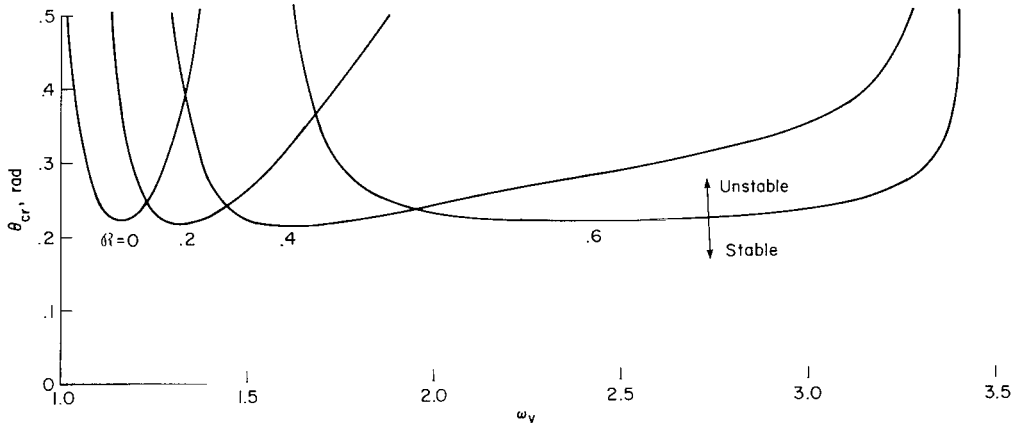

Figure 22.- The effect of $\mathcal{R}$ on the stability boundaries, θ_{cr} versus lead-lag frequency, for a torsionally rigid blade: $\beta_{pc} = 0.0$ rad.

the value of this minimum pitch angle depends on the blade profile drag, rotor solidity, and blade structural damping (not included in these results). The main result to be noted is that as the lead-lag frequency increases, the value of $\mathcal{R}$ must also increase to produce instability at a moderate pitch angle. For $\mathcal{R} \gtrsim 0.6$, flap-lag instability is unlikely for practical lead-lag frequencies ($\omega_v \lesssim 2.0$).

Torsional flexibility greatly modifies the flap-lag stability boundaries as shown in figures 23 to 28. In each figure, for a single value of $\mathcal{R}$, ω_ϕ

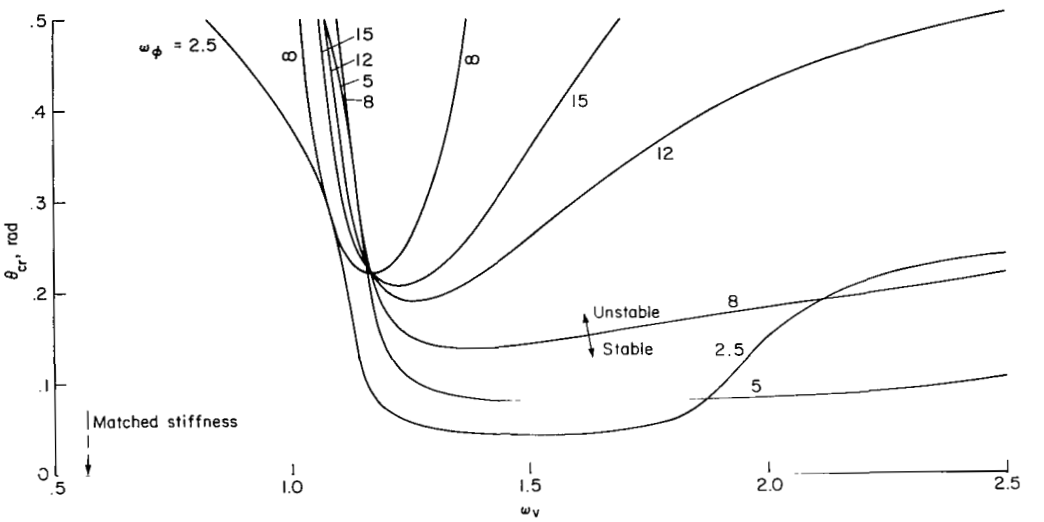

Figure 23.- The effect of torsion frequency on stability boundaries, θ_{cr} versus lead-lag frequency: β_{pc} = 0.0 rad, $\mathcal{R}$ = 0.0.

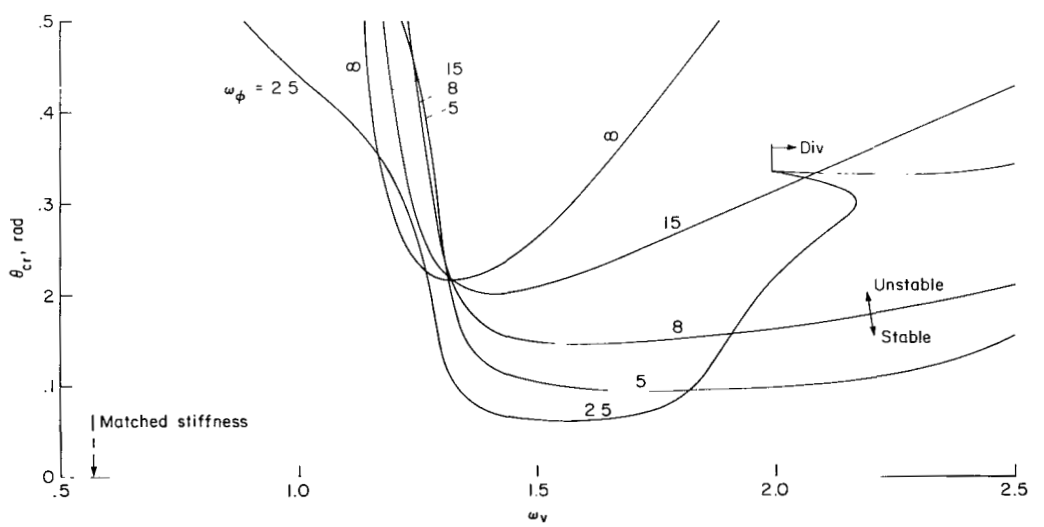

Figure 24.- The effect of torsion frequency on stability boundaries, θ_{cr} versus lead-lag frequency: β_{pc} = 0.0 rad, $\mathcal{R}$ = 0.2.

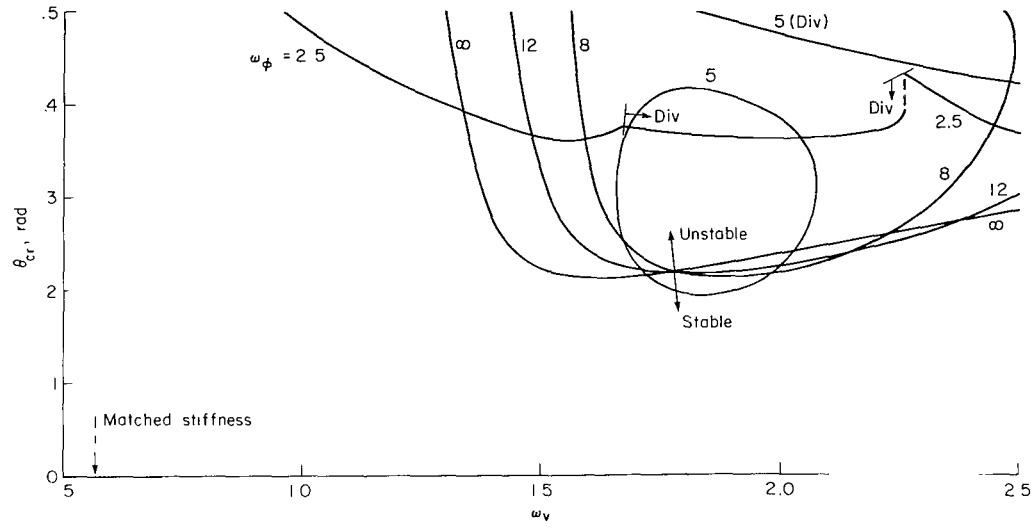

Figure 25.- The effect of torsion frequency on the stability boundaries, θ_{cr} versus lead-lag frequency: β_{pc} = 0.0 rad, $\mathcal{R}$ = 0.4.

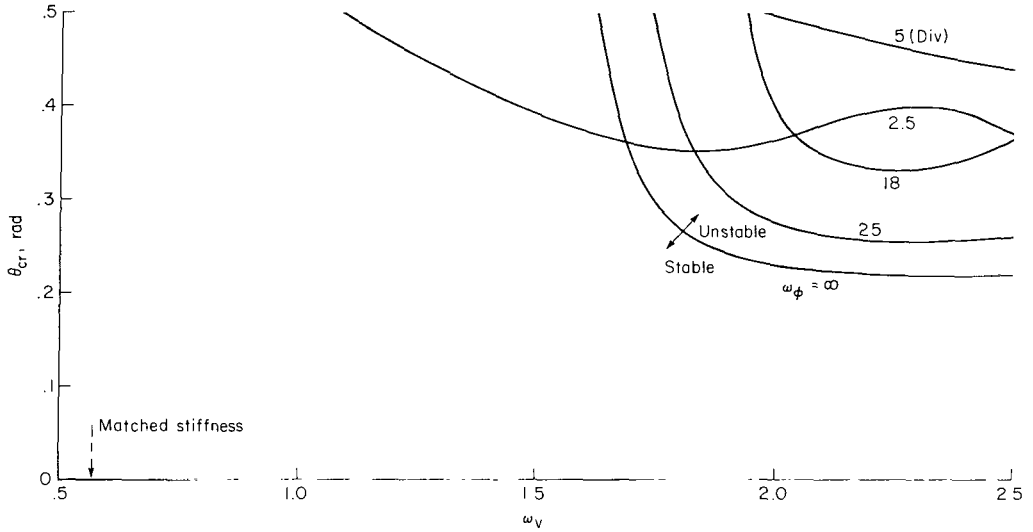

Figure 26.- The effect of torsion frequency on the stability boundaries, θ_{cr} versus lead-lag frequency: β_{pc} = 0.0 rad, $\mathcal{R}$ = 0.6.

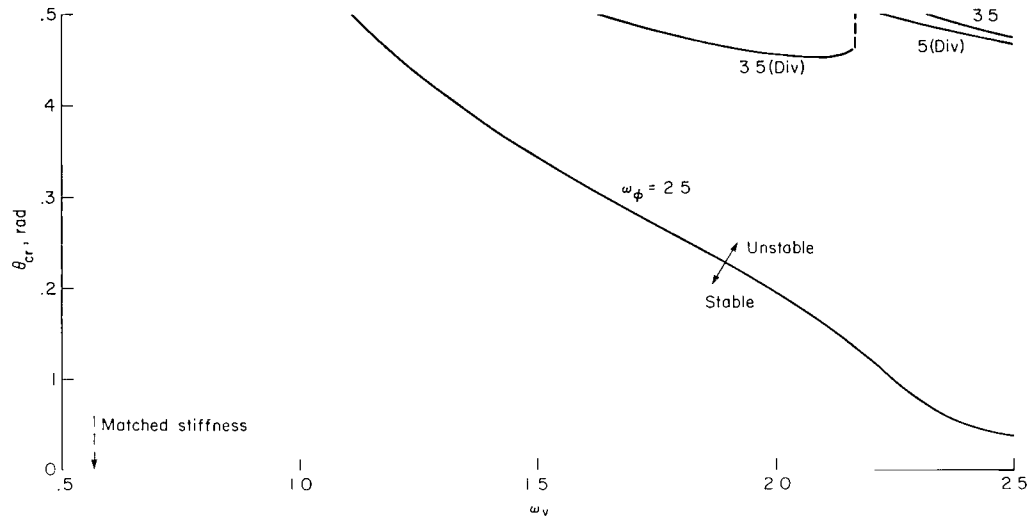

Figure 27.- The effect of torsion frequency on the stability boundaries, θ_{cr} versus lead-lag frequency: β_{pc} = 0.0 rad, $\mathcal{R}$ = 0.8.

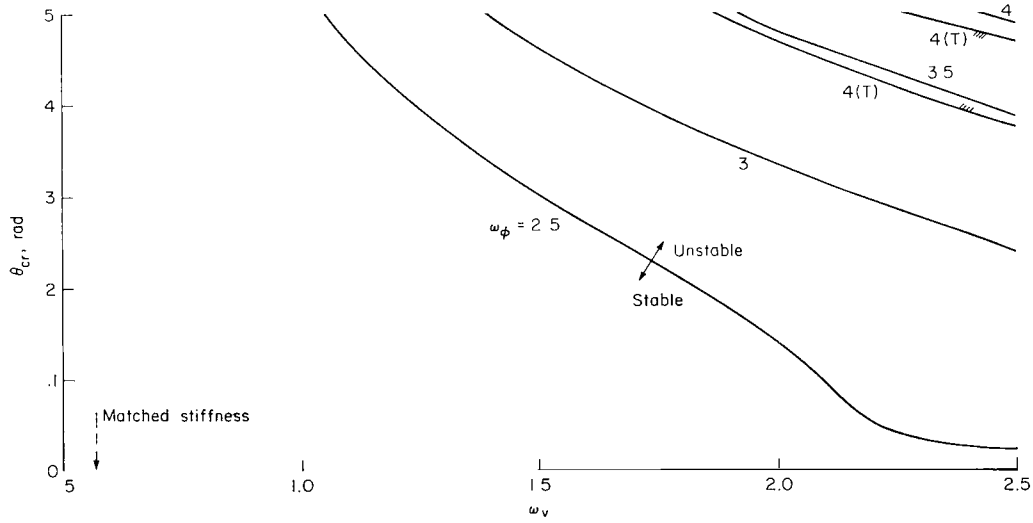

Figure 28.- The effect of torsion frequency on the stability boundaries, θ_{cr} versus lead-lag frequency: β_{pc} = 0.0 rad, $\mathcal{R}$ = 1.0.

is varied from 2.5 to ∞. In general, soft inplane configurations are free of instability for all combinations of $\mathcal{R}$ and ω_ϕ. A special limiting case of the soft inplane configurations is the matched stiffness configuration where $EI_z' = EI_y'$, and all flap-lag and bending-torsion structural coupling vanishes. For this configuration the torsion modes are uncoupled from the bending modes, and the lead-lag damping may be obtained approximately, but with good accuracy, from a flap-lag analysis. Since torsionally rigid soft inplane configurations are virtually always stable, torsionally flexible matched stiffness configurations may be expected to be stable for all values of $\mathcal{R}$ and ω_ϕ. This expectation is confirmed by the results. Figures 23 and 28 show that the stability boundaries shift up and out of the practical pitch angle range as the lead-lag frequency decreases to the matched stiffness frequency marked on the figures.

In contrast to the soft inplane configurations, the stiff inplane configurations again exhibit a variety of unstable behavior. For low values of $\mathcal{R}$, the region of instability occurs at increasingly smaller pitch angles as the torsion frequency is reduced. This is directly attributable to the equivalent pitch-lag coupling of the bending-torsion structural coupling. As $\mathcal{R}$ increases, the region of instability shifts to larger pitch angles and higher lead-lag frequencies. When $\mathcal{R} = 1.0$, the motion is stable for all practical configurations. For very low torsion frequency or high lead-lag frequency, however, a small unstable region is present. This instability appears to be associated with a coincidence of the lead-lag and torsion frequencies $\omega_v \cong \omega_\phi$.

The results of figures 23-28 are cross-plotted for $\omega_\phi = 5$ in figure 29 to show more directly the effect of the structural coupling parameter $\mathcal{R}$. Compared to figure 22 for a torsionally rigid blade, the effect of torsional flexibility is to reduce significantly the pitch angle at which instability occurs.

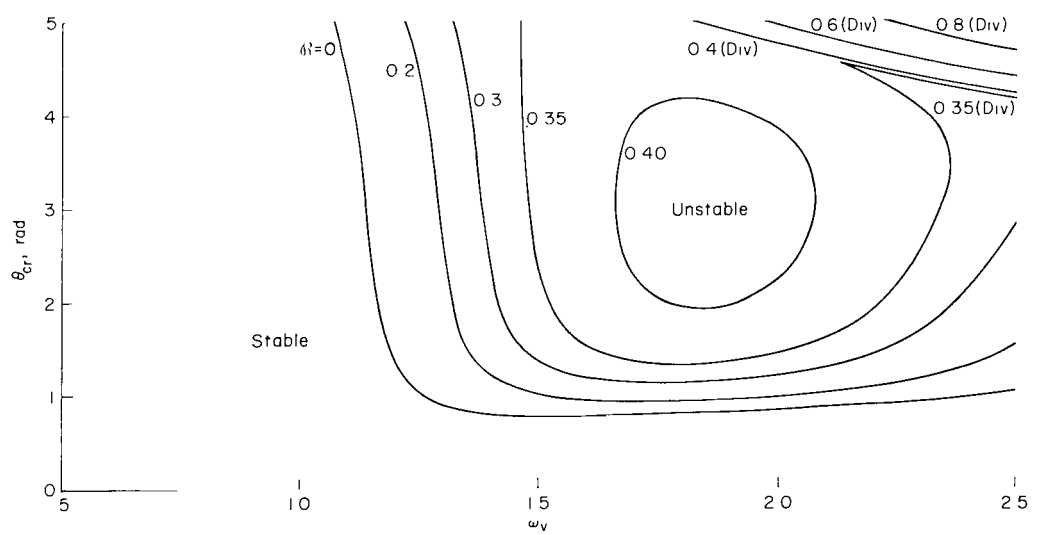

Figure 29.- The effect of $\mathcal{R}$ on the stability boundaries, θ_{cr} versus lead-lag frequency: $\omega_\phi = 5.0$, $\beta_{pc} = 0.0$.

In summary, these results without precone indicate that typical hingeless rotor blade configurations ($\omega_\phi \gtrsim 5$, $\omega_v \lesssim 2$) operating at moderate pitch angles ($\theta \leq 0.3$ rad) are stable, except when the structural coupling parameter $\mathcal{R}$ is relatively small.

Effect of Precone on Stability Boundaries

The influence of precone on the stability of torsionally rigid rotor blades is relatively small (refs. 5 and 6), but for torsionally flexible blades its influence can be very large. This is due primarily to the bending-torsion structural coupling terms in the torsion equation. As noted above, the equivalent pitch-lag coupling produced by structural coupling is a function of the equilibrium flap and lead-lag deflections of the blade that are in turn strongly dependent on precone. As clearly shown in figures 14 and 18, positive precone produces a positive equivalent pitch-lag coupling, at small pitch angles, that can be strongly destabilizing. The stability boundaries without precone, given in figures 23-28, are repeated for three values of $\mathcal{R}$ in figures 30-32 with 0.05 rad precone. A comparison between the two series of figures clearly reveals the destabilizing effects of precone. For low and moderate torsion frequencies, a new region of instability appears which begins at or near zero pitch angle and terminates at a small positive pitch angle. The range of pitch angles for which the blade is unstable increases as ω_ϕ decreases because the pitch-lag coupling increases with decreasing ω_ϕ. For $\mathcal{R} = 0.0$ this precone instability is limited to soft inplane configurations; however, as $\mathcal{R}$ increases, the region of instability expands to include stiff inplane configurations as well. At the low ω_v range, near the matched stiffness configuration, the unstable region closes because the structural coupling ($EI_{z'} - EI_{y'}$) available to generate destabilizing pitch-lag coupling decreases and then vanishes when $EI_{z'} = EI_{y'}$.

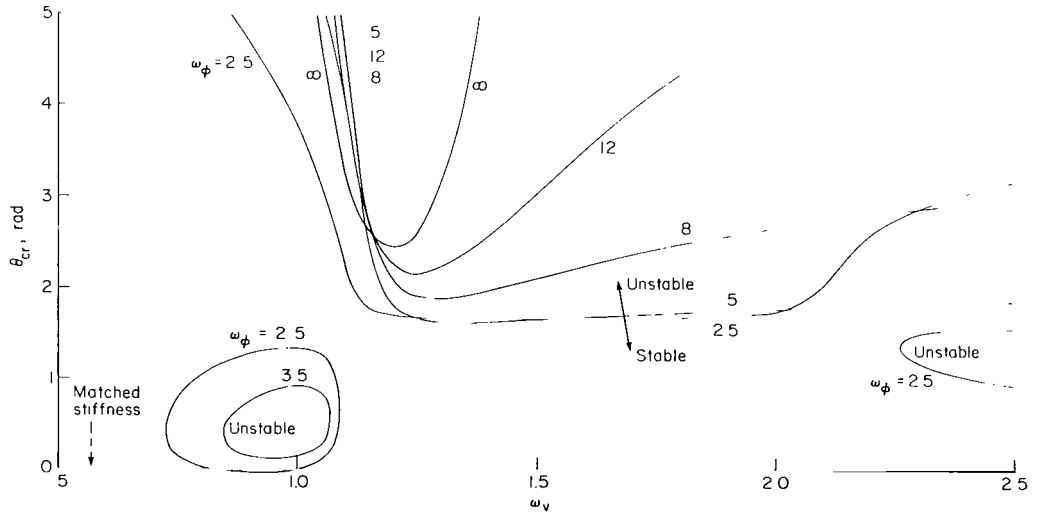

Figure 30.- The effect of precone and torsion frequency on the stability boundaries, θ_{cr} versus lead-lag frequency: $\beta_{pc} = 0.05$ rad, $\mathcal{R} = 0.0$.

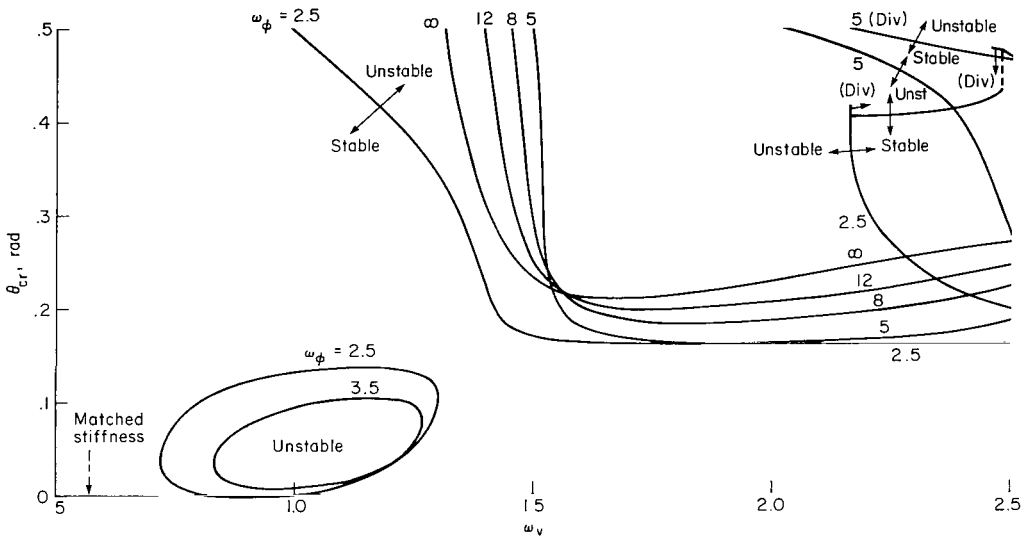

Figure 31.- The effect of precone and torsion frequency on the stability boundaries, θ_{cr} versus lead-lag frequency: β_{pc} = 0.05 rad, $\mathcal{R}$ = 0.4.

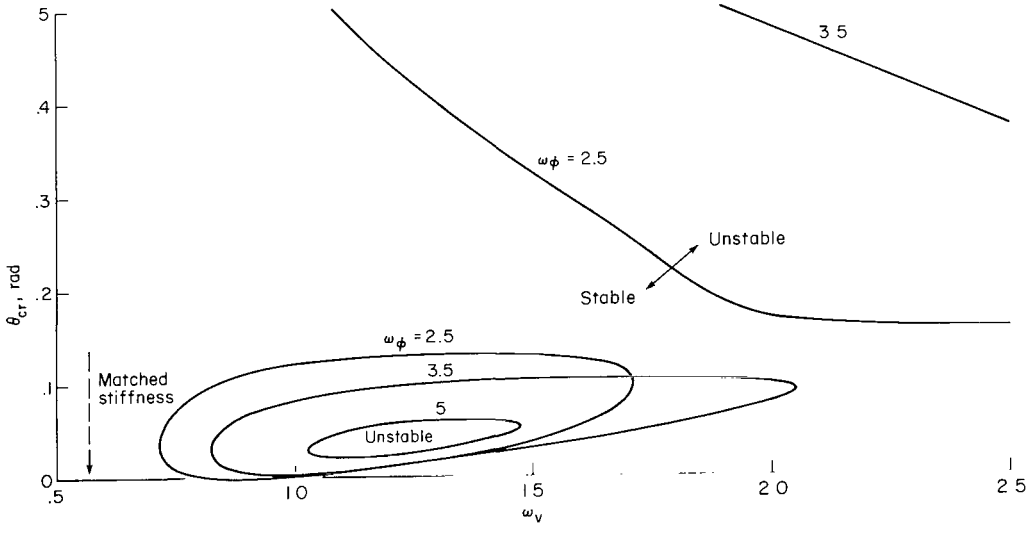

Figure 32.- The effect of precone and torsion frequency on the stability boundaries, θ_{cr} versus lead-lag frequency: β_{pc} = 0.05 rad, $\mathcal{R}$ = 1.0.

In addition to the new region of instability at low pitch angles, precone also influences the previous stability boundaries at higher pitch angles, but the effect is not very large. Generally, these stability boundaries are shifted to higher pitch angles. The effect of increasing precone to 0.1 rad for $\mathcal{R} = 1$ is shown in figure 33; if the results of figures 33 and 32 are compared, it will be noted that the regions of instability at low pitch angles more than double in size when the precone is doubled.

Additional results are given for soft and stiff inplane configurations where precone is taken to be the independent variable. For the soft inplane configuration with $\omega_v = 0.7$ (fig. 34) the motion is stable for $\omega_\phi \geq 5.0$, and only the result for $\omega_\phi = 2.5$ is shown. The effect of variations in $\mathcal{R}$ is

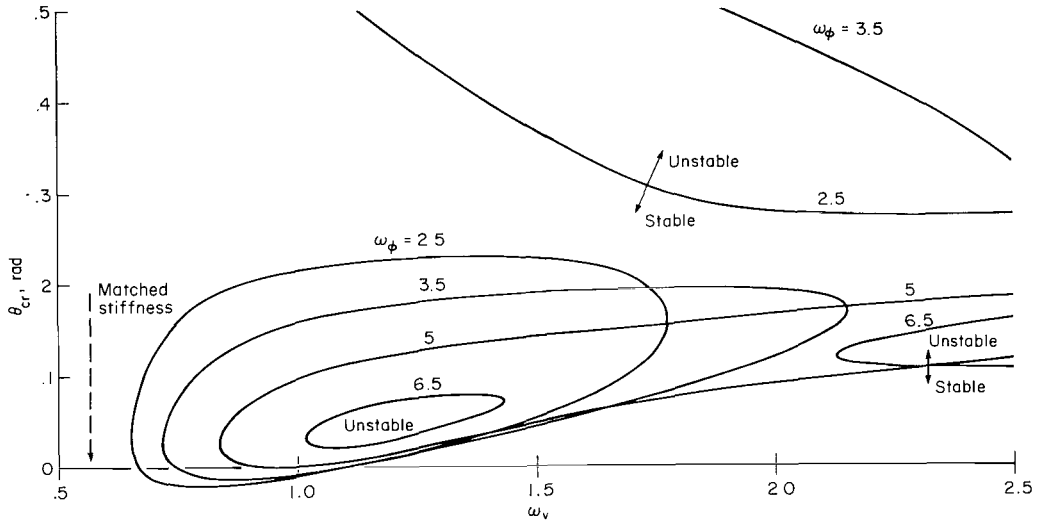

Figure 33.- The effect of precone and torsion frequency on the stability boundaries, θ_{cr} versus lead-lag frequency: $\beta_{pc} = 0.1$ rad, $\mathcal{R} = 1.0$.

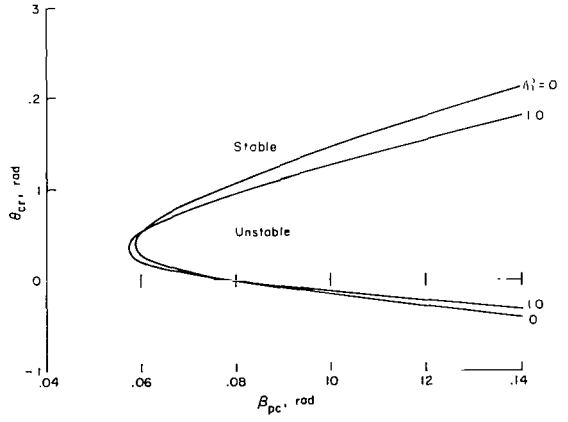

Figure 34.- The effect of $\mathcal{R}$ on the stability boundaries, θ_{cr} versus precone angle: $\omega_\phi = 2.5$, $\omega_v = 0.7$.

seen to be quite small. For the stiff inplane configuration in figures 35-38, the motion is unstable for a wide range of precone, torsion frequency, and $\mathcal{R}$. For simplicity, only values for ω_ϕ = 2.5, 5.0, 12.0 and ∞ are shown. At lower values of ω_ϕ, the results show large variations with respect to β_{pc} and $\mathcal{R}$, while at high ω_ϕ, the variations are small. As noted above, the instabilities are primarily generated by the equivalent pitch-lag coupling produced by bending-torsion structural coupling. This coupling varies roughly in proportion to precone and inversely in proportion to torsion frequency.

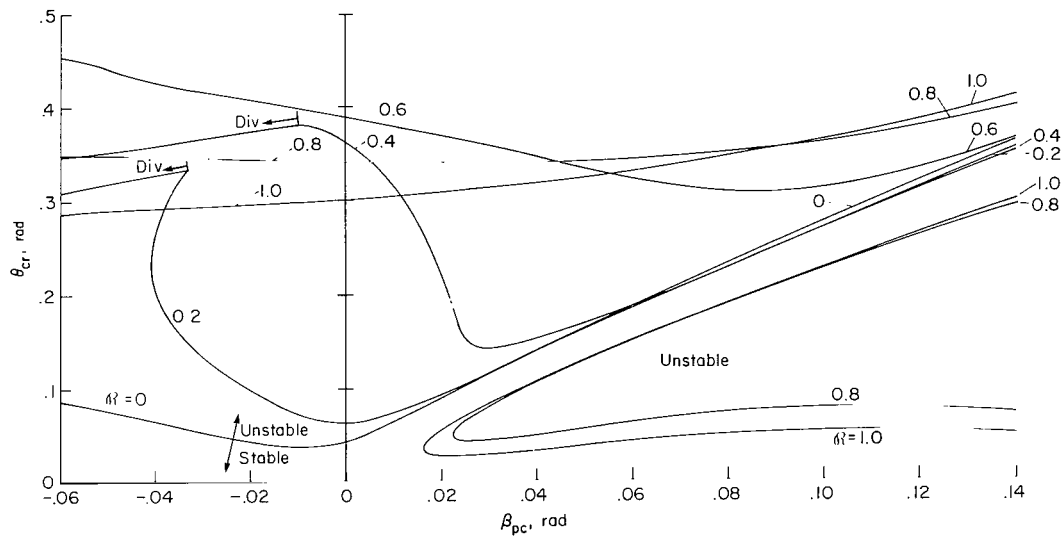

Figure 35.- The effect of $\mathcal{R}$ on the stability boundaries, θ_{cr} versus precone angle: ω_ϕ = 2.5, ω_v = 1.5.

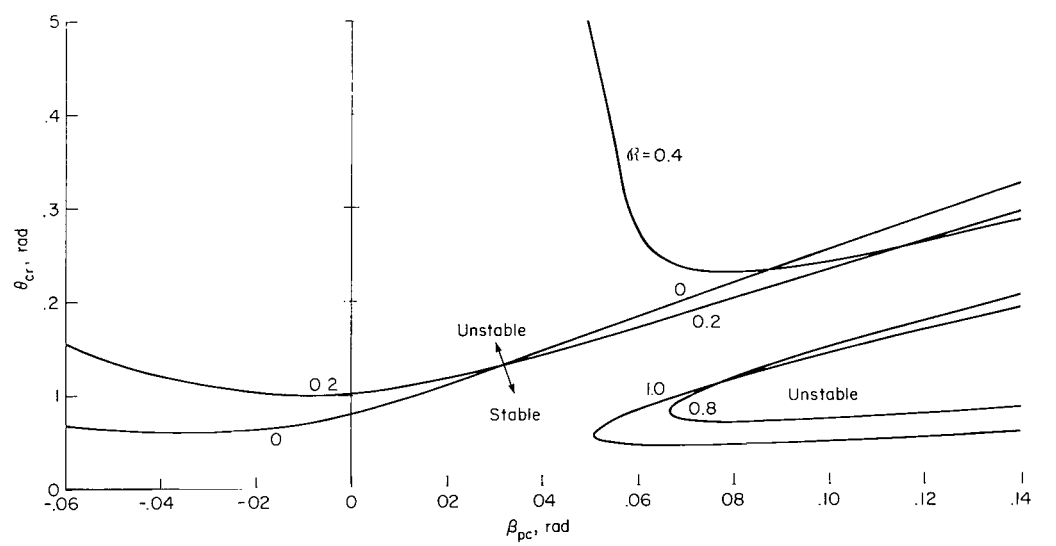

Figure 36.- The effect of $\mathcal{R}$ on the stability boundaries, θ_{cr} versus precone angle: ω_ϕ = 5.0, ω_v = 1.5.

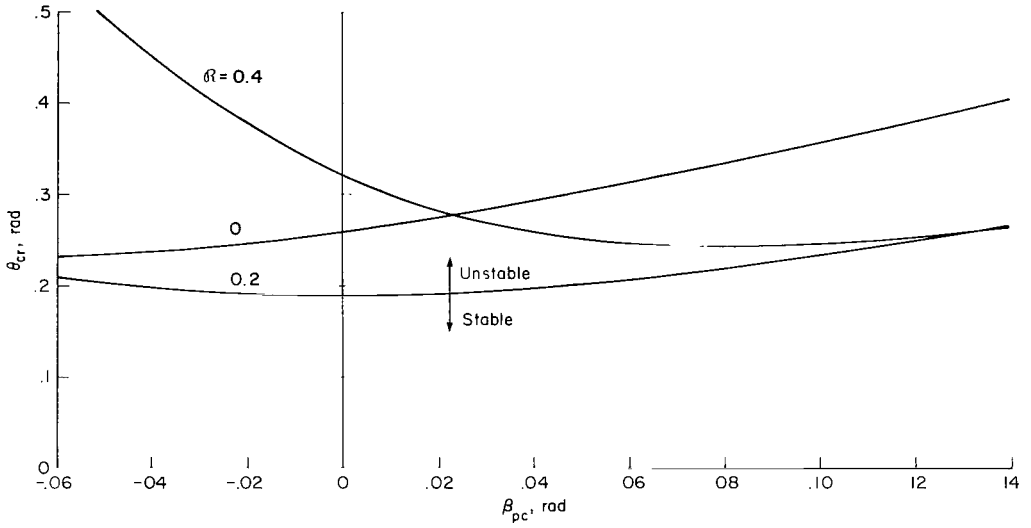

Figure 37.- The effect of $\Re$ on the stability boundaries, θ_{cr} versus precone angle: $\omega_\phi = 12.0$, $\omega_v = 1.5$.

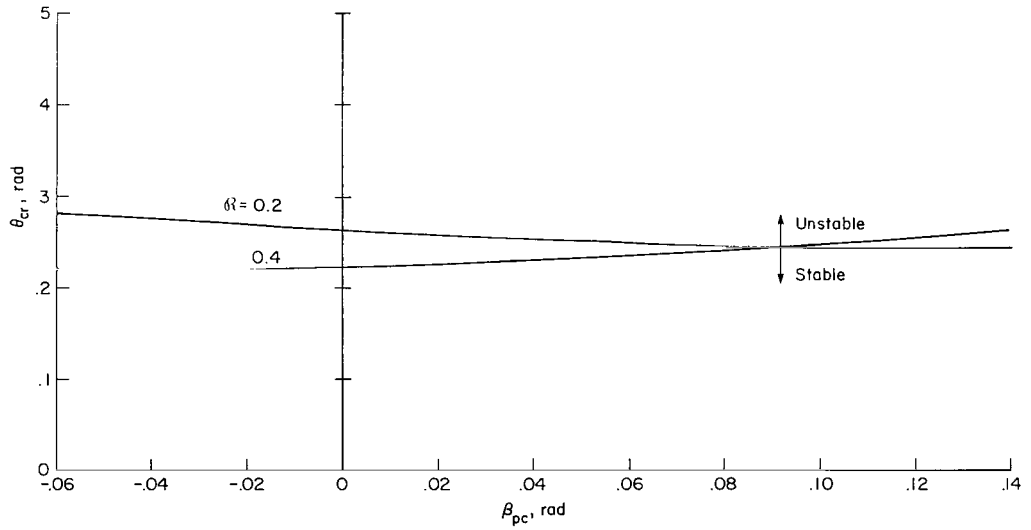

Figure 38.- The effect of $\Re$ on the stability boundaries, θ_{cr} versus precone angle for a torsionally rigid blade: $\omega_v = 1.5$.

Therefore, the stability boundary variation with precone for a large torsion frequency should be reflected in a similar stability boundary variation over a smaller range of precone when the torsion frequency is small. This expectation is reasonably well confirmed by the results, particularly for the lower values of $\mathcal{R}$. Also the small effect of precone for large ω_ϕ is what would be expected from the equivalent pitch-lag coupling effect.

Effect of Torsion Frequency

The results discussed above have clearly shown the important influence of torsion flexibility. We will now consider this influence more directly by showing the variation of stability boundaries as an explicit function of the independent variable ω_ϕ. These results are shown in figures 39-41 for three values of the structural coupling parameter $\mathcal{R}$ and several values of lead-lag frequency. For low ω_ϕ, an increase in torsion frequency is stabilizing for all values of $\mathcal{R}$ and ω_v; at higher torsion frequencies, this relationship is reversed for some configurations. This occurs, for example, when $\mathcal{R} = 0.0$ near $\omega_v \cong \omega_w$ and at moderate $\mathcal{R}$ for certain stiff inplane configurations. The flap divergence boundaries for low torsion frequencies described earlier are shown in detail in the expanded scale portion of figure 40. In general, it is difficult to classify the stability characteristics of torsionally flexible cantilever blades with respect to the effect of increased or decreased torsional flexibility. At large values of ω_ϕ the stability boundaries asymptotically approach the corresponding flap-lag stability boundaries (provided that a flap-lag stability boundary exists). It may be noted in figure 41 that without precone, lead-lag instabilities are not present at typical torsion frequencies ($\omega_\phi \tilde{>} 5$). Since there are no flap-lag instabilities for $\mathcal{R} = 1$ and $\beta_{pc} = 0.0$, the results of figure 41 are consistent with the results discussed above.

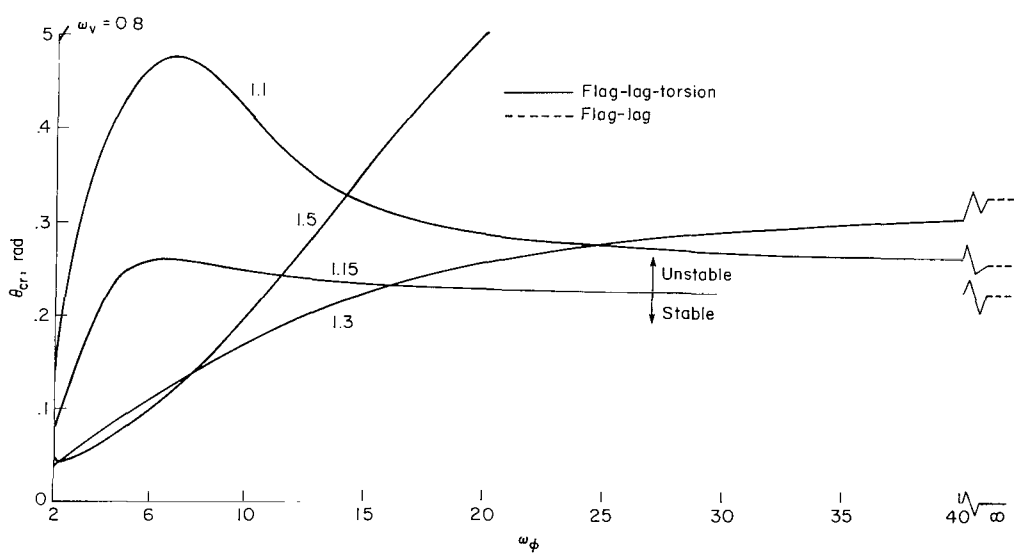

Figure 39.- The effect of lead-lag frequency on the stability boundaries, θ_{cr} versus torsion frequency: $\beta_{pc} = 0.0$ rad, $\mathcal{R} = 0.0$.

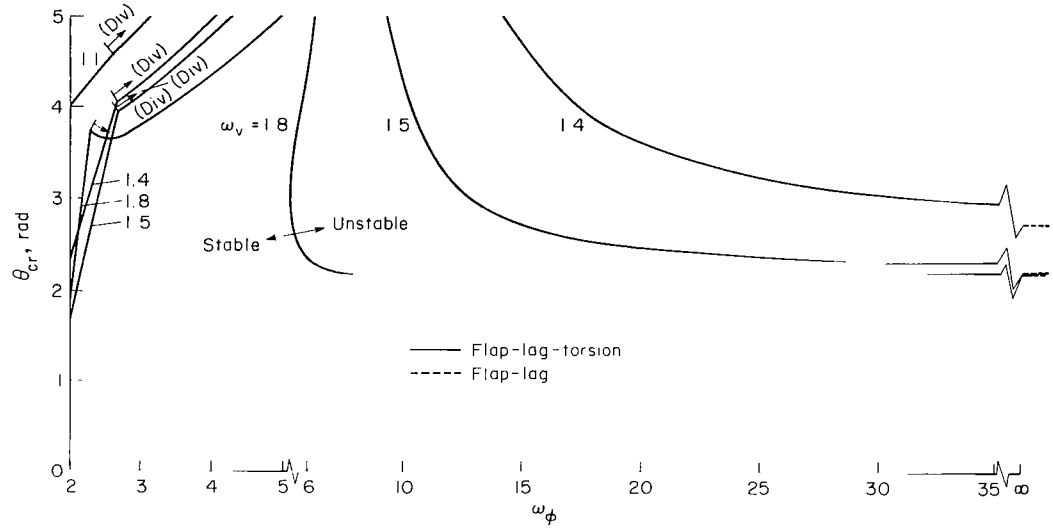

Figure 40.- The effect of lead-lag frequency on the stability boundaries, θ_{cr} versus torsion frequency: β_{pc} = 0.0 rad, $\mathcal{R}$ = 0.4.

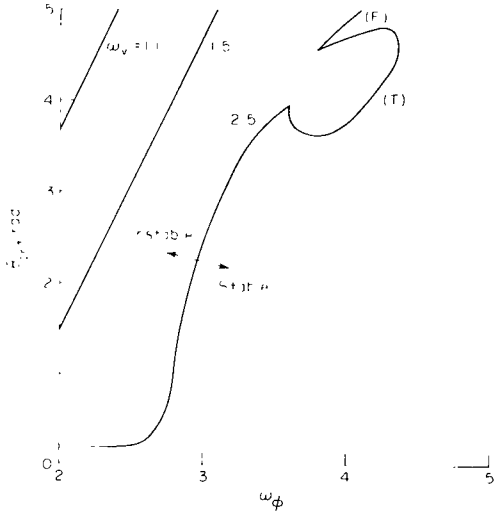

Figure 41.- The effect of lead-lag frequency on the stability boundaries, θ_{cr} versus torsion frequency: β_{pc} = 0.0 rad, $\mathcal{R}$ = 1.0.

A few results are also included to show the effect of torsional flexibility on lead-lag damping of cantilever rotor blades. This is of interest because the lead-lag damping of cantilever blades is inherently low and may lead to problems, such as high blade bending loads or coupled rotor-body instabilities, even if the motion of an isolated blade is stable. Figures 42-44 show several examples where the damping of stable configurations is significantly increased or decreased by torsion flexibility. The damping is given by the dimensionless real part of the lead-lag mode eigenvalue at a pitch angle of 0.3 rad plotted as a function of ω_v for several torsion frequencies. The influence of torsional flexibility is especially clear in these results. As ω_ϕ is reduced, the influence of torsional flexibility is magnified whether the lead-lag damping is increased or decreased. This again is due to the influence of bending-torsion structural coupling. It is also clear that torsional flexibility reverses its influence when ω_v equals the matched stiffness value. At this point, the equivalent pitch-lag coupling changes sign. In general, for

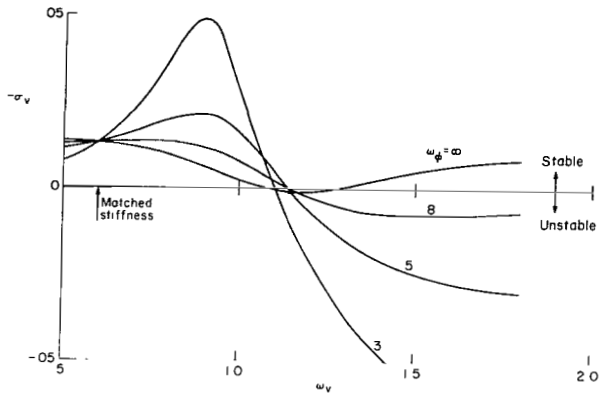

Figure 42.- The effect of torsion frequency on lead-lag modal damping versus lead-lag frequency: β_{pc} = 0.0 rad, θ = 0.3 rad, $\mathcal{R}$ = 0.0.

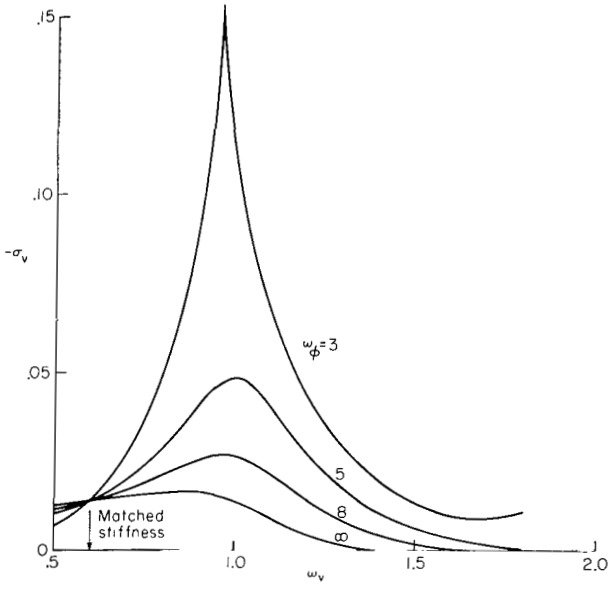

Figure 43.- The effect of torsion frequency on lead-lag modal damping versus lead-lag frequency: β_{pc} = 0.0 rad, θ = 0.3 rad, $\mathcal{R}$ = 0.4.

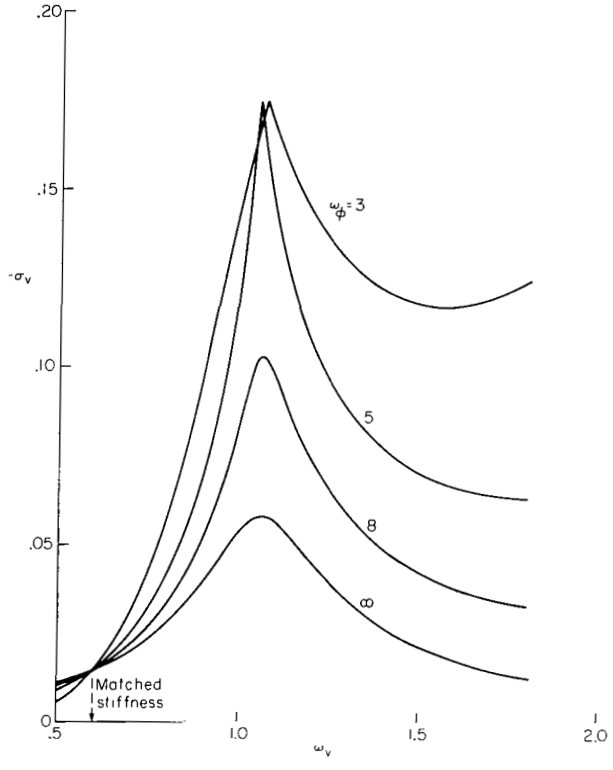

Figure 44.- The effect of torsion frequency on lead-lag modal damping versus lead-lag frequency: β_{pc} = 0.0 rad, θ = 0.3 rad, $\mathcal{R}$ = 1.0.

typical soft and stiff inplane configurations without precone, torsional flexibility increases lead-lag damping except for stiff inplane configurations of low $\mathcal{R}$ values.

Effect of Approximations in the Analysis

The preceding results and discussion have demonstrated the importance of the structural bending-torsion terms in the equations of motion. It is natural to inquire, therefore, if the equations of motion could be simplified, without significant loss of accuracy, by eliminating most of the terms in the torsion equation except the structural terms. This procedure was described in a previous section and results in a system of modified flap-lag equations without independent torsion degrees of freedom.

The results using the modified flap-lag equations are compared to the complete flap-lag-torsion results in figures 45-48. In general, the complete flap-lag torsion equations are required for very low torsion frequencies when inertial, aerodynamic, and structural terms are all important in the torsion equation. At intermediate torsion frequencies, only the structural torsion terms are required and the modified flap-lag equations are appropriate. At very high torsion frequencies, torsion deflections become negligible and a pure flap-lag analysis is adequate.

An indication of the range of torsion frequency where the three levels of complexity are appropriate may be obtained from typical results for a configuration without precone or flap-lag structural coupling ($\mathcal{R} = 0$) in figure 45. For $\omega_\phi \gtrsim 20$, the flap-lag equations without torsion are adequate; for $5 \lesssim \omega_\phi \lesssim 20$, the modified flap-lag equations including structural torsion

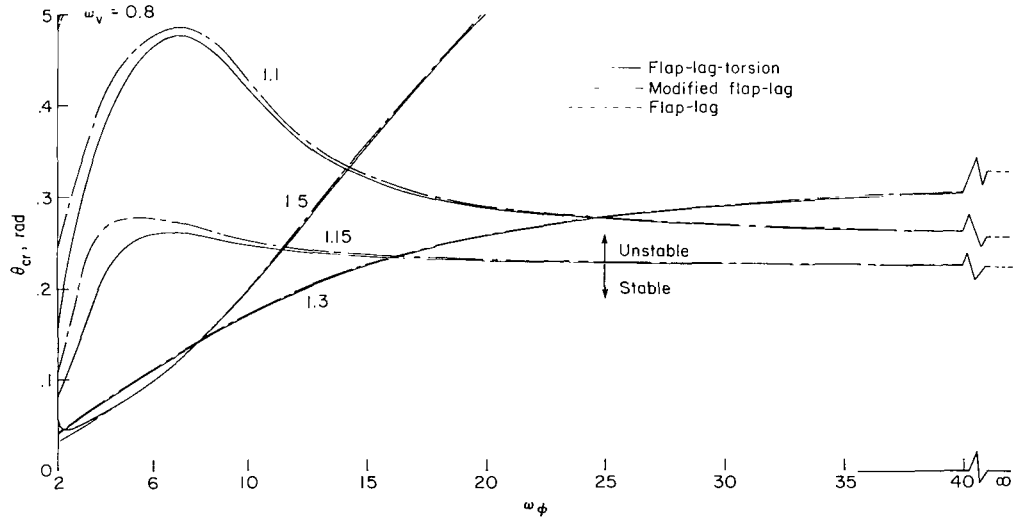

Figure 45.- The effects of approximations in the analysis on the stability boundaries, θ_{cr} versus torsion frequency: $\beta_{pc} = 0.0$ rad, $\mathcal{R} = 0.0$.

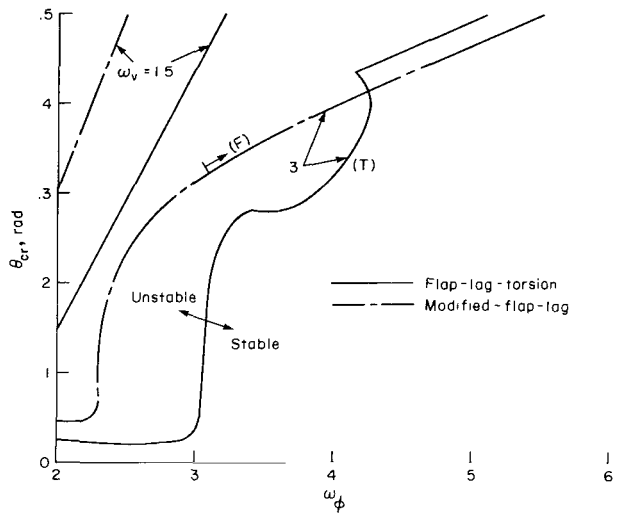

Figure 46.- The effect of approximations in the analysis on the stability boundaries, θ_{cr} versus torsion frequency: $\beta_{pc} = 0.0$ rad, $\mathcal{R} = 1.0$.

terms are sufficient, and for $\omega_\phi \tilde{<} 5$, the full flap-lag-torsion equations are required, including torsion dynamics. Figure 45 clearly shows, however, that this division of the torsion frequency range depends on other parameters as well. For example, with $\omega_v = 1.5$, the effects of torsion deflections due to bending-torsion structural coupling are significant for $\omega_\phi \tilde{>} 20$.

Typical results for a configuration having flap-lag structural coupling ($\mathcal{R} = 1.0$, fig. 46) are generally consistent with the observations based on figure 45. That is, for low torsion frequencies $\omega_\phi \tilde{<} 5$, the complete equations are necessary, and for higher torsion frequencies the modified flap-lag equations are adequate.

Figure 47 shows the variation in modal damping versus ω_ϕ for a stable configuration for the three systems of equations. These results are again consistent with the range of validity outlined above for the approximate equations.

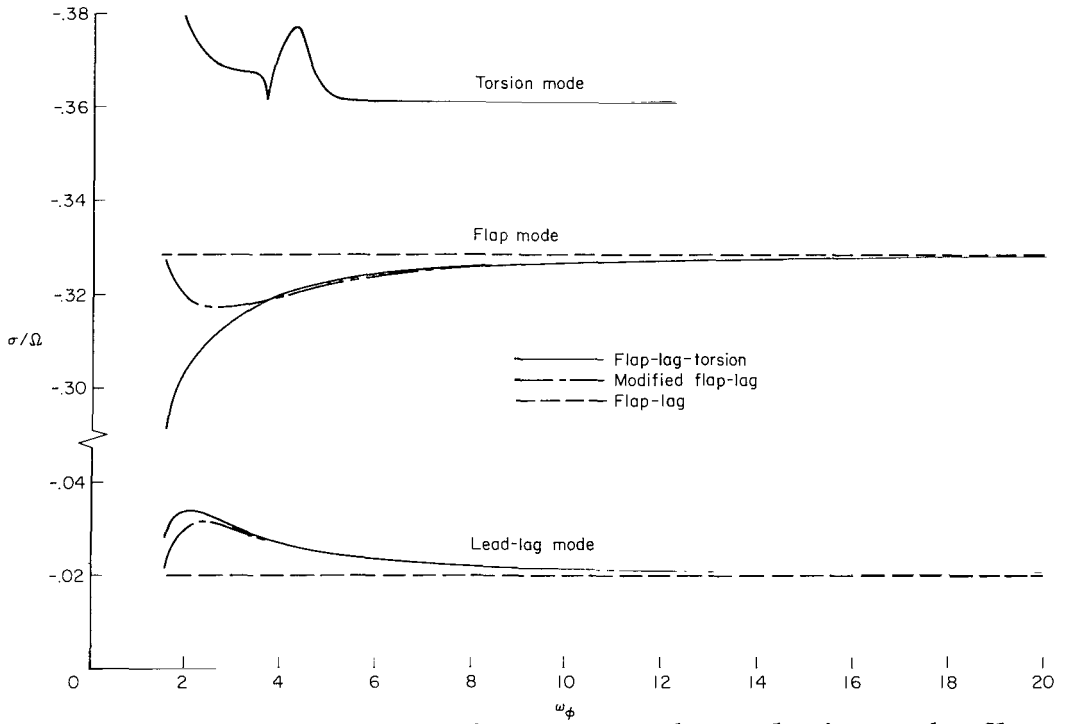

Figure 47.- The effect of approximations in the analysis on the flap, lead-lag, and torsion modal damping versus torsion frequency: $\omega_v = 0.7$, $\beta_{pc} = 0.0$ rad, $\theta = 0.3$ rad, $\mathcal{R} = 1.0$.

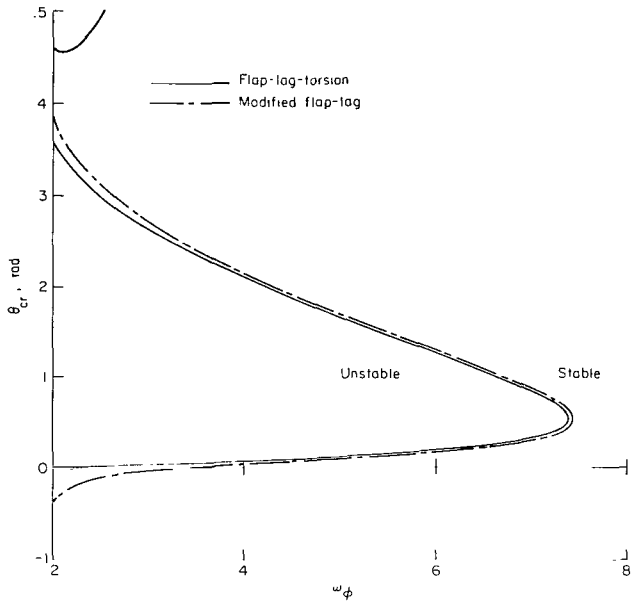

Figure 48.- The effect of approximations in the analysis on the stability boundaries, θ_{cr} versus torsion frequency: $\beta_{pc} = 0.14$ rad, $\omega_v = 1.2$, $\mathcal{R} = 1.0$.

Figure 48 illustrates an example with precone where the modified flap-lag equations are accurate to very low ω_ϕ for predicting the low pitch angle precone instability. A high pitch angle instability at very low ω_ϕ is not predicted by the approximate equations, however, because of the lack of torsion dynamics.

Effect of the Number and Type of Mode Shapes on Accuracy and Convergence

The type and number of mode shapes used in the solution of the equations has been described previously. It is of interest to examine the influence of these factors on the accuracy and especially on the rate of convergence of the results. A previous investigation, using uncoupled mode shapes of a nonrotating cantilever beam for flap-lag stability analysis (ref. 6), indicated that results would be accurate with as few as one or two modes. The present results for the flap-lag-torsion equations are not as simple. Figures 49 and 50 show stability boundaries as a function of precone for a soft and stiff inplane configuration, respectively. In each case, the stability boundaries are shown for an increasing number of mode shapes for two different calculations, the first using uncoupled mode shapes of a nonrotating beam, and the second using coupled mode shapes from a free vibration analysis of the rotor blade about its equilibrium operating condition (see discussion above in the section on Solution of the Equations of Motion).

The results using uncoupled mode shapes of a nonrotating beam are given in figure 49. These mode shapes yield poor convergence of the stability boundaries, and for accurate results five (N) mode shapes are required for

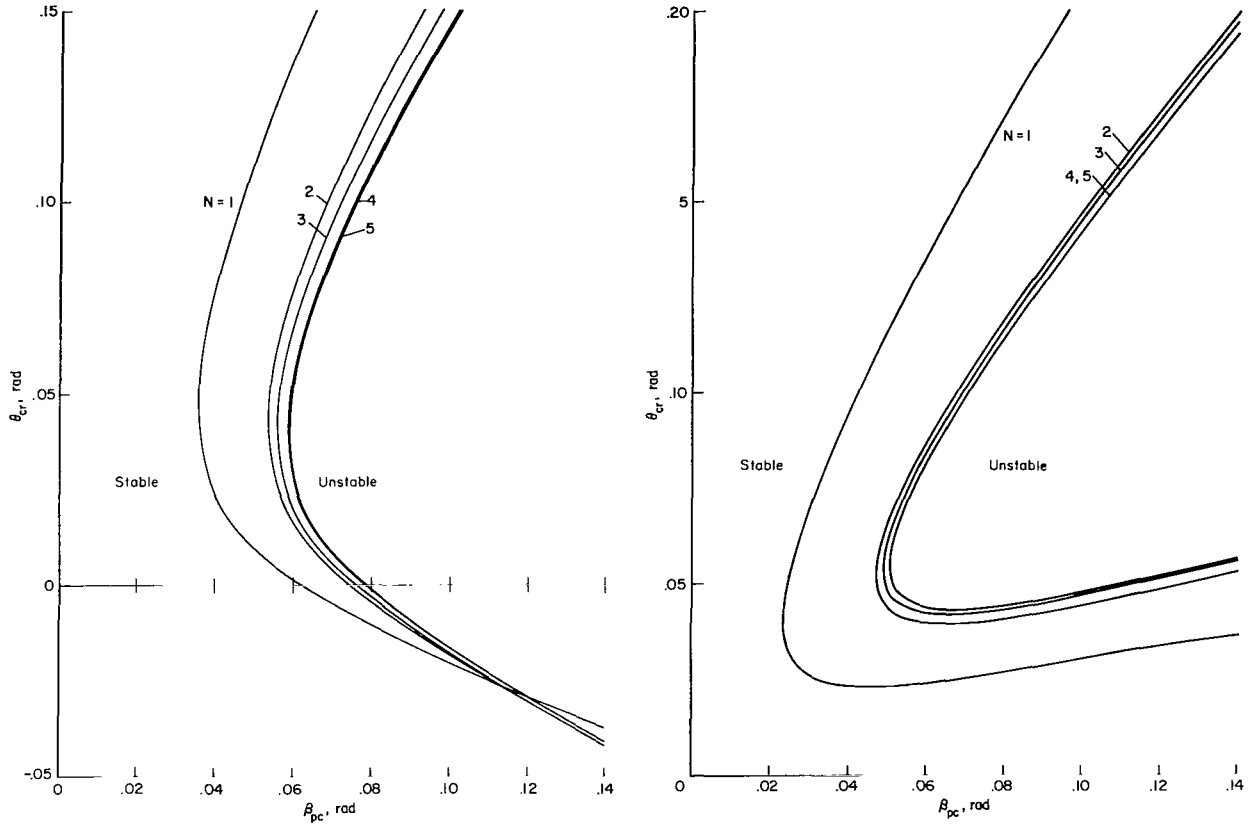

(a) Soft inplane blade: $\omega_v = 0.7$, $\omega_\phi = 2.5$, $\mathcal{R} = 0.0$.

(b) Stiff inplane blade: $\omega_v = 1.5$, $\omega_\phi = 5.0$, $\mathcal{R} = 1.0$.

Figure 49.- Convergence of stability boundaries with respect to number of mode shapes for analysis using uncoupled nonrotating mode shapes; total number of mode shapes and degrees of freedom equals 3N.

each bending and torsion deflection. This yields a total of 15 (3N) degrees of freedom and is cumbersome computationally.

The results using coupled mode shapes obtained from a free vibration analysis about the equilibrium deflection condition of the rotating beam are shown in figure 50. Up to six (M) coupled mode shapes (6 degrees of freedom) were used, and for each value of M, 15 (3N) uncoupled nonrotating mode shapes were used in the free vibration analysis. It should be noted that a minimum of 15 uncoupled nonrotating mode shapes was necessary as a basis for determining the coupled rotating modes, this minimum number having been established by the results of figure 49. As explained previously, the truncation of the number of rotating modes from 15 to M was accomplished in two different ways. For M = 5 or 6, the M lowest frequency coupled modes were retained. For M = 5 or 6, these modes consisted of 3 or 4 flap bending modes, 1 or 2 lead-lag bending modes, and 1 or 2 torsion modes, depending on the particular configuration parameters. For M = 2, 3, and 4, the modes retained were chosen

arbitrarily as follows. For M = 4, 2 flap, 1 lead-lag, and 1 torsion mode were retained; for M = 3, one of each mode was retained; and for M = 2, the lowest frequency flap and lead-lag modes were retained. Figure 50 shows clearly that the convergence using coupled rotating mode shapes is quite good; in this case as few as three coupled mode shapes provided very accurate results.

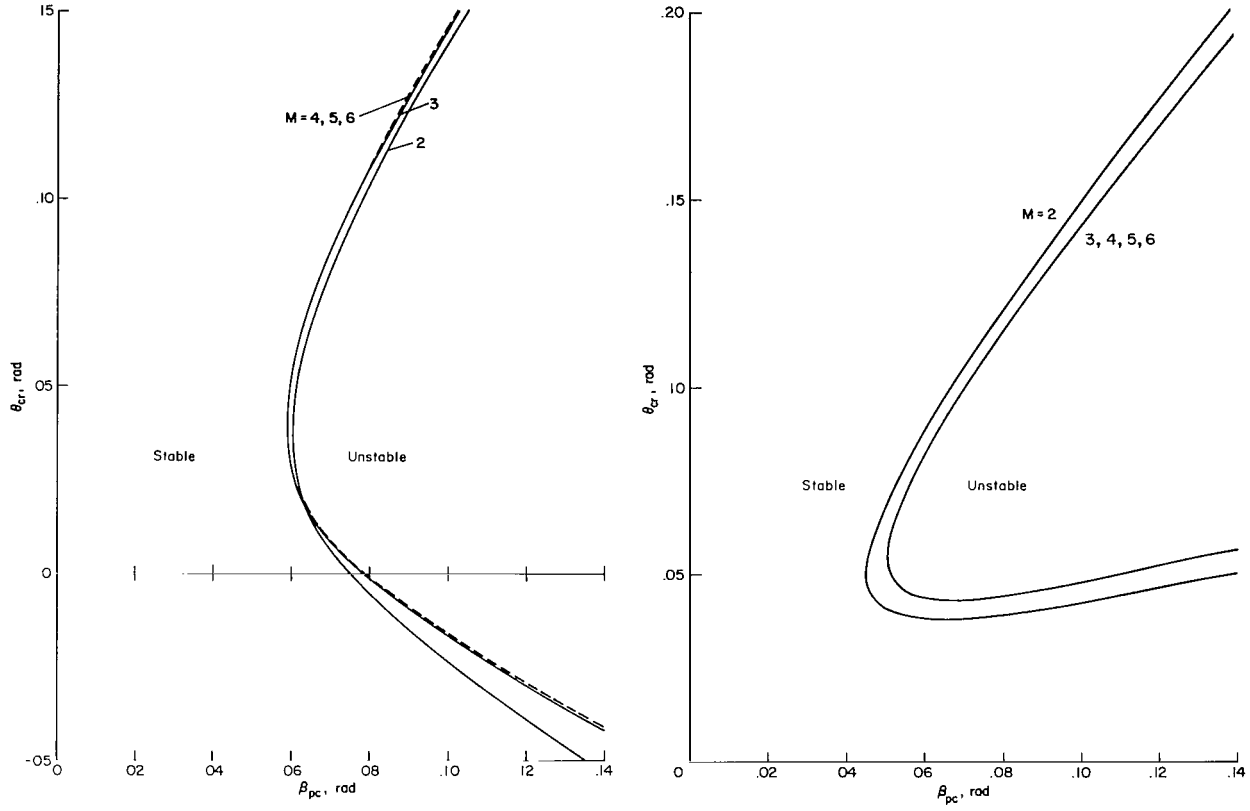

(a) Soft inplane blade: $\omega_V = 0.7$, $\omega_\phi = 2.5$, $\mathcal{R} = 0.0$.

(b) Stiff inplane blade: $\omega_V = 1.5$, $\omega_\phi = 5.0$, $\mathcal{R} = 1.0$.

Figure 50.- Convergence of stability boundaries with respect to number of mode shapes for analysis using coupled rotating mode shapes; total number of mode shapes and degrees of freedom equals M. For each value of M, the coupled rotating mode shapes are derived from 3N = 15 uncoupled nonrotating mode shapes.

The two widely different configurations used for both figure 49 and figure 50 showed similar convergence trends. This indicates that the relative effect of using uncoupled nonrotating or coupled rotating mode shapes is not highly dependent on the rotor blade configuration.

In addition to the two ways of varying the number of mode shapes presented in figures 49 and 50, it is also possible to use a truncated set of coupled rotating mode shapes and vary the number of uncoupled nonrotating mode

shapes used as a basis for the rotating modes. Results were obtained holding M constant at 6 with N varied from 2 to 5. Although not shown in the figures, the rate of convergence is virtually identical with the results using uncoupled rotating modes in figure 49. This is because, for N less than 5, the number of nonrotating mode shapes used as a basis for determining the rotating mode shapes is insufficient for accurate results.

CONCLUDING REMARKS

In this report the stability of elastic cantilever rotor blades of uniform mass and stiffness and without twist or chordwise offsets of the mass, elastic, and aerodynamic center axes was investigated for the hovering flight condition. Instabilities were found mainly for the lead-lag bending degree of freedom. These instabilities were strongly dependent on lead-lag frequency, torsion frequency, precone, and a structural coupling parameter $\mathcal{R}$ that was used to approximate the effects of nonuniformities in bending stiffness. The results of the present investigation may be summarized as follows.

1. The stability characteristics of torsionally flexible blades are mainly determined by the nonlinear structural coupling between bending and torsion deflections. This coupling produces equivalent kinematic pitch-lag and pitch-flap couplings that are generally proportional to the difference between lead-lag and flap bending stiffness $EI_{z'} - EI_{y'}$, precone, and torsional flexibility.

2. Rotor blade configurations without precone, and with typical values for torsion and bending frequencies, are generally stable for all practical blade pitch angles. Exceptions occur for stiff inplane configurations with low values of the structural coupling parameter $\mathcal{R}$ or with low torsional frequencies, or both.

3. Rotor blade configurations with precone exhibit lead-lag instability for a variety of configuration parameters in practical ranges. This instability exists at low pitch angles and is not present for stiff inplane configurations when $\mathcal{R}$ is small.

4. Increasing torsion frequency is usually stabilizing at low values of ω_ϕ, but the opposite is true at higher ω_ϕ for some configurations. In general, it is difficult to characterize the effects of torsional flexibility in a simple manner.

5. The approximate modified flap-lag equations that neglect torsional dynamic effects are usually accurate for torsion frequencies greater than 5.0. For $\omega_\phi \lesssim 5.0$, torsional dynamics should not be neglected. For torsion frequencies above 20.0, torsional flexibility is rarely important and flap-lag analyses are generally accurate.

6. The accuracy of the results is dependent on the mode shapes used in the modal solution. When using coupled rotating mode shapes, no more than six

are required. Using less accurate, uncoupled nonrotating mode shapes, a much larger number is required for the same degree of accuracy.

A logical extension of the present investigation would be to increase the scope to include two segment rotor blades with nonuniformities in mass and stiffness, twist, and a rigid body blade pitch degree of freedom. Furthermore, the effects of droop, sweep, and torque offset, as well as chordwise offsets of the elastic, mass, and aerodynamic center axes could be included.

Ames Research Center
National Aeronautics and Space Administration
and
Ames Directorate, U.S. Army Air Mobility R&D Laboratory
Moffett Field, California 94035, December 30, 1975

APPENDIX A

DERIVATION OF BLADE VELOCITY COMPONENTS U_T, U_P, AND $\dot{\varepsilon}$ FROM THE DEFORMED BLADE COORDINATE TRANSFORMATION

In equations (18) and (20) blade aerodynamic loads are expressed in terms of U_T, U_P, and $\dot{\varepsilon}$ where U_T and U_P are components of blade velocity along the y' and z' axes, and $\dot{\varepsilon}$ is the component of blade angular velocity along the x' axis. In order to use the expressions for blade aerodynamic loads in equations (10), U_T, U_P, and $\dot{\varepsilon}$ must be expressed in terms of the blade bending and torsion deflections v, w, and ϕ. The blade velocity is easily expressed in the x, y, z coordinate system. The deformed blade coordinate transformation $[T]$ relating the x, y, z and x', y', z' coordinate systems, derived in references 1 and 24, is then applied to express the U_T and U_P velocity components in terms of v, w, and ϕ. The angular velocity components of the blade may be obtained by taking advantage of certain mathematical properties of $[T]$.

The vector velocity $\vec{U}$ of the blade may be simply written in the x, y, z coordinate system from equation (45) of reference 1, and with the addition of uniform induced inflow v_i becomes

$$\vec{U} \cong (\dot{u} - \Omega v)\vec{i} + (\Omega x + \dot{v})\vec{j} + (v_i + \dot{w} + \Omega v\beta_{pc})\vec{k} = U_R\vec{i}' + U_T\vec{j}' + U_P\vec{k}'$$

The transformation $[T]$ relates the $\vec{i}$, $\vec{j}$, $\vec{k}$, and $\vec{i}'$, $\vec{j}'$, $\vec{k}'$ unit vectors of the x, y, z and x', y', z' coordinate systems, respectively. Therefore, the blade velocity components in the deformed x', y', z' coordinate system are

$$\begin{Bmatrix} U_R \\ U_T \\ U_P \end{Bmatrix} = [T] \begin{Bmatrix} \dot{u} - \Omega v \\ \Omega x + \dot{v} \\ v_i + \dot{w} + \Omega v\beta_{pc} \end{Bmatrix} \tag{A1}$$

where, valid to second order,

$$[T] = \begin{bmatrix} 1 - \frac{v'^2}{2} - \frac{w'^2}{2} & v' & w' \\ -[v'\cos(\theta + \phi) + w'\sin(\theta + \phi)] & \left(1 - \frac{v'^2}{2}\right)\cos(\theta + \hat{\phi} + v'w') & \left(1 - \frac{w'^2}{2}\right)\sin(\theta + \hat{\phi}) \\ [v'\sin(\theta + \phi) - w'\cos(\theta + \phi)] & -\left(1 - \frac{v'^2}{2}\right)\sin(\theta + \hat{\phi} + v'w') & \left(1 - \frac{w'^2}{2}\right)\cos(\theta + \hat{\phi}) \end{bmatrix}$$

and

$$\hat{\phi} = \phi - \int_0^x v''w'\,dx \tag{A2}$$

Thus, using equations (A1) and (A2)

$$U_T = -(\dot{u} - \Omega v)[v' \cos(\theta + \phi) + w' \sin(\theta + \phi) + (\Omega x + \dot{v})\cos(\theta + \hat{\phi} + v'w')\left(1 - \frac{v'^2}{2}\right)$$
$$+ (v_i + \dot{w} + \Omega v \beta_{pc})\sin(\theta + \hat{\phi})\left(1 - \frac{w'^2}{2}\right)$$

$$U_P = (\dot{u} - \Omega v)[v' \sin(\theta + \phi) - w' \cos(\theta + \phi)] - (\Omega x + \dot{v})\sin(\theta + \hat{\phi} + v'w')\left(1 - \frac{v'^2}{2}\right)$$
$$+ (v_i + \dot{w} + \Omega v \beta_{pc})\cos(\theta + \hat{\phi})\left(1 - \frac{w'^2}{2}\right)$$

For $\theta = O(\varepsilon)$ we have $\sin\theta \cong \theta$ and $\cos\theta \cong 1$. With all terms of $O(\varepsilon^2)$ neglected with respect to unity, the U_T and U_P velocity components are

$$\begin{aligned} U_T &= \Omega x + \dot{v} \\ U_P &= -\Omega x\left(\theta + \phi + \int_0^x v'w'' \, dx\right) + v_i + \dot{w} - (\theta + \phi)\dot{v} + \Omega v(\beta_{pc} + w') \end{aligned} \tag{A3}$$

The component of angular velocity along the x' axis, $\dot{\varepsilon}$, is now considered. First, an infinitesimal rotation $[\alpha]\, dt$ is defined where

$$[\alpha] = \begin{bmatrix} 0 & \alpha_k & -\alpha_j \\ -\alpha_k & 0 & \alpha_i \\ \alpha_j & -\alpha_i & 0 \end{bmatrix} \tag{A4}$$

and where α_i, α_j, and α_k are the angular velocity components about $\vec{i}'$, $\vec{j}'$, and $\vec{k}'$. Note that $\dot{\varepsilon} = \alpha_i$. By definition, the matrix $[T]$ satisfies the relation

$$\begin{Bmatrix} \vec{i}' \\ \vec{j}' \\ \vec{k}' \end{Bmatrix} = [T]\begin{Bmatrix} \vec{i} \\ \vec{j} \\ \vec{k} \end{Bmatrix}$$

Differentiating this equation yields

$$\begin{Bmatrix} d\vec{i}' \\ d\vec{j}' \\ d\vec{k}' \end{Bmatrix} = [dT]\begin{Bmatrix} \vec{i} \\ \vec{j} \\ \vec{k} \end{Bmatrix}$$

which in turn can be written in terms of $[\alpha]$ as

$$[\alpha]dt\begin{Bmatrix}\vec{i}'\\ \vec{j}'\\ \vec{k}'\end{Bmatrix} = [dT]\begin{Bmatrix}\vec{i}\\ \vec{j}\\ \vec{k}\end{Bmatrix}$$

Thus,

$$[\dot{T}] = [\alpha][T] \tag{A5}$$

The transformation $[T]$ was originally derived in reference 24 by solving the following differential equation, similar to equation (A5):

$$[T'] = [\omega][T] \tag{A6}$$

where $[\omega]$ is of the same form as $[\alpha]$ and the elements ω_i, ω_j, ω_k are rates of rotation with respect to the blade axial distance x, functions of v'', w'', and ϕ'. We now consider the derivatives of the tensor function $[T(v',w',\phi)]$:

$$\begin{aligned}[T'] &= \left[\frac{\partial T}{\partial v'}\, v'' + \frac{\partial T}{\partial w'}\, w'' + \frac{\partial T}{\partial \phi}\, \phi'\right]\\ [\dot{T}] &= \left[\frac{\partial T}{\partial v'}\, \dot{v}' + \frac{\partial T}{\partial w'}\, \dot{w}' + \frac{\partial T}{\partial \phi}\, \dot{\phi}\right]\end{aligned} \tag{A7}$$

By comparing the two equations of (A7) and equations (A5) and (A6) it is evident that, when v'', w'', and ϕ' in the expressions for ω_i, ω_j, and ω_k are replaced by $\dot{v}'$, $\dot{w}'$, and $\dot{\phi}$, the exact expressions for α_i, α_j, and α_k are obtained for a nonrotating blade. Making this replacement in the expressions for ω_i, ω_j, and ω_k in the appendix of reference 1 and adding the $\vec{i}'$, $\vec{j}'$, $\vec{k}'$ components of the blade angular velocity Ω of a rotating blade yields

$$\begin{Bmatrix}\alpha_i\\ \alpha_j\\ \alpha_k\end{Bmatrix} = \begin{Bmatrix}\dot{\phi}\\ \dot{v}'\sin(\theta+\phi) - \dot{w}'\cos(\theta+\phi)\\ \dot{v}'\cos(\theta+\phi) + \dot{w}'\sin(\theta+\phi)\end{Bmatrix} + \Omega[T]\begin{Bmatrix}\beta_{pc}\\ 0\\ 1\end{Bmatrix} \tag{A8}$$

The only component of interest here is $\alpha_i = \dot{\varepsilon}$. Thus, neglecting higher order terms

$$\dot{\varepsilon} = \dot{\phi} + \Omega(\beta_{pc} + w') \tag{A9}$$

APPENDIX B

MODAL EQUATIONS OF MOTION

In this appendix the nonlinear, variable coefficient, integro-partial differential equations (10) and (23) are written in nondimensional form and transformed into nonlinear ordinary differential equations. These modal equations are then linearized for small perturbation motions about the equilibrium operating condition. Nonlinear algebraic equations, governing the equilibrium operating condition, are written first, and the mass, damping, and stiffness matrices, equation (28), for the linearized perturbation equation are then expressed in terms of the equilibrium generalized coordinates.

First, equations (10) and equations (23) for the aerodynamic loadings are combined and written in nondimensional form:

$\delta\bar{v}$ equation:

$$-\left[\bar{v}'\int_{\bar{x}}^{1}(\bar{x}+2\dot{\bar{v}})dx\right]' + \Lambda_2\bar{v}'''' - (\Lambda_2-\Lambda_1)\sin^2(\mathcal{R}\theta)\bar{v}'''' + (\Lambda_2-\Lambda_1)\frac{\sin(2\mathcal{R}\theta)}{2}\bar{w}''''$$

$$+ (\Lambda_2-\Lambda_1)[-\sin(2\mathcal{R}\theta)(\phi\bar{v}'')'' + \cos(2\mathcal{R}\theta)(\phi\bar{w}'')''] - 2\beta_{pc}\dot{\bar{w}} - 2\int_0^{\bar{x}}(\bar{v}'\dot{\bar{v}}'+\bar{w}'\dot{\bar{w}}')d\bar{x}$$

$$+ \ddot{\bar{v}} - \bar{v} + \frac{\gamma}{6}\left\{\bar{x}\bar{v}_i\phi + \left[2\frac{c_{d_0}}{a}\bar{x} + (\theta+\phi)\bar{v}_i\right]\dot{\bar{v}} + [2\bar{v}_i - \bar{x}(\theta+\phi)]\dot{\bar{w}}\right\}$$

$$= \frac{\gamma}{6}\left(v_i^2 - \frac{c_{d_0}}{a}\bar{x}^2 - \bar{x}\bar{v}_i\theta\right) \qquad \text{(B1a)}$$

$\delta\bar{w}$ equation:

$$-\left[\bar{w}'\int_{\bar{x}}^{1}(\bar{x}+2\dot{\bar{v}})d\bar{x}\right]' + \Lambda_1\bar{w}'''' + (\Lambda_2-\Lambda_1)\sin^2(\mathcal{R}\theta)\bar{w}'''' + (\Lambda_2-\Lambda_1)\frac{\sin(2\mathcal{R}\theta)}{2}\bar{v}''''$$

$$+ (\Lambda_2-\Lambda_1)[\cos(2\mathcal{R}\theta)(\phi\bar{v}'')'' + \sin(2\mathcal{R}\theta)(\phi\bar{w}'')''] + 2\beta_{pc}\dot{\bar{v}} + \ddot{\bar{w}}\left(1+\frac{\gamma\bar{c}}{24}\right)$$

$$+ \frac{\gamma}{6}\left\{-\bar{x}^2\left(\phi + \int_0^{\bar{x}}\bar{v}'\bar{w}''\,d\bar{x}\right) + \bar{x}\bar{v}(\beta_{pc}+\bar{w}') - \frac{\bar{c}}{2}\bar{x}\bar{w}' - [2\bar{x}(\theta+\phi) - \bar{v}_i]\dot{\bar{v}}\right.$$

$$\left. + \bar{x}\dot{\bar{w}} - \frac{3\bar{c}}{4}\bar{x}\dot{\phi}\right\} = -\beta_{pc}\bar{x} + \frac{\gamma}{6}\left(-\bar{x}\bar{v}_i + \bar{x}^2\theta + \frac{\bar{c}}{2}\bar{x}\beta_{pc}\right) \qquad \text{(B1b)}$$

$\delta\phi$ equation:

$$-\frac{\mu^2 K}{2}\left[(1-\bar{x}^2)\phi'\right]' - \kappa\phi'' + (\Lambda_2 - \Lambda_1)\left[\left(\frac{\bar{w}''^2 - \bar{v}''^2}{2}\right)\sin(2\mathcal{R}\theta) + \bar{v}''\bar{w}''\cos(2\mathcal{R}\theta)\right]$$

$$+\frac{\gamma\bar{c}^2}{48}\bar{x}\dot{\phi} + \mu^2\ddot{\phi} + (\mu_2{}^2 - \mu_1{}^2)\phi\cos(2\theta) = -(\mu_2{}^2 - \mu_1{}^2)\frac{\sin(2\theta)}{2} \qquad \text{(B1c)}$$

The dimensionless parameters are given by

$$\left.\begin{aligned}
&K = \frac{k_A{}^2}{k_m{}^2} \qquad \bar{x} = \frac{x}{R} \qquad \bar{v} = \frac{v}{R}\\
&\mu_1 = \frac{k_{m_1}}{R} \qquad \Lambda_1 = \frac{EI_{y'}}{m\Omega^2R^4} \qquad \bar{w} = \frac{w}{R}\\
&\mu_2 = \frac{k_{m_2}}{R} \qquad \Lambda_2 = \frac{EI_{z'}}{m\Omega^2R^4} \qquad \bar{v}_i = \frac{v_i}{\Omega R}\\
&\mu = \frac{k_m}{R} \qquad \kappa = \frac{GJ}{m\Omega^2R^4} \qquad (\,)' = \frac{\partial}{\partial\bar{x}}(\,)\\
&\bar{c} = \frac{c}{R} \qquad \gamma = \frac{3\rho_\infty acR}{m} \qquad (\dot{}) = \frac{\partial}{\partial\psi} = \frac{\partial}{\Omega\partial t}(\,)
\end{aligned}\right\} \qquad \text{(B2)}$$

Substitution of equation (25) into equations (B1) and application of Galerkin's method yields the following set of nonlinear ordinary differential equations:

δV_i equations:

$$\sum_{j=1}^{N}\Bigg\langle V_j\{D_{ij} + [\Lambda_2 - (\Lambda_2 - \Lambda_1)\sin^2(\mathcal{R}\theta)]\beta_j{}^4\delta_{ij} - \delta_{ij}\}$$

$$+ W_j\frac{\sin(2\mathcal{R}\theta)}{2}(\Lambda_2 - \Lambda_1)\beta_j{}^4\delta_{ij} + (\Lambda_2 - \Lambda_1)\sum_{k=1}^{N}K_{jki}\Phi_j[-V_k\sin(2\mathcal{R}\theta)$$

$$+ W_k\cos(2\mathcal{R}\theta)] - 2\beta_{pc}\delta_{ij}\dot{W}_j + 2\sum_{k=1}^{N}(F_{ikj} - F_{jki})V_k\dot{V}_j - 2\sum_{k=1}^{N}F_{jki}W_k\dot{W}_j$$

$$+ \delta_{ij}\ddot{V}_j + \frac{\gamma}{6}\Bigg[\bar{v}_i I_{ij}\Phi_j + \left(2\frac{c_{d_0}}{a}E_{ij} + \theta\bar{v}_i\delta_{ij} + \bar{v}_i\sum_{k=1}^{N}\Phi_k H_{ijk}\right)\dot{V}_j$$

$$+ \left(2\bar{v}_i\delta_{ij} - \theta E_{ij} - \sum_{k=1}^{N}\Phi_k G_{ijk}\right)\dot{W}_j\Bigg]\Bigg\rangle = \frac{\gamma}{6}\left(\bar{v}_i{}^2A_i - \frac{c_{d_0}}{a}C_i - \bar{v}_i\theta B_i\right) \qquad i = 1, 2, \ldots, N \qquad \text{(B3a)}$$

δW_i equations:

$$\sum_{j=1}^{N} \Bigg\langle V_j \frac{\sin(2\mathcal{R}\theta)}{2} (\Lambda_2 - \Lambda_1)\beta_j{}^4\delta_{ij} + W_j\{D_{ij} + [\Lambda_1$$

$$+ (\Lambda_2 - \Lambda_1)\sin^2(\mathcal{R}\theta)]\beta_j{}^4\delta_{ij}\} + (\Lambda_2 - \Lambda_1) \sum_{k=1}^{N} K_{jki}\Phi_j[V_k \cos(2\mathcal{R}\theta)$$

$$+ W_k \sin(2\mathcal{R}\theta)] + 2\beta_{pc}\delta_{ij}\dot{V}_j + 2 \sum_{k=1}^{N} F_{ikj}W_k\dot{V}_j + \ddot{W}_j\left(1 + \frac{\gamma\bar{c}}{24}\right)\delta_{ij}$$

$$+ \frac{\gamma}{6}\Bigg[-J_{ij}\Phi_j + \sum_{k=1}^{N} L_{ijk}V_jW_j + \beta_{pc}E_{ij}V_j - \frac{\bar{c}}{2} O_{ij}W_j$$

$$- \left(2\theta E_{ij} + 2 \sum_{k=1}^{N} \Phi_k G_{ijk} - \bar{v}_i\delta_{ij}\right)\dot{V}_j + E_{ij}\dot{W}_j - \frac{3\bar{c}}{4} I_{ij}\dot{\Phi}_j\Bigg]\Bigg\rangle$$

$$= -\beta_{pc}B_i + \frac{\gamma}{6}\left(-\bar{v}_iB_i + \theta C_i + \frac{\bar{c}}{2}\beta_{pc}B_i\right) \qquad i = 1, 2, \ldots, N \qquad \text{(B3b)}$$

$\delta\Phi_i$ equations:

$$\sum_{j=1}^{N} \Bigg\langle \Phi_j\{\mu^2 KN_{ij} + [\kappa\gamma_j{}^2 + (\mu_2{}^2 - \mu_1{}^2)\cos(2\theta)]\delta_{ij}\}$$

$$+ (\Lambda_2 - \Lambda_1) \sum_{k=1}^{N} K_{ijk}\left[\frac{\sin(2\mathcal{R}\theta)}{2} (W_jW_k - V_jV_k) + \cos(2\mathcal{R}\theta)V_jW_k\right]$$

$$+ \mu^2\delta_{ij}\ddot{\Phi}_j + \frac{\gamma\bar{c}^2}{48} M_{ij}\dot{\Phi}_j\Bigg\rangle = -(\mu_2{}^2 - \mu_1{}^2) \frac{\sin(2\theta)}{\sqrt{2}\gamma_i} \qquad i = 1, 2, \ldots, N \qquad \text{(B3c)}$$

Here

$$
\left.
\begin{aligned}
A_i &= \int_0^1 \Psi_i \, d\bar{x} & J_{ij} &= \int_0^1 \bar{x}^2 \Psi_i \Theta_j \, d\bar{x} \\
B_i &= \int_0^1 \bar{x}\Psi_i \, d\bar{x} & K_{ijk} &= \int_0^1 \Theta_i \Psi_j'' \Psi_k'' \, d\bar{x} \\
C_i &= \int_0^1 \bar{x}^2 \Psi_i \, d\bar{x} & L_{ijk} &= \int_0^1 \bar{x}\Psi_i \Psi_j \Psi_k' \, d\bar{x} \\
D_{ij} &= \int_0^1 \left(\frac{1-\bar{x}^2}{2}\right)\Psi_i' \Psi_j' \, d\bar{x} & &\quad - \int_0^1 \bar{x}^2 \Psi_i \int_0^{\bar{x}} \Psi_j'(\bar{x}_1)\Psi_k''(\bar{x}_1) d\bar{x}_1 \, d\bar{x} \\
E_{ij} &= \int_0^1 \bar{x}\Psi_i \Psi_j \, d\bar{x} & M_{ij} &= \int_0^1 \bar{x}\Theta_i \Theta_j \, d\bar{x} \\
F_{ijk} &= -\frac{1}{\beta_k^4} \int_0^1 \Psi_i' \Psi_j' \Psi_k''' \, d\bar{x} & N_{ij} &= \int_0^1 \left(\frac{1-\bar{x}^2}{2}\right)\Theta_i' \Theta_j' \, d\bar{x} \\
G_{ijk} &= \int_0^1 \bar{x}\Psi_i \Psi_j \Theta_k \, d\bar{x} & O_{ij} &= \int_0^1 \bar{x}\Psi_i \Psi_j' \, d\bar{x} \\
H_{ijk} &= \int_0^1 \Psi_i \Psi_j \Theta_k \, d\bar{x} & \delta_{ij} &= \int_0^1 \Psi_i \Psi_j \, d\bar{x} = \int_0^1 \Theta_i \Theta_j \, d\bar{x} \\
I_{ij} &= \int_0^1 \bar{x}\Psi_i \Theta_j \, d\bar{x} & &= \begin{cases} 0 & i \neq j \\ 1 & i = j \end{cases}
\end{aligned}
\right\} \quad \text{(B4)}
$$

The equilibrium and perturbation equations are obtained by substituting equations (27) into equations (B3) and performing the operations described in the text. The resulting equilibrium equations are:

$$
\delta V_{0i} \text{ equations: } \sum_{j=1}^{N} \Bigg\langle V_{0j}\{D_{ij} + [\Lambda_2 - (\Lambda_2 - \Lambda_1)\sin^2(\mathcal{R}\theta)]\beta_j^4 \delta_{ij} - \delta_{ij}\}
$$

$$
+ W_{0j} \frac{\sin(2\mathcal{R}\theta)}{2} (\Lambda_2 - \Lambda_1)\beta_j^4 \delta_{ij} + (\Lambda_2 - \Lambda_1) \sum_{k=1}^{N} K_{jki} \Phi_{0j} [-V_{0k} \sin(2\mathcal{R}\theta)
$$

$$
+ W_{0k} \cos(2\mathcal{R}\theta)] + \frac{\gamma}{6} \bar{v}_i I_{ij} \Phi_{0j} \Bigg\rangle = \frac{\gamma}{6} \left(\bar{v}_i^2 A_i - \frac{c_{d_0}}{a} C_i - \bar{v}_i \theta B_i \right) \qquad i = 1, 2, \ldots, N \quad \text{(B5a)}
$$

δW_{0i} equations:

$$\sum_{j=1}^{N} \Bigg\langle V_{0j} \frac{\sin(2\mathcal{R}\theta)}{2} (\Lambda_2 - \Lambda_1)\beta_j{}^4\delta_{ij} + W_{0j}\{D_{ij} + [\Lambda_1$$

$$+ (\Lambda_2 - \Lambda_1)\sin^2(\mathcal{R}\theta)]\beta_j{}^4\delta_{ij}\} + (\Lambda_2 - \Lambda_1) \sum_{k=1}^{N} K_{jki}\Phi_{0j}[V_{0k} \cos(2\mathcal{R}\theta)$$

$$+ W_{0k} \sin(2\mathcal{R}\theta)] + \frac{\gamma}{6} \Bigg(\beta_{pc}E_{ij}V_{0j} - \frac{\bar{c}}{2} O_{ij}W_{0j} - J_{ij}\Phi_{0j}$$

$$+ \sum_{k=1}^{N} L_{ijk}V_{0j}W_{0k}\Bigg)\Bigg\rangle = -\beta_{pc}B_i + \frac{\gamma}{6}\left(\theta C_i - \bar{v}_i B_i + \frac{\bar{c}}{2}\beta_{pc}B_i\right) \qquad i = 1, 2, \ldots, N \quad \text{(B5b)}$$

$\delta\Phi_{0i}$ equations:

$$\sum_{j=1}^{N} \Bigg\langle \Phi_{0j}\{\mu^2 KN_{ij} + [\kappa\gamma_j{}^2 + (\mu_2{}^2 - \mu_1{}^2)\cos(2\theta)]\delta_{ij}\}$$

$$+ (\Lambda_2 - \Lambda_1) \sum_{k=1}^{N} K_{ijk}\left[\frac{\sin(2\mathcal{R}\theta)}{2} (W_{0j}W_{0k} - V_{0j}V_{0k}) + \cos(2\mathcal{R}\theta)V_{0j}V_{0k}\right]\Bigg\rangle$$

$$= -(\mu_2{}^2 - \mu_1{}^2) \frac{\sin(2\theta)}{\sqrt{2}\gamma_i} \qquad i = 1, 2, \ldots, N \quad \text{(B5c)}$$

The perturbation equations, linearized in Δ-quantities, yield a set of ordinary differential equations with constant coefficients that can be easily expressed in the form of equation (28) where

$$[M] = \left[\begin{array}{c|c|c} \delta_{ij} & 0 & 0 \\ \hline 0 & \delta_{ij}\left(1 + \frac{\gamma\bar{c}}{24}\right) & 0 \\ \hline 0 & 0 & \mu^2\delta_{ij} \end{array}\right] \qquad \text{(B6)}$$

$$[C] = 2\begin{bmatrix} \sum_{k=1}^{N}(F_{ikj} - F_{jki})V_{0k} & -\beta_{pc}\delta_{ij} - \sum_{k=1}^{N} F_{jki}W_{0k} & 0 \\ \beta_{pc}\delta_{ij} + \sum_{k=1}^{N} F_{ikj}W_{0k} & 0 & 0 \\ 0 & 0 & 0 \end{bmatrix}$$

$$+ \frac{\gamma}{6}\begin{bmatrix} 2\frac{c_{d_0}}{a}E_{ij} + \theta\bar{v}_i\delta_{ij} + \bar{v}_i\sum_{k=1}^{N} H_{ijk}\Phi_{0k} & 2\bar{v}_i\delta_{ij} - \theta E_{ij} - \sum_{k=1}^{N} G_{ijk}\Phi_{0k} & 0 \\ -2\theta E_{ij} + \bar{v}_i\delta_{ij} - 2\sum_{k=1}^{N} G_{ijk}\Phi_{0k} & E_{ij} & -\frac{3\bar{c}}{4}I_{ij} \\ 0 & 0 & \frac{\bar{c}^2}{8}M_{ij} \end{bmatrix} \qquad \text{(B7)}$$

$$
[K] = \left[\begin{array}{c|c|c}
D_{ij} + [\Lambda_2 - (\Lambda_2 - \Lambda_1)\sin^2(\mathcal{R}\theta)]\beta_j{}^4\delta_{ij} - \delta_{ij} - (\Lambda_2 - \Lambda_1) \times \sum_{k=1}^{N} K_{kji}\Phi_{0k} \sin(2\mathcal{R}\theta) & \frac{\sin(2\mathcal{R}\theta)}{2}(\Lambda_2 - \Lambda_1)\beta_j{}^4\delta_{ij} + (\Lambda_2 - \Lambda_1)\sum_{k=1}^{N} K_{kji}\Phi_{0k}\cos(2\mathcal{R}\theta) & (\Lambda_2 - \Lambda_1)\sum_{k=1}^{N} K_{jki} \times [-V_{0k}\sin(2\mathcal{R}\theta) + W_{0k}\cos(2\mathcal{R}\theta)] \\
\hline
\frac{\sin(2\mathcal{R}\theta)}{2}(\Lambda_2 - \Lambda_1)\beta_j{}^4\delta_{ij} + (\Lambda_2 - \Lambda_1)\sum_{k=1}^{N} K_{kji}\Phi_{0k}\cos(2\mathcal{R}\theta) & D_{ij} + [\Lambda_1 + (\Lambda_2 - \Lambda_1)\sin^2(\mathcal{R}\theta)]\beta_j{}^4\delta_{ij} + (\Lambda_2 - \Lambda_1)\sum_{k=1}^{N} K_{kji}\Phi_{0k}\sin(2\mathcal{R}\theta) & (\Lambda_2 - \Lambda_1)\sum_{k=1}^{N} K_{jki} \times [V_{0k}\cos(2\mathcal{R}\theta) + W_{0k}\sin(2\mathcal{R}\theta)] \\
\hline
(\Lambda_2 - \Lambda_1)\sum_{k=1}^{N} K_{ijk}[-V_{0k}\sin(2\mathcal{R}\theta) + W_{0k}\cos(2\mathcal{R}\theta)] & (\Lambda_2 - \Lambda_1)\sum_{k=1}^{N} K_{ijk} \times [V_{0k}\cos(2\mathcal{R}\theta) + W_{0k}\sin(2\mathcal{R}\theta)] & \mu^2 KN_{ij} + [\kappa\gamma_j{}^2 + (\mu_2{}^2 - \mu_1{}^2)\cos(2\theta)]\delta_{ij}
\end{array}\right]
$$

$$
+ \frac{\gamma}{6}\left[\begin{array}{c|c|c}
0 & 0 & \bar{v}_i I_{ij} \\
\hline
\beta_{pc}E_{ij} + \sum_{k=1}^{N} L_{ijk}W_{0k} & -\frac{\bar{c}}{2}O_{ij} + \sum_{k=1}^{N} L_{ikj}V_{0k} & -J_{ij} \\
\hline
0 & 0 & 0
\end{array}\right] \qquad \text{(B8)}
$$

REFERENCES

1. Hodges, D. H.; and Dowell, E. H.: Nonlinear Equations of Motion for the Elastic Bending and Torsion of Twisted Nonuniform Rotor Blades. NASA TN D-7818, 1974.

2. Houbolt, John C.; and Brooks, George W.: Differential Equations of Motion for Combined Flapwise Bending, Chordwise Bending, and Torsion of Twisted, Nonuniform Rotor Blades. NACA Rep. 1346, 1958.

3. Young, Maurice I.: A Theory of Rotor Blade Motion Stability in Powered Flight. J. American Helicopter Soc., vol. 9, no. 3, July 1964, pp. 12-25.

4. Hohenemser, Kurt H.; and Heaton, Paul W., Jr.: Aeroelastic Instability of Torsionally Rigid Helicopter Blades. J. American Helicopter Soc., vol. 12, no. 2, April 1967, pp. 1-13.

5. Ormiston, Robert A.; and Hodges, Dewey H.: Linear Flap-Lag Dynamics of Hingeless Helicopter Rotor Blades in Hover. J. American Helicopter Soc., vol. 17, no. 2, April 1972, pp. 2-14.

6. Hodges, Dewey H.; and Ormiston, Robert A.: Nonlinear Equations for Bending of Rotating Beams with Application to Linear Flap-Lag Stability of Hingeless Rotors. NASA TM X-2770, 1973.

7. Friedmann, P.; and Tong, P.: Dynamic Nonlinear Elastic Stability of Helicopter Rotor Blades in Hover and Forward Flight. (ASRL-TR-116-3, Massachusetts Inst. of Technology; NAS2-6175.) NASA CR-114485, 1972.

8. Friedmann, P.; and Tong, P.: Nonlinear Flap-Lag Dynamics of Hingeless Helicopter Blades in Hover and in Forward Flight. J. Sound Vib., vol. 30, no. 1, Sept. 8, 1973, pp. 9-31.

9. Mil', M. L.; Nekrasov, A. V.; Braverman, A. S.; Grodko, L. N.; and Leykand, M. A.: Helicopters, Calculation and Design, vol. 1, Aerodynamics. NASA TT F-494, 1967.

10. Culver, I. H.; and Rhodes, J. E.: Structural Coupling in the Blades of Rotating Wing Aircraft. IAS Paper 62-33. Institute of the Aerospace Sciences 30th Annual Meeting, New York, New York, Jan. 1962.

11. Gallot, J.: Effets Aeroelastiques sur les Qualités de Vol d'un Rotor Rigide (Aeroelastic Effects on the Flying Qualities of a Hingeless Rotor). AGARD CP No. 46, April 1969.

12. Balmford, D. E. H.: Ground and Flight Test Experience with the Westland Scout Hingeless Rotor Helicopter. AGARD CP No. 121, Advanced Rotorcraft, vol. 1, Feb. 1973.

13. Hansford, R. E.; and Simons, I. A.: Torsion-Flap-Lag Coupling on Helicopter Rotor Blades. J. American Helicopter Soc., vol. 18, no. 4, Oct. 1973, pp. 2-12.

14. Burkam, John E.; and Miao, Wen-Liu: Exploration of Aeroelastic Stability Boundaries With a Soft-In-Plane Hingeless-Rotor Model. Paper No. 610, presented at the 28th Annual National Forum of the American Helicopter Society, Washington, D. C., May 1972.

15. Huber, H. B.: Some Objectives in Applying Hingeless Rotors to Helicopters and V/STOL Aircrafts. AGARD CP 111, Sept. 1972.

16. Huber, H. G.: Effect of Torsion-Flap-Lag Coupling on Hingeless Rotor Stability. 29th Annual National Forum of the American Helicopter Society, Washington, D. C., AHS preprint 731, May 1973.

17. Arcidiacono, P. J.: Prediction of Rotor Instability at High Forward Speeds. Vol. 1. Steady Flight Differential Equations of Motion for a Flexible Helicopter Blade with Chordwise Mass Unbalance. USAAVLABS TR 68-18A, vol. 1, Feb. 1969.

18. Friedmann, Peretz: Investigation of Some Parameters Affecting the Stability of a Hingeless Helicopter Rotor Blade in Hover. (ASRL-TR-166-4, Massachusetts Inst. of Technology; NAS2-6175.) NASA CR-114525, 1972.

19. Hodges, Dewey Harper: Nonlinear Bending and Torsion of Rotating Beams with Application to Linear Stability of Hingeless Helicopter Rotors. Ph.D. Thesis, Stanford University, Dec. 1972.

20. Hodges, Dewey H.; and Ormiston, Robert A.: Stability of Elastic Bending and Torsion of Uniform Cantilevered Rotor Blades in Hover. 14th Structures, Structural Dynamics, and Materials Conference, Williamsburg, Virginia, AIAA Paper 73-405. March 1973.

21. Friedmann, Peretz: Aeroelastic Instabilities of Hingeless Helicopter Blades. J. Aircraft, vol. 10, no. 10, Oct. 1973, pp. 623-631.

22. Friedmann, P.: Some Conclusions Regarding the Aeroelastic Stability of Hingeless Helicopter Blades in Hover and in Forward Flight. J. American Helicopter Soc., vol. 18, no. 4, Oct. 1973, pp. 13-23. (Discussion by R. A. Ormiston and D. H. Hodges, vol. 20, no. 3, July 1975, pp. 46, 47.)

23. Friedmann, P.: Influence of Structural Damping, Preconing, Offsets and Large Deflections on the Flap-Lag-Torsional Stability of a Cantilevered Rotor Blade. 16th Structures, Structural Dynamics, and Materials Conference, Denver, Colorado, AIAA Paper 75-780, May 1975.

24. Peters, David A.; and Ormiston, Robert A.: The Effects of Second Order Blade Bending on the Angle of Attack of Hingeless Rotor Blades. J. American Helicopter Soc., vol. 18, no. 4, Oct. 1973, pp. 45-48.

25. Greenberg, J. Mayo: Airfoil in Sinusoidal Motion in a Pulsating Stream. NACA TN 1326, 1947.

26. Bisplinghoff, Raymond L.; Ashley, Holt; and Halfman, Robert L.: Aeroelasticity. Addison-Wesley, Reading, Massachusetts, 1955.

27. Gessow, Alfred; and Myers, Garry C., Jr.: Aerodynamics of the Helicopter. Fredrick Ungar Publishing Company, New York, New York, 1967.

28. Chang, Tish-Chun; and Craig, R. R., Jr.: On Normal Modes of Uniform Beams. EMRL 1068, Univ. of Texas (Austin), 1969.

29. Felgar, R. P., Jr.: Formulas for Integrals Containing Characteristic Functions of a Vibrating Beam. Circular 14, Bur. Eng. Res., Univ. of Texas (Austin), 1950.

30. Meirovitch, Leonard: Elements of Vibration Analysis. McGraw-Hill, New York, New York, 1975.

31. Peters, D. A.: An Approximate Solution for the Free Vibrations of Rotating Uniform Cantilever Beams. NASA TM X-62,299, 1973.

"The aeronautical and space activities of the United States shall be conducted so as to contribute . . . to the expansion of human knowledge of phenomena in the atmosphere and space. The Administration shall provide for the widest practicable and appropriate dissemination of information concerning its activities and the results thereof."

—NATIONAL AERONAUTICS AND SPACE ACT OF 1958

NASA SCIENTIFIC AND TECHNICAL PUBLICATIONS

TECHNICAL REPORTS: Scientific and technical information considered important, complete, and a lasting contribution to existing knowledge.

TECHNICAL NOTES: Information less broad in scope but nevertheless of importance as a contribution to existing knowledge.

TECHNICAL MEMORANDUMS: Information receiving limited distribution because of preliminary data, security classification, or other reasons. Also includes conference proceedings with either limited or unlimited distribution.

CONTRACTOR REPORTS: Scientific and technical information generated under a NASA contract or grant and considered an important contribution to existing knowledge.

TECHNICAL TRANSLATIONS: Information published in a foreign language considered to merit NASA distribution in English.

SPECIAL PUBLICATIONS: Information derived from or of value to NASA activities. Publications include final reports of major projects, monographs, data compilations, handbooks, sourcebooks, and special bibliographies.

TECHNOLOGY UTILIZATION PUBLICATIONS: Information on technology used by NASA that may be of particular interest in commercial and other non-aerospace applications. Publications include Tech Briefs, Technology Utilization Reports and Technology Surveys.

Details on the availability of these publications may be obtained from:

SCIENTIFIC AND TECHNICAL INFORMATION OFFICE

NATIONAL AERONAUTICS AND SPACE ADMINISTRATION

Washington, D.C. 20546